POLITECNICO DI MILANO

Department of Industrial and Information Engineering

Measurements Based on Fraunhofer Diffraction Theory and Self-mixing Interferometry

Supervisor: Prof. Michele Norgia

Master Thesis by: Zhang Jiawen
Student ID Number: 10575584

Abstract

Along with the advances in technology and expansion of industrial applications, laser measurement technology has been widely used in various fields due to its characteristics such as non-contact, high-resolution and fast measurement speed. In this paper, two kinds of laser measurement methods are mainly studied. One is the particle sizing technique based on Fraunhofer diffraction theory. Fraunhofer diffraction-based instruments can accurately measure the size distribution of particles ranging from 2 μm to 1000 μm. The other one is dimensional measurement based on self-mixing interferometry. Self-mixing interferometry has been considered even more as a valid alternative to the classical optical instrumentations for its compact, low-cost and user-friendly setup.

For the first part of this thesis work, the reconstruction method and experiments of narrow particle size distribution measurement were carried out based on the Fraunhofer diffraction. The main results are listed as follows:

1. The main methods of particle size measurement and the state-of-the-art of diffraction particle sizing were outlined. Traditional system and the traditional particle sizing algorithms for the Fraunhofer diffraction-based instruments were studied. Shortcomings of the traditional methods and systems in case of narrow particle size distributions were analyzed.

2. In order to improve the reconstruction accuracy, an iterative algorithm was introduced to reduce the deviation and the result of the dual integral inversion method was used as feedback. The PID controller was implemented in the control loop to generate the reconstructed distributions of the particles. The neural network PID and fuzzy PID were utilized to reduce the sensitivity to the initial values of the PID parameters, and the performance was verified by using numerical simulations.

3. In order to pick up the weak signals at large angles in the particle size measurement system, a modulated light was generated and the intensity values on the detectors were demodulated, followed by data acquisitions at high signal to noise ratios. Experiments were implemented on the standard particle suspension to evaluate the performance of the proposed particle sizing system. Experimental results showed that the proposed algorithm performs better than the dual integral algorithm, in cases of different background noises.

For the second part of this thesis work, the self-mixing interferometry theory is used to measure the displacement and the speed of the target. The main contents are as follows:

1. By using the general theoretical model of self-mixing interferometry, the influence of model parameters on self-mixing interference signals is researched by numerical simulation.

2. A displacement measurement based on fringes counting is studied, and the basic measurement system based on self-mixing interferometry is set up. Both the simulated and the experimental results show the feasibility of this method.

3. A method oriented to the measure of the speed of a target is studied. The method based on a particular frequency-domain algorithm and has strong robustness. The feasibility and effectiveness of the method are verified by simulation and experiments.

Keywords: Fraunhofer diffraction, Particle size distribution, Self-mixing interference, Displacement measurement, Speed measurement

Abstract

Oltre ai progressi tecnologici e all'espansione delle applicazioni industriali, la tecnologia di misurazione laser è stata ampiamente utilizzata in vari campi grazie alle sue caratteristiche come la velocità di misurazione e l'alta risoluzione, nonché la possibilità di misure senza. In questo articolo vengono principalmente studiati due tipi di metodi di misurazione laser. Il primo è la tecnica di dimensionamento delle particelle basata sulla teoria della diffrazione di Fraunhofer. Gli strumenti basati sulla diffrazione di Fraunhofer possono misurare accuratamente la distribuzione dimensionale di particelle che vanno da 2 μm a 1000 μm. Il secondo riguarda la misurazione dimensionale basata sull'interferometria a retroiniezione. L'interferometria a retroiniezione è una valida alternativa alle classiche strumentazioni ottiche per la sua configurazione compatta, a basso costo e user-friendly.

Per la prima parte di questo lavoro di tesi, il metodo di ricostruzione e gli esperimenti di misurazione della distribuzione delle dimensioni delle particelle strette sono stati effettuati sulla base della diffrazione di Fraunhofer. I risultati principali sono elencati come segue:

1. Sono stati delineati i principali metodi di misurazione delle dimensioni delle particelle e lo stato dell'arte del dimensionamento delle particelle di diffrazione. Sono stati studiati il sistema tradizionale e i tradizionali algoritmi di dimensionamento delle particelle per gli strumenti basati sulla diffrazione di Fraunhofer. Sono state analizzate le carenze dei metodi e dei sistemi tradizionali in caso di distribuzioni di dimensioni strette delle particelle.

2. Al fine di migliorare l'accuratezza della ricostruzione, è stato introdotto un algoritmo iterativo per ridurre la deviazione e il risultato del duplice metodo di inversione integrale è stato utilizzato come feedback. Il controller PID è stato implementato nell'anello di controllo per generare le distribuzioni ricostruite delle particelle. Il PID di rete neurale e il PID fuzzy sono stati utilizzati per ridurre la sensibilità ai valori iniziali dei parametri PID e le prestazioni sono state verificate utilizzando simulazioni numeriche.

3. Al fine di raccogliere i segnali deboli a grandi angoli nel sistema di misurazione delle dimensioni delle particelle, è stata generata una luce modulata e i valori di intensità sui rivelatori sono stati demodulati, seguiti da acquisizioni di dati ad elevati rapporti segnale / rumore. Per valutare le prestazioni del sistema di dimensionamento delle particelle proposto sono stati condotti diversi esperimenti con sospensione di particelle standard. I risultati sperimentali hanno mostrato che l'algoritmo proposto ha prestazioni migliori rispetto all'algoritmo a doppio integrale, in caso di rumori di fondo diversi.

Per la seconda parte di questo lavoro di tesi, la teoria dell'interferometria a retroiniezione viene utilizzata per misurare lo spostamento e la velocità di un bersaglio remoto. I contenuti principali sono i seguenti:

1. Utilizzando il modello teorico generale dell'interferometria a retroiniezione, l'influenza dei parametri del modello sui segnali di interferenza è stata studiata mediante simulazione numerica.

2. È stato implementato un sistema di misura di spostamento basato sul conteggio delle frange e si è impostato un sistema basato sull'interferometria a retroiniezione che può essere applicato a diverse tipologie di misura. Sia i risultati simulati che quelli sperimentali confermano la funzionalità di questo approccio.

3. È stato studiato ed implementato un metodo di misura di velocità di un bersaglio, basato su un particolare algoritmo nel dominio della frequenza, che dimostra una notevole robustezza alle variazioni di ampiezza del segnale. La fattibilità e l'efficacia del metodo sono state verificate mediante simulazione ed esperimenti.

Parole chiave: diffrazione di Fraunhofer, distribuzione delle dimensioni delle particelle, interferometria a retroiniezione, misurazione di spostamento, misurazione di velocità.

Contents

Summary

The purpose of this research project is to investigate the feasibility of contactless measurements using Fraunhofer diffraction and self-mixing interferometry respectively.

The total thesis work can be dependent into two parts. The first one is about the particle sizing based on Fraunhofer diffraction which is described in Chapter 1 to Chapter 4. And the second part is about the movement measurement based on Self-mixing interferometry which is described in Chapter 5 to Chapter 7.

In Chapter 1, the research significance of particle size measurement and several main particle size measurement methods are introduced briefly. The research status of particle size measurement technology based on Fraunhofer diffraction theory are brought out.

In Chapter 2, the basic principle of particle sizing measurement by Fraunhofer diffraction method is studied. While, the traditional diffraction method particle size measuring device is introduced, and the principle of traditional integral transform inversion algorithm is briefly described. At last, several problems which should be solved are posed.

In Chapter 3, the closed-loop iterative theory is introduced into the reconstruction algorithm to reduce the reconstruction error for the narrow-distribution particle sizing measurement. In order to realize the adaptive selection of controller parameters and improve the applicability, the principles of neural network model and fuzzy control theory are studied. The model is combined with the traditional double integral inversion formula to propose a suitable distribution for narrowly distributed particles. The proposed algorithm is verified by numerical simulation.

In Chapter 4, a setup for particle sizing measurement based on the principle of modulation and demodulation is designed. Through comparison experiments, it is verified that the improved signal measurement method has good anti-noise ability. Meanwhile, a data calibration method is proposed to improve the accuracy of measurement signals. Finally, the measured experiments were carried out with different standard particle suspensions, and the accuracy and reliability of the proposed improved algorithm are verified.

In Chapter 5, the principle and characteristics of laser self-mixing interference are introduced, and the theoretical model of self-mixing interference system is established. Meanwhile, the influence of the feedback level C and amplitude of the movement of the target a is analyzed by simulation.

In Chapter 6, the displacement measuring method based on the fringe counting is introduced, and the algorithm is verified by simulation. The measurement system is designed and built and the experimental results prove the feasibility of the method.

In Chapter 7, a novel reconstruction technique based on spectral analysis is studied. The shown algorithm, which operates on frequencies domain, gives more robust reconstructions of the remote displacements.

Finally, the general conclusion is summarized and some further work is offered.

Chapter 1 Introduction of particle sizing

1.1. Background of particle size measurement

Particles refer to tiny solids (dust), liquids (droplets) or gases (bubbles) in a segmented state. With the development of social economy and the maturity of industrialization problems related to particle measurement are faced in several fields. The concept of particle size is usually used to compare the size of various types of particles. In general, the particle size is defined as the size of the space occupied by the particles. The value of it varies widely, from sub-nanometer to millimeter [1].

Particle size has important significance in many fields such as industry, chemistry, medical treatment, etc. It is not only an important evaluation index of product quality and performance, but also affects the efficient use of energy and optimization of process. For example, in the combustion of pulverized coal and liquid fuel, the size of pulverized coal particles and the degree of atomization of liquid fuel directly affect the efficiency and stability of the combustion reaction [2]. In the field of chemistry, the particle size of the metal particles used for catalysis directly affects the activity of the catalyst [3]. In the industrial field, the particle size of the coating affects the durability and smoothness of the product; in the medical field, the particle size of the prepared drug directly affects the efficacy[4].

In addition, the impact of particulate matter on the environment and human health cannot be ignored. As the population grows, the emissions of particulate matter generated in daily production and life become more and more serious, such as coal-fired soot generated during heating and automobile exhaust emitted during travel. As the size of the particles is smaller, it is easier to suspend in the air and it is difficult to settle. When the particle size is less than 10 μm, it can be inhaled, which has adverse effects on the upper respiratory tract and even the lungs of the human body[5]. Excessive inhalation of dust will cause great harm to the human body. In the coal mining industry, due to the possibility of suspended solid particles in the working environment, long-term inhalation of productive dust will cause pneumoconiosis and directly endanger the health of workers. The haze weather caused by particulate matter (PM 2.5) exceeding atmospheric circulation capacity also has a negative impact on the ecological environment and human health. Therefore, with the concept of sustainable development and the improvement of residents' health awareness, the analysis and control of particulate emissions has become an issue of increasing public concern.

In summary, the particle size measurement technology is closely related to industrial development, environmental protection and the health of residents. The research on particle size measurement shows its importance and urgency recently. How to achieve faster and more accurate measurement of particle size is increasingly concerned.

1.2. The main measurement methods of particle sizing

The particle size measurement technology first started in Germany during the World War II[6]. With the advancement of technology and the development of process manufacturing technology, traditional measurement methods have been continuously improved, and emerging measurement technologies have been continuously proposed. Up to now, many measurement methods have been formed with different principles and different application ranges.

1）Sieving method

Sieving is the most common particle size measurement technique [7, 8]. The principle can be described as follows: the sample to be tested is placed on a standard sieve with a known mesh pore size. When the sieve is vibrated, due to gravity, particles having a diameter smaller than the pore size of the sieve pass through the sieve hole, and particles having a diameter larger than the pore size of the sieve remain in the standard sieve. Therefore, the particles of different particle sizes can be separated. In the actual operation process, the particle size and distribution range of the sample to be tested are estimated, and a set of standard sieves with different apertures are selected. The apertures are arranged vertically from top to bottom according to the pore size. The largest is placed on the uppermost layer with a screen cover to prevent particles from splashing. The smallest is placed in the lowest layer with the container below to collect the smallest particles. After the sieving, the ratio of the mass of the residual particles on the different standard sieves to the total mass is measured, and the particle size distribution of the measured sample by mass can be obtained after statistical analysis.

The advantage of the sieving method is its simple principle and low-cost. For the particle size distribution of large particles (diameter 150 μm or more), the sieving method can obtain the accurate results and has unparalleled superiority. However, its shortcomings are also obvious: Small particle sieving is difficult to achieve due to the strong adhesion and agglomeration between particles; It is difficult to prepare the fine standard sieves; Excessive sieving may cause the particles size changing when pass through the pore; Long-term use will cause a series of problems such as mesh deformation and clogging, which will affect the measurement accuracy. The above disadvantages of the sieving method limit its application in the field of small particle size measurement, so it is usually applied in the field of large particle measurement requiring low precision.

2）Sedimentation techniques

The physical meaning of sedimentation techniques is clear. It is based on the Stokes equation. When the particles in the suspension system are uniformly settled (or centrifugally settled), the gravity of the particles themselves (or the centrifugal force), the buoyancy of the particles and the viscous drag reach the equilibrium. The particle size distribution can represent a function related to the sedimentation velocity, so the particle size distribution can be obtained by measuring the sedimentation velocity[9]. In actual measurement, the sedimentation velocity is difficult to obtain, so the particle size distribution of the particles to be tested is usually determined by measuring other related quantities such as pressure, density, concentration. The sedimentation method can be divided into the gravity sedimentation method and the centrifugal sedimentation method.

The Stokes equation for gravity settlement is [10]

$$\mathrm{V}_g = \frac{d^2(\rho_s - \rho_l)}{18\eta} g \tag{1.1}$$

where V_g represents the sedimentation velocity of the particles; *d* is the particle diameter; ρ_s and ρ_l represent the density of the solid particles and of the liquid dispersion medium respectively; η is the viscosity of the liquid; *g* is the acceleration of gravity. It can be seen from Eq.(1.1) that in the gravity sedimentation method, the sedimentation velocity is proportional to the square of the particle size.

The centrifugal sedimentation method firstly rotates the suspended liquid of the measured particles around a certain axis at a high speed. During the movement of the particles, the speed and acceleration are continuously increased. The Stokes equation for centrifugal sedimentation is

$$\frac{\mathrm{dX}}{\mathrm{dt}} = \frac{d^2(\rho_s - \rho_l)}{18\eta} \mathrm{X}\omega^2 \tag{1.2}$$

where *X* represents the horizontal distance of the particles from the axis of rotation; ω is the angular velocity of the centrifugal motion. Compared with the gravity sedimentation method, the centrifugal sedimentation method can expand the range of analysis particles, and the measurement limit is significantly reduced.

The sedimentation method can measure the particle size distribution of small particles with high resolution and low cost. However, the sedimentation method takes more time and has poor reproducibility. When using the sedimentation method, the particles must be completely infiltrated by the liquid. Therefore, the dissolution of the particles will bring a certain error to the measurement. In addition, factors such as mutual motion between particles, Brownian motion, and non-ideal sphere shape of the particles all affect the measurement accuracy of the sedimentation method.

3）Optical counting methods

Particle size distribution can be measured microscopically by sizing against a graticule and counting, but for a statistically valid analysis, millions of particles must be measured. This is impossibly arduous when done manually, but automated analysis of electron micrographs is now commercially available. It is used to determine the particle size within the range of 0.2 to 100 micrometers[11].

Microscopy is simple to operate. Even if the particles agglomerate, the particles can be visually distinguished by observation. Therefore, the measurement accuracy is high, and the measurement results are often used as calibration standards for other particle size measurement methods. However, it can only observe the two-dimensional projection size of the particles, and the cost is high. Usually the sample preparation process is complicated and cumbersome, and the measurement speed is relatively slow. The early microscopic method for measuring particle size is mainly for manual observation and counting. It is easy to introduce human error such as missed detection or repeated counting. In recent years, with the development of image processing technology and the popularity of computers, dynamic image processing technology has been used to improve microscopy[12, 13]. This technology effectively avoids the operational errors introduced by manual analysis, and greatly shortens the measurement time and improves the measurement accuracy.

4）Electro-resistance counting methods

An example of this is the Coulter counter, which measures the momentary changes in the conductivity of a liquid passing through an orifice that take place when individual non-conducting particles pass through. The particle count is obtained by counting pulses. This pulse is proportional to the volume of the sensed particle[14].

The electro-resistance counting method has the advantages of simple operation, high measurement speed, high precision, and good repeatability. It is suitable for measuring a particle group with a narrow particle distribution. In practical applications, the choice of small hole size is particularly important. If the small hole is too narrow, the hole will be blocked, and the small hole will cause the particles to overlap, that is, two and more particles pass through the small hole at the same time, which introduces measurement error. For a wide distribution of particle groups, it is very difficult to determine the optimal pore size, so it is difficult to ensure the measurement accuracy.

5）Ultrasound attenuation spectroscopy

Low-energy ultrasonic waves are widely used in the field of detection, such as non-destructive testing, ultrasonic imaging, and ultrasonic speed measurement[15]. The processing of the method based on ultrasound attenuation spectroscopy is that when the ultrasonic wave passes through the medium containing the particles to be measured, the ultrasonic wave will produce phase change and attenuation due to the absorption and scattering of the particles, and the speed or attenuation coefficient of the ultrasonic wave can be obtained and then the particle size distribution can be reconstruct[16, 17].

Ultrasonic method has the advantages of no dilution, non-destructive testing, and simple hardware. Compared with visible light, sound waves have stronger penetrating ability, and their detectors can better adapt to harsh field conditions such as probe pollution. There are significant advantages in high concentration and online measurement. However, ultrasonic measurement relies on the accuracy of theoretical models, and the modeling complexity of particle scattering theory makes it limited in application.

6）Laser scattering method

Laser scattering is one of the most widely used methods of particle size measurement. The scattering method is based on Mie scattering. When the collimated laser beam is irradiated onto the measured particle group, the light wave will undergo various effects such as reflection, refraction, diffraction and absorption under the action of the particles. Because of these effects, the light is deflected away from the original direction of propagation and spread out in all directions. This phenomenon is called light scattering. Since the scattering effect mainly depends on the particle size and material of the particles, the particle size information of the measured particle group can be obtained by measuring the scattered light parameters[18].

According to the difference of the measured scatter signal, several methods based on laser scattering are proposed:

a) Angular scattering

The angular scattering method obtains the particle size distribution information of the measured particle system by measuring the distribution of scattered light intensity or scattered light energy at a certain angle or angles.

b) Extinction spectroscopy

The extinction spectroscopy obtains the particle size distribution information by measuring the degree of attenuation of light of different wavelength. The measuring source of the extinction spectroscopy is a complex color light containing multiple wavelengths[19].

c) Dynamic light scattering

The dynamic light scattering method irradiates the coherent beam onto the measured particle system, and the formed scattered light spot will change with time. By measuring the pulsation of the scattered light with time at a certain angle, the particle size distribution information can be obtained.

d) Polarization method

The scattered light output after passing through the particle group is polarized light, and the polarization method calculates the particle size distribution function by measuring the degree of polarization of the scattered light at different angles.

The light scattering method has the advantages of high measurement accuracy, good repeatability, fast measurement speed, and so on. It has broad application prospects, and is suitable for automated online measurement. However, the lack of light wave penetration is an inherent limitation of the light scattering method, and its measurement results are largely affected by the distribution model.

1.3. Research status about the particle sizing

The development of particle measurement technology has a positive effect on industrial development, medical progress and environmental protection. With the continuous research of related topics, a variety of advanced measurement methods and theories are constantly being proposed. In the 1880s, the introduction of Rayleigh scattering marked the beginning of the study of scattering theory. Subsequently, G.Mie derived the analytical solution of Maxwell's equations on the scattering boundary of spherical particles, and obtained the detailed expression of the physical quantity of each light scattering field[20], which is the famous Mie theory. In 1957, Van de Hulst gave a research framework for measuring geometrical optics in the forward large angle range based on the scattering method. Then the principle of light scattering was officially used in the field of measurement. However, the classical Mie scattering theory is complicated and cumbersome, and the rigorous solution is subject to many limitations. It is difficult to solve complex problems, so the scope of application of this theory is limited. In 1976, J. Swithenbank et al. proposed the Fraunhofer diffraction theory as an approximate calculation of the Mie scattering theory. The particle size measurement method based on Fraunhofer diffraction is also called the small angle forward diffraction method. The main principle is to obtain the particle size distribution information by analyzing the diffraction intensity. The method has the advantages of simple measuring device, small sample size, wide measuring range, good repeatability and fast measuring speed, and is suitable for particle size measurement with particle diameter in the range of 0.1 to 3000 μm. The theory requires less physical quantity and is relatively simple to calculate. Therefore, this method gradually replaces the traditional method and becomes the main method for measuring the particle size distribution of industrial particles.

Since diffraction theory is used to describe the scattering behavior of particles is an approximation method, there are theoretical errors in the measurement of small particles, and the particle size inversion problem is seriously ill-conditioned. In order to meet the accuracy, speed and reliability of online measurement in the field of particle measurement. In recent years, related research has mainly focused on two aspects: one is the improvement of the structure of the measuring device, and the other is the research of the granular inversion algorithm.

There are several factors that affect the accuracy of the particle size measurement system: the choice of the focal length of the receiving lens, the accuracy of the alignment of the photodetector, the concentration of the sample to be measured, the refractive index, etc. To achieve accurate measurement, the questions such as how to choose the focal length of the appropriate lens have been widely studied and discussed[21]. Conventional diffraction measuring devices are limited by the numerical aperture and detector size of the Fourier lens. The particle size measurement range is narrow and the Gaussian distribution of the laser may introduce a certain error. In 1989, Hu Zhuguo used anti-Gaussian filters to eliminate the effects of lasers as Gaussian beams [22]. At the same time, the particle size of the diffraction method cannot measure particles with too small particle diameter, and there is a lower limit of measurement. How to effectively extend the lower limit of measurement of the diffraction measurement system is also the main direction of the improved system. The improvement measures that have been proposed are the use of an inverted Fourier transform optical system. Dual lens technology, dual light source technology, polarization scattering intensity (PIDS) technology and omnidirectional multi-angle technology and so on[23, 24]. In order to expand the measurement range, Germany Sympatec used a Fourier lens group with different focal lengths instead of a single lens. In the measurement, the detector size is constant, and the range of the detection scattering angle is changed by changing the focal length of the lens, thereby expanding the measurement range. A measurement system based on the inverse Fourier transform structure is proposed. This technique places the Fourier lens in front of the sample, thereby reducing the equivalent focal length of the system without changing the focal length of the lens[25]. In 2009, Dandong Baxter added a large-angle detector based on the traditional structure to realize a single-beam multi-lens structure, which can detect the increase of the diffraction angle range and effectively extend the lower limit of measurement. Subsequently, Malvern proposed to increase the oblique incident light source. The method solves the problem that part of the large-angle scattered light cannot be received by the detector due to total reflection.

In addition to obtaining as much diffraction distribution information as possible, how to reconstruct the particle size distribution at high speed and accurately is also a major concern. The problem of solving the particle size distribution is essentially solving the problem of the first type of Fredholm equation. According to whether it is necessary to presuppose the approximate distribution function of the measured particle group before the solution, the particle size inversion algorithm can be divided into the non-independent mode algorithm and the independent mode algorithm[26]. According to the application principle of solving, the particle size inversion algorithm can be divided into matrix equation method and integral transform method. One of the most common methods for solving inverse scattering problems in matrix method. Commonly used matrix inversion algorithms include Phillips-Twomey algorithm, Chahine algorithm, Projection algorithm and projection algorithm. Phillips-Twomey algorithm adds a light to the intensity distribution matrix. The deterministic approach reduces the ill-posed conditions of the matrix, but the introduction of the smoothing factor reduces the accuracy of the inversion algorithm[27, 28]. Chahine algorithm does not rely on pre-assumed distribution but is sensitive to measurement noise [29]. The Projection algorithm can reconstruct multi-peak distribution well, but the inversion results are oscillating and smearing[30]. The projection algorithm converges to a certain solution of the equation through the loop, but repeated iterations easily lead to oscillation[31]. In the past years, advanced theories such as neural network algorithms and genetic algorithms have been applied to the particle size distribution inversion process of particles. The combination of multi-layer neural network structure and non-negative least squares method can obtain the inversion result closer to the true value. This method can be used to invert the particle size distribution of non-spherical particles[32, 33]. The main principle of the integral transformation method is to obtain the analytical solution of particle size distribution by means of integral transformation. The Chin-Shifrin algorithm proposed in the 1950s is the most widely used integral inversion algorithm[34, 35]. The advantages are that the numerical calculation is simple and the inversion result is independent of the selection of the inversion interval, but the algorithm is sensitive to noise and the inversion result diverges when the particle size is small. In 2009, a double integral granularity inversion method was proposed [36]. The method uses the Schlomilch equation and the Hankel transform to solve the particle size distribution information. Compared with the Chin-Shifrin algorithm, it is not sensitive to noise, and the reconstruction accuracy for the small particle size distribution is better than the Chin-Shifrin algorithm. The research on the integral transformation method has been focused on the improvement of the traditional Chin-Shifrin algorithm, such as correcting the integral transformation formula, introducing a rectangular window function[37-39]. At the same time, the Chin-Shifrin algorithm theoretically requires the range of the integral scattering angle to be $(0,+\infty)$, and the range of the scattering angle in the actual measurement is bound to be limited. Therefore, how to select the appropriate integral range is also the focus of research in recent years [40].

Chapter2 Basic principle and inversion algorithm

With the continuous development of industrial technology, the requirements for particle size measurement in various application fields are gradually improved. The traditional particle size measurement methods have certain deficiencies in measurement speed and accuracy, and thus cannot adapt to the current online measurement and high precision requirements. In recent years, with the development of photodetection technology, optical measurement methods have received extensive attention. Among them, the particle size measurement technology based on Fraunhofer diffraction theory has the advantages of simple numerical calculation, convenient operation, fast measurement speed and wide application range, and is widely used in the preparation of laser particle size analyzer. At the same time, since the inversion algorithm for particle size distribution is essentially the solution of the first type of Fredholm integral equation, it is important to use a suitable inversion algorithm to improve the reconstruction accuracy.

2.1. Optical principle based on diffraction

The Fraunhofer diffraction method is essentially using an approximation of the scattering phenomenon when the particle size is equivalent to the wavelength. The light scattering refers to a phenomenon in which the direction of propagation changes when the beam passes through an inhomogeneous medium, and no longer propagates along a straight line but deflects in all directions of the space[41]. Generally, when the particle size is measured by the diffraction method, the measured particles should be added to distilled water to be configured as a suspension. According to whether the scattering phenomena between different particles interact with each other, the scattering phenomenon can be divided into uncorrelated scattering and related scattering. When the concentration of the measured particles is low, the spacing between the individual particles is large, and the scattering between the individual particles does not affect each other. This scattering is called uncorrelated scattering, and vice versa, when the distance between the individual particles is greater than 3 times the diameter of the particle, the resulting scattering phenomenon can be considered as uncorrelated scattering[42]. Correlated scattering needs to consider the interference effect of light, multiple scattering of particles and so on. So the solution conditions are complex. In practical applications, most of the measured particle groups are low-concentration samples, which can usually be processed according to uncorrelated scattering. According to the output scattered light generated by scattering of a single particle or by multiple scattering, the scattering phenomenon can be divided into single scattering and complex scattering. The single scattering means that the output scattered light is only scattered by a particle. Conversely, if the scattered light encounters the particle during the propagation and scatters again, it is called complex scattering[43]. In this paper, the study is carried out under the uncorrelated single scattering condition.

2.1.1. Principle of diffraction method

When a beam of parallel light is irradiated onto the particle, it will deviate from the original propagation direction to the surrounding space. The accurate expression of the scattered light intensity can be solved by Mie scattering theory. The expression is complex in form, and the scattered light intensity at a certain point in space can be related to the scattering angle, the size of the particles, and the refractive index. When the particle size is large (more than 2 μm), the diffraction phenomenon is dominant. The relatively simple Fraunhofer diffraction theory can be used to approximate the Mie scattering theory. At this time, the influence of the refractive index of the measured particles can be ignored. The intensity of the diffracted light is only related to the diffraction angle and the particle size. By measuring the intensity of the diffracted light at the corresponding diffraction angle, the size information of the particle can be obtained.

In physics, Babinet's principle states that the diffraction pattern from an opaque body is identical to that from a hole of the same size and shape except for the overall forward beam intensity. Assuming that the incident light is monochromatic parallel light and the sample region has only one particle of diameter D. The diffraction intensity distribution on the annular photodetector located at the focal plane of the converging lens can be obtained from the diffraction intensity distribution of the circular aperture of the same diameter. That is, in addition to the focus of the lens, the diffraction intensity distribution of the particles and the diffraction intensity distribution produced by the light passing through the circular hole of the same diameter are completely identical, and the intensity distribution can be expressed as[44]

$$I(\theta) = I_0 \frac{\pi^2 D^4}{16 f^2 \lambda^2} \left(\frac{2J_1(x)}{x} \right)^2 \tag{2.1}$$

where I_0 is the incident light intensity, λ is the incident light wavelength, f is the focal length of the convex lens, $x = \alpha \cdot \sin\theta = \frac{\pi D \sin\theta}{\lambda}$, α is the optical size parameter, θ is the diffraction angle, J_1 is the Bessel function of the first kind and order one. When θ=0（ie, x=0）, according to the nature of the Bessel function, $2J_1(x)/x$=1 can be obtained. Therefore, the diffraction intensity of the center position of the ring photodetector can be obtained as

$$I(0) = I_0 \frac{\pi^2 D^4}{16 f^2 \lambda^2} \tag{2.2}$$

It is shown in Eq. (2.2) that the intensity of the central diffracted light is proportional to the fourth power of the particle diameter. The larger the particle size of the measured particle, the more concentrated the light energy is concentrated at the center after diffraction. Substituting the Eq.(2.2) into Eq.(2.1), it can be obtained the diffraction intensity distribution with respect to the central intensity at any angle θ:

$$P(\theta)=\frac{I(\theta)}{I(0)}=\left[\frac{2J_1(x)}{x}\right]^2 \tag{2.3}$$

From Eq.(2.3) we know that the diffraction pattern is a concentric ring, and the central bright spot is called Airy disk. The degree of dispersion of the angular distribution can be measured by the half angle of the Airy disk θ_0, which can be expressed as

$$\theta_0=\arcsin\left(\frac{1.22\lambda}{D}\right)\approx 1.22\frac{\lambda}{D} \tag{2.4}$$

It can be seen from Eq.(2.4) that when the incident light wavelength is constant, the half-angle of the Airy disk is inversely proportional to the particle diameter, that is, the smaller the particle diameter, the larger the central bright spot.

According to the Eq.(2.1) the diffracted light energy received by the *n*th annular photodetector is an integral of the light intensity over the area, which can be expressed as

$$e_n=\int_{R_{n,1}}^{R_{n,2}} I(\theta)\pi R dR \tag{2.5}$$

where $R_{n,1}$ is the inner diameter of the *n*th ring, $R_{n,2}$ is the outer diameter of the *n*th ring, n=1,2,…,N, N is the total number of rings of the annular photodetector. Normally, the diffraction method measures the angle within 5°, so for each point the scattering angle at the radius R can be approximated as

$$\theta\approx\sin\theta\approx\tan\theta=R/f \tag{2.6}$$

Substituting Eq.(2.1) and Eq.(2.6) into Eq.(2.5), after simplification, the relationship between the diffracted light energy and the particle size parameter on the *n*th ring detector is obtained.

$$e_n=\frac{I_0\pi D^2}{4}\int_{x_{n,1}}^{x_{n,2}}\frac{J_1^2(x)}{x}dx \tag{2.7}$$

where $x_{n,1}=\pi D\theta_{n,1}/\lambda$, $x_{n,2}=\pi D\theta_{n,2}/\lambda$. Applying the recursive formula of the Bessel function to discretize the above integral formula, the expression of the diffracted light energy received on the *n*th ring detector can be obtained:

$$e_n=I_0(\pi D^2/8)\left[J_0^2(x_{n,1})+J_1^2(x_{n,1})-J_0^2(x_{n,2})-J_1^2(x_{n,2})\right] \tag{2.8}$$

It can be seen from Eq.(2.8) that the light energy on each ring of the detector can be represented by the size parameter of the particle, and there is a clear mathematical relationship. Therefore, the particle size information can be obtained by measuring the light energy.

Extending the above conclusions to the case where there are N particles of diameter D in the measured area, the scattering phenomena between the individual particles are independent of each other under uncorrelated single scattering conditions, so the total light intensity should be the simple superposition of the diffraction intensity of the individual particles. The diffracted light energy expression on the nth ring detector is

$$e_n = NI_0(\pi D^2/8)\left[J_0^{\,2}(x_{n,1}) + J_1^{\,2}(x_{n,1}) - J_0^{\,2}(x_{n,2}) - J_1^{\,2}(x_{n,2})\right] \tag{2.9}$$

Further considering that the measured area has a plurality of particles having different diameters, wherein the number of particles having a diameter of D_i is N_i. Then the diffracted light energy expression on the nth ring detector is

$$e_n = I_0(\pi/8)\sum_i N_i D_i^{\,2}\left[J_0^{\,2}(x_{i,n,1}) + J_1^{\,2}(x_{i,n,1}) - J_0^{\,2}(x_{i,n,2}) - J_1^{\,2}(x_{i,n,2})\right] \tag{2.10}$$

where $x_{i,n,1} = \pi D_i\theta_{n,1}/\lambda$, $x_{i,n,2} = \pi D_i\theta_{n,2}/\lambda$. Converting the proportion of particles from quantity to mass, the conversion relationship between quantity and mass is as follows:

$$N_i = 6W_i/(\rho\pi D_i^3) \tag{2.11}$$

where Wi is the weight ratio, ρ is the density of the particles. Substituting Eq.(2.11) into Eq.(2.10)，we can obtain that :

$$e_n = C\sum_i (W_i/D_i)\left[J_0^{\,2}(x_{i,n,1}) + J_1^{\,2}(x_{i,n,1}) - J_0^{\,2}(x_{i,n,2}) - J_1^{\,2}(x_{i,n,2})\right] \tag{2.12}$$

where C=3I_0/4ρ, which is independent of the particle size, C is constant when the incident light intensity and particle density are determined, so it can be ignored during the operation. Write Eq. (2.12) as n independent equations, corresponding to n ring detectors:

$$\begin{aligned} e_1 &= t_{1,1}W_1 + t_{2,1}W_2 + t_{3,1}W_3 + \ldots + t_{K,1}W_K \\ e_2 &= t_{1,2}W_1 + t_{2,2}W_2 + t_{3,2}W_3 + \ldots + t_{K,2}W_K \\ \vdots \quad & \quad \vdots \qquad \vdots \qquad \vdots \\ e_M &= t_{1,M}W_1 + t_{2,M}W_2 + t_{3,M}W_3 + \ldots + t_{K,M}W_K \end{aligned} \tag{2.13}$$

$$t_{i,n} = (1/D_i)\left[J_0^{\,2}(x_{i,n,1}) + J_1^{\,2}(x_{i,n,1}) - J_0^{\,2}(x_{i,n,2}) - J_1^{\,2}(x_{i,n,2})\right] \tag{2.14}$$

Convert the Eq.(2.13) into matrix form:

$$E = TW \tag{2.15}$$

$$E=\begin{bmatrix} e_1 \\ e_2 \\ \vdots \\ e_{M-1} \\ e_M \end{bmatrix},\quad T=\begin{bmatrix} t_{1,1} & t_{2,1} & \cdots & t_{K-1,1} & t_{K,1} \\ t_{1,2} & t_{2,2} & \cdots & t_{K-1,2} & t_{K,2} \\ \vdots & \vdots & \ddots & \vdots & \vdots \\ t_{1,M-1} & t_{2,M-1} & \cdots & t_{K-1,M-1} & t_{K,M-1} \\ t_{1,M} & t_{2,M} & \cdots & t_{K-1,M} & t_{K,M} \end{bmatrix},\quad W=\begin{bmatrix} W_1 \\ W_2 \\ \vdots \\ W_{K-1} \\ W_K \end{bmatrix} \tag{2.16}$$

where E is the light energy distribution column vector, T is the light energy distribution coefficient matrix, W is the particle size distribution column vector.

Eq.(2.15) is the basic calculation formula based on the particle size measurement of Fraunhofer diffraction theory. The matrix equation method solves the equation to obtain the distribution information of the measured particles, and the integral transformation algorithm can inversely derive the light intensity from the measured light energy.

2.1.2. Measurement setup based on Fraunhofer diffraction

A typical schematic diagram of the particle sizing system based on the light scattering method is depicted in Figure 1. A collimated light beam is generated by a semiconductor laser. After passing through a beam expander and an aperture, the light illuminates the sample in the tested cell. Then the diffraction pattern is projected on the focal plane of the convex lens. Usually, a concentric photosensitive detector array is utilized here to receive the diffracted light.

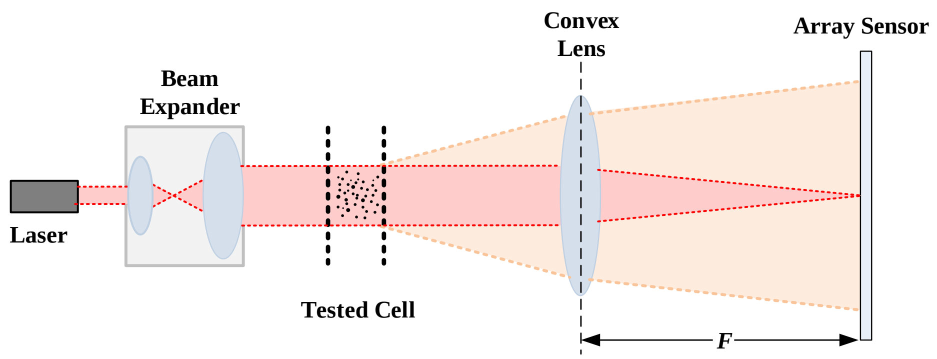

Figure 1 A typical schematic diagram of particle sizing system

The ring-shaped photodetector used in the conventional structure is generally semi-circular, and is a detection array composed of a plurality of concentric semi-circular photodiodes. Each ring is a detecting unit, and the output signal reflects the light energy in the detection range. The structure of the ring photodetector determines the matrix T of light energy distribution coefficients in Eq.(2.15). Since the intensity of the diffraction center of the Airy disk is much larger than that of other diffraction stripes, in practical applications, the center of the ring detector generally has a small hole with a radius of about 100 μm to let the central bright spot pass through.

From Eq.(2.6), we can know that the scattering angle at a fixed position of the focal plane of the lens is inversely proportional to the focal length of the Fourier lens. When the detection area is constant, the use of a lens with a longer focal length will move the range of detectable scattering angles to small size. The minimum detectable scattering angle determines the upper limit of the particle size measurement, and the maximum scattering angle that can be detected determines the lower limit of the particle size measurement. Therefore, the focal length of the lens can determine the measurement range of the laser particle size analyzer.

In practical applications, the lower limit of measurement of the diffractive laser particle size analyzer have more engineering significance, which is given by Eq.(2.17)[45]:

$$D_{\min} = 1.357 \frac{\lambda f}{\pi R_{\max}} \tag{2.17}$$

where $D_{\min}$ represents the smallest particle size that can be measured, λ represents the wavelength of the measured light, f represents the focal length of the receiving lens, $R_{\max}$ represents the maximum detection radius of the detector.

In the conventional detection structure, measurement errors are easily introduced because of inconsistent detector response between each ring of the ring-shaped photodetector. Therefore, spatial light modulation can be realized by Digital Micromirror Devices (DMD) to realize the detection of diffracted light intensity in combination with a single point detector [46]. It can avoid the effects of inconsistent responses between different detection units.

In actual measurement, the influence of environmental noise on the measurement data is a problem that should be considered. By reducing the sensitivity of the system to environmental noise to improve the accuracy of the measured light intensity data, the inversion accuracy can be improved and a more accurate particle size distribution curve can be obtained.

2.1.3. Diffraction intensity analysis

According to the Fraunhofer diffraction principle, the light energy after the light passes through the particle group is concentrated in a small forward angle. The farther the light stripe is from the center, the weaker the diffraction light intensity is. For accurate reconstruction, how to accurately measure the weak Light intensity signals should be researched. The difference in particle size distribution width affects the intensity distribution on the focal plane of the Fourier lens. For a unimodal distribution, the width of the particle size distribution is defined as the length of the particle size interval where the particle size distribution function is not zero. Figure 2 shows the changes in intensity distribution at a small forward angle（1-3°）slightly further from the lens focus, when the particle distribution width changed.

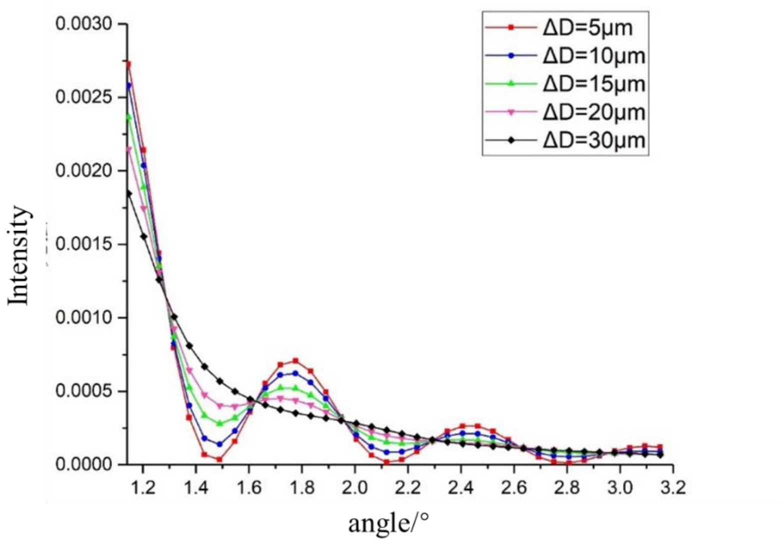

Figure 2 Diffractive light intensity signals with different particle distribution width

It can be seen that the narrower the particle group distribution is, the larger the fluctuation of the light intensity signal is. In order to accurately reconstruct the particle size distribution of the narrowly distributed particles, it is necessary to accurately measure the fluctuation of the weak light intensity. Therefore, relative to the broadly distributed particle group, measuring narrowly distributed particle populations requires a higher level of detection accuracy. It is necessary to study the corresponding improvement scheme to improve the detection capability of the weak signal of the particle size measurement system and improve the measurement accuracy.

2.2. Particle size inversion algorithm

Compared with the matrix equation algorithm, the integral transform algorithm has the advantages of fast calculation speed and no prior information. In this paper, the integral transform inversion algorithm is mainly studied. Before explaining the principle of the integral inversion algorithm, some common particle size distribution functions are introduced.

2.2.1. Common particle size distribution function

When the particle size of the particle group is the same, it is called a monodisperse system When the particle size of the particle group is different and there is a certain particle size distribution range, it is called a polydisperse system[47]. The particle size distribution of the particle group reflects the percentage of the particles of different diameters to the total number of particle groups. There are two commonly used particle size distribution expressions. One is the particle number distribution *N(D)* and it represents the percentage of the number of particles of diameter *D* to the total number of particles. The other one is the particle volume distribution *V(D*, which represents the relationship between the volume of particles of diameter *D* and the volume of the total particle group, the relationship between them can be expressed as

$$V(D) = N(D) \cdot \frac{\pi}{6} D^3 \tag{2.18}$$

The particle size distribution for the particles is usually described by the volume distribution. In practical applications, the above two distributions are divided into two types: frequency distribution and cumulative distribution. The frequency distribution refers to the percentage of particles in a certain size interval to the total particles. The cumulative distribution refers to the number of particles larger or smaller than a certain size. The percentage, in the standard particle identification manual, generally gives the cumulative distribution of particles.

Common particle size distribution functions are as follows:

1）Rosin-Rammler distribution（R-R distribution）

In 1933, Rosin and Rammler proposed a distribution to represent the particle size distribution of pulverized coal after grinding. The distribution function is an asymmetrical function. Subsequent studies have shown that most of the particle group distribution obtained by the crushing process can be represented by this distribution. So the Rosin-Rammler distribution is widely used in engineering determination [48]. Its expression is：

$$V\left(D\right) = \exp\left[-\left(\frac{D}{\bar{D}}\right)^k\right] \cdot \left(\frac{k}{\bar{D}^k}\right) \cdot D^{k-1} \tag{2.19}$$

where D is the particle size, $\bar{D}$ is a characteristic size parameter, which characterizes the average particle size of the particle group. K is called the particle size distribution parameter, which characterizes the distribution width of the measured particles. Figure 3 is the distribution curve function when $\bar{D}$=30 μm and k takes different values. It can be seen that the larger the value of k , the narrower the particle size distribution of the particle group.

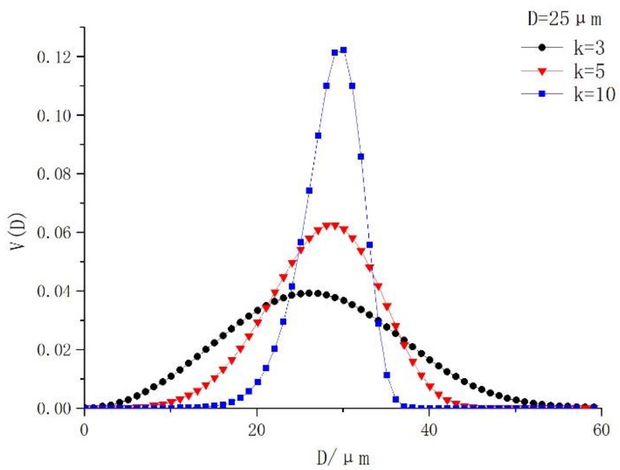

Figure 3　R-R distribution function curve of different distribution parameters

2）Lognormal distribution

Normal distribution can also be used to describe the particle size, but due to natural conditions, the particle size distribution function rarely conforms to the symmetry of the normal distribution. By taking the logarithm of each parameter in the normal distribution, the lognormal distribution can be obtained. This distribution is often used to describe the particle size distribution of particle groups such as soot, sand and aerosol, and its expression is:

$$V(D)=\frac{1}{\sqrt{2\pi}\cdot\ln\sigma}\exp\left[-\frac{1}{2}\left(\frac{\ln D-\ln\bar{D}}{\ln\sigma}\right)^2\right] \tag{2.20}$$

where $\bar{D}$ is the feature size parameter, ie the mathematical expectation, representing the average diameter; σ is the distribution parameter, ie the mathematical standard deviation, representing the range of the particle size distribution. Figure 4 is a distribution curve function diagram when $\bar{D}=30$ μm and σ takes different values. It can be seen that the smaller the σ is, the narrower the distribution is.

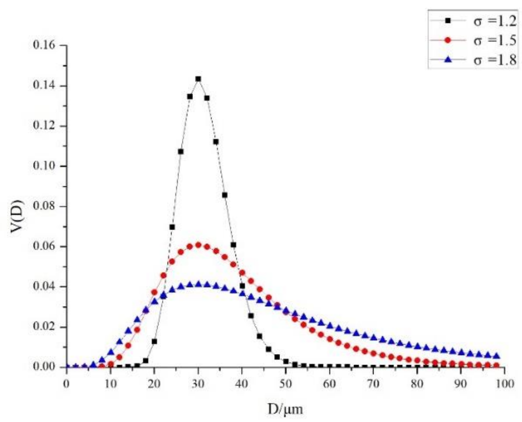

Figure 4　Lognormal distribution function curve of different distribution parameters

3）Normal bimodal distribution

In practical applications, the particle size distribution of some particle groups may have two or more peaks, and the multimodal function can be represented by a combination of different unimodal functions. Here, a bimodal normal distribution function expression is given:

$$V(D)=\frac{1}{\sqrt{2\pi}a\sigma_1}\exp\left[-\frac{1}{2}\left(\frac{D-\bar{D}_1}{\sigma_1}\right)^2\right]+\frac{1}{\sqrt{2\pi}b\sigma_2}\exp\left[-\frac{1}{2}\left(\frac{D-\bar{D}_2}{\sigma_2}\right)^2\right] \tag{2.21}$$

where $\bar{D}_1$、$\bar{D}_2$ respectively represent the expected values of the two unimodal distributions; σ_1、σ_2 represent the variances of the two unimodal distributions, respectively. *a, b* is the peak scale factor.

In this paper, in order to objectively evaluate accuracy of the reconstruction, the *s* value is defined as:

$$s=\sqrt{\frac{\sum_{i=1}^{N}(f_i-f_{ref,i})^2}{\sum_{i=1}^{N}f_{ref,i}^2}} \tag{2.22}$$

where f_i and $f_{ref,i}$ are the reconstruction distribution frequency and the original distribution frequency in the i-th particle size segment, respectively. The physical meaning is the relative deviation between the reconstructed distribution and the original distribution. The smaller the s value, the more accurate the reconstruction distribution is.

2.2.2. Inversion algorithm based on integral transform

The Chin-Shifrin algorithm is the most widely used integral transform inversion algorithm. As stated earlier, when there is only one particle of diameter D in the sample area, the diffraction intensity distribution on the detector of the focal plane of the condenser lens can be expressed by the Eq.(2.1), and when the sample to be tested is a particle group, under the single scattering condition, the diffraction intensity distribution is the superposition of the diffraction intensity distribution of all the particles. Let $f(x)$ be the continuous function of the particle size distribution of the particle size parameter x, then the angular distribution function of the diffraction intensity of the particle group can be expressed as

$$I(\theta)=I_0\int_0^\infty \frac{\pi^2 d^4}{16 f^2\lambda^2}[\frac{2J_1(x\sin\theta)}{x\sin\theta}]^2 f(x)dx \tag{2.23}$$

Eq.(2.23) is the first type of Fredholm integral equation [49]. Solve integral equations based on Bateman-Tichmarsh-Fox integral transformation formula:

$$\phi(t)=2\pi\int_0^\infty \mathrm{d}/\mathrm{d}t\left[tJ_\rho^2(rt)\right]r\varphi(r)\mathrm{d}r \tag{2.24}$$

$$\varphi(s)=-\int_0^\infty J_\rho(st)Y_\rho(st)t\phi(t)\mathrm{d}t \tag{2.25}$$

The expression of the distribution is

$$f(x)=-\frac{8\pi^3}{\lambda^2 I_0 x^2}\int_0^\infty x\theta J_1(x\theta)Y_1(x\theta)\frac{\mathrm{d}}{\mathrm{d}\theta}\left[\theta^3 I(\theta)\right]\mathrm{d}\theta \tag{2.26}$$

where Y_1 is the Bessel function of the second kind and first order, also known as the Neumann function. Eq.(2.26) is the expression of the classical Chin-Shifrin integral inversion algorithm. When analyzing the principle of Chin-Shifrin algorithm, the integral part of Eq.(2.26) can be divided into two parts:

$$\begin{cases} H_{cs}(x\theta)=J_1(x\theta)Y_1(x\theta)x\theta \\ E_{cs}(\theta)=\dfrac{\mathrm{d}}{\mathrm{d}\theta}\left(\theta^3 I(\theta)\right) \end{cases} \tag{2.27}$$

where $H_{cs}\left(x\theta\right)$ is the integral kernel function and $E_{cs}\left(\theta\right)$ is the differential function. It can be seen that the kernel function is independent of the measured light intensity distribution, and the differential function contains the measurement information. So the distribution information can be obtained through fitting a differential function by constructing a kernel function.

The Chin-Shifrin algorithm requires the integration interval of the scattering angle is $(0,+\infty)$, but in the actual measurement, the condition is difficult to satisfy. Therefore, when using the Chin-Shfrin algorithm for particle size reconstruction, certain errors are inevitably introduced. In order to improve the reconstruction accuracy, the selection of the integral scattering angle interval is particularly important. Meanwhile the Chin-Shifrin algorithm is sensitive to measurement noise. How to improve the anti-noise ability of the algorithm is also a research hotspot in recent years.

In 2009, a double integral inversion algorithm was proposed, which first rewrote the Eq.(2.23) into the following form:

$$\frac{4\pi^2 f^2\theta^2}{\lambda^2 I_0} I(\theta) = \frac{2}{\pi}\int_0^{\frac{\pi}{2}}\int_0^{\infty} J_2(2x\theta\sin\varphi)x^2 f(x)\mathrm{d}x\mathrm{d}\varphi \tag{2.28}$$

Applying the Schlomilch equation to solve the Eq.(2.28), the analytical solution can be obtained as follows:

$$\frac{\mathrm{d}\int_0^{\frac{\pi}{2}} \frac{(\theta\sin\varphi)^3}{\lambda^2 I_0} I(\frac{\theta\sin\varphi}{2})\mathrm{d}\varphi}{\mathrm{d}\theta} = \int_0^{\infty} xJ_2(\theta x)xf(x)\mathrm{d}x \tag{2.29}$$

where J_2 is the Bessel function of the first kind and second order. Using the Hankel transform, the Eq.(2.29) can be rewritten into a double integral form, which is the final expression of the double integral inversion algorithm:

$$f(x) = \frac{\pi^2 f^2}{\lambda^2 I_0 x}\int_0^{\infty}\theta J_2(\theta x)\frac{\mathrm{d}[\int_0^{\frac{\pi}{2}}(\theta\sin\varphi)^3 I(\frac{\theta\sin\varphi}{2})\mathrm{d}\varphi]}{\mathrm{d}\theta}\mathrm{d}\theta \tag{2.30}$$

Since the integral action in the derivative is equivalent to a low-pass filter in the double-integral algorithm, the double integral inversion algorithm is insensitive to measurement noise compared to the Chin-Shifrin algorithm. When the particle size is small, the double integral inversion algorithm exhibits better reconstruction performance than the Chin-Shifrin algorithm.

2.2.3. Limitation of integral transform inversion algorithm

The narrower the particle size distribution, the more uniform and stable the particles are. It is of great industrial significance to accurately reconstruct the narrow particle size distribution.

In order to study the accuracy of the existing integral transform inversion algorithm for the reconstruction of narrow particle size distribution and the resolving power for adjacent multi-peak distribution, several simulations have been done.

1）Narrow particle distribution reconstruction accuracy

For the Rosin-Rammler distribution, fixed $\bar{D}$=30 μm，k value increases from 3 to 40. For the lognormal distribution, fixed $\bar{D}$=30 μm， σ value increases from 1.005 to 1.200. The correspondence between the particle size distribution width and the distribution parameters is shown in Table 1:

Table 1　Correspondence between particle size distribution width and distribution parameters

Distribution parameter	Particle size distribution width（ μm）				
	<10	15	20	25	>30
k	>27	16	11	8	<6
σ	<1.05	1.08	1.11	1.14	>1.18

Reconstruct the above distribution by Chin-Shifrin algorithm and double integral algorithm respectively. The changes of the reconstruction accuracy (represented by s value) with the particle size distribution parameters are shown in Figure 5:

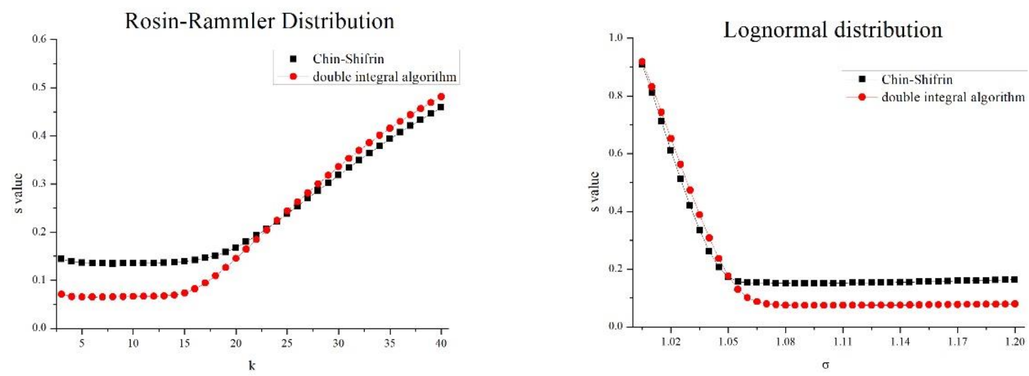

(a) Rosin-Rammler distribution　　　　**(b) Lognormal distribution**

Figure 5　Reconstruction of different distribution

It can be seen from the reconstruction results that for the Rosin-Rammler distribution and the lognormal distribution, when the particle distribution is wide, both integral inversion algorithms can accurately reconstruct the particle size distribution function, and the s value is lower than 0.2. When the particle size distribution width is narrower than 15 μm, the reconstruction accuracy of the two integral transform inversion algorithms decreases sharply with the decrease of the particle width. For the narrow distribution, the existing integral transform inversion algorithm cannot meet the reconstruction accuracy requirements.

2）Resolution of adjacent double peaks

Take the normal doublet as an example, fix one of the peaks $\bar{D}_1$=30 μm， $\sigma_1 = \sigma_2 = 0.5$， and take $\bar{D}_2$=35 μm and $\bar{D}_2$=40 μm respectively. The reconstruction results are shown in Figure 6 to Figure 7:

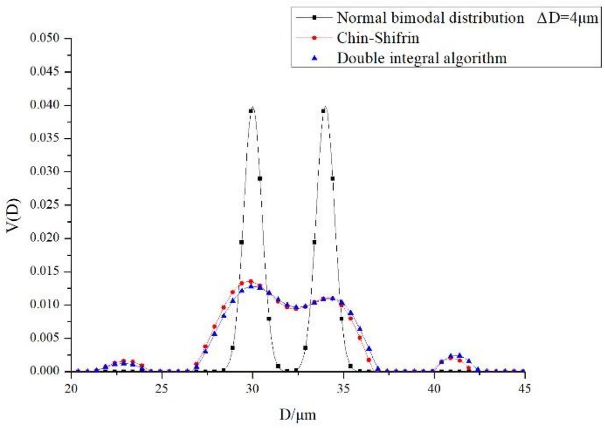

Figure 6　Normal bimodal distribution reconstruction results with peak spacing of 4 μm

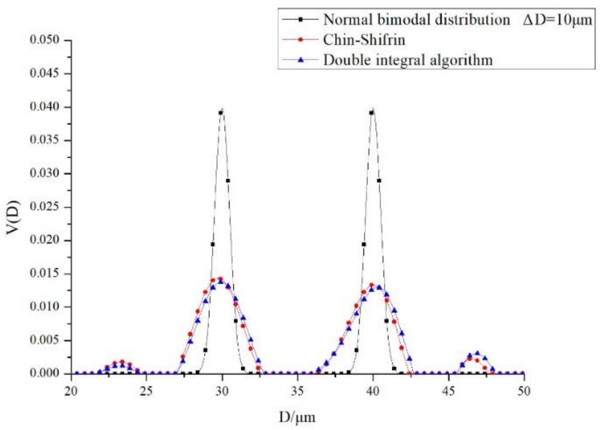

Figure 7　Normal bimodal distribution reconstruction results with peak spacing of 10 μm

It can be seen from the reconstruction results that when the Chin-Shifrin algorithm and the double integral inversion algorithm reconstruct the particle size distribution, fake peaks are generated at both sides of the main peak. When the peak spacing of the bimodal distribution is 4 μm, neither of the two integral transformation reconstruction algorithms can separate the two main peaks. That is, when the particle group contains multiple narrow distribution particles, the integral transformation algorithm cannot accurately distinguish the adjacent multi-peaks.

According to the above analysis, the Chin-Shifrin algorithm and the double integral inversion algorithm have large errors in reconstructing of the narrow particle size distribution. The central particle size value can be obtained, but the distribution function cannot be accurately reconstructed. It requires in-depth study on improving the reconstruction accuracy of the narrow distribution particle and distinguishing the adjacent multi-peaks.

Chapter 3 Inversion algorithm based on closed-loop control principle

When solving the inverse problem, the r reconstruction result can be improved by iteration. The iterative process is equivalent to the feedback effect in the closed-loop control theory. Therefore, the closed-loop control is introduced to the inversion algorithm to reduce the deviation, and the reconstruction result of the integral algorithm can be used as the initial distribution estimation of the iteration. Then, analogous to the principle of closed-loop control, the reconstruction error is regarded as the controlled object. According to the Fraunhofer diffraction theory, the particle size distribution of each reconstruction can be used to derive a set of light intensity distribution, and the light intensity distribution value is used for feedback, and the light intensity deviation is corrected. Recently, PID (Proportional–Integral–Derivative) controller is the most widely used closed-loop controller. Its mathematical model is simple. Only need to determine the proportional, differential and integral parameters to get good control effect. By introducing PID controller into a particle size inversion algorithm, the reconstruction accuracy of the narrow distribution particle size distribution can be improved by iterative method. However, the traditional PID controller parameters are manually selected. It is necessary to obtain a suitable PID parameter under a certain condition through massive calculation. In recent years, the introduction of intelligent PID control theory has realized the adaptive selection of controller parameters. The advanced closed-loop control theory is introduced into the integral inversion algorithm, and a high-precision reconstruction algorithm that adaptively adjusts the parameters and is suitable for particle size distribution reconstruction of different particle groups is obtained.

3.1. Reconstruction algorithm based on closed-loop control principle

Considering the inversion algorithm as the controlled system, the PID controller realizes the tracking of the input signal. Through the Fraunhofer diffraction feedback loop, the deviation of the reconstruction of narrow particle size distribution due to the limited diffraction angle can be corrected. The structural block diagram of the algorithm can be expressed as:

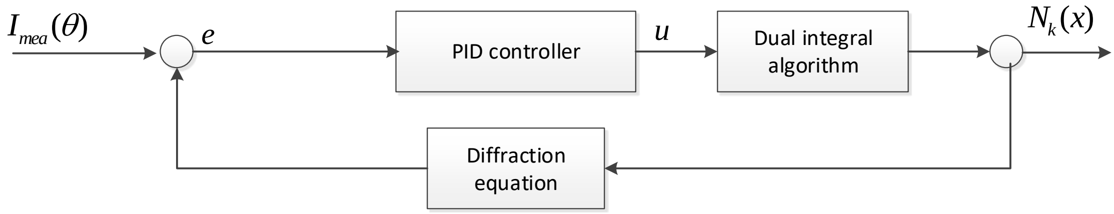

Figure 8 Structure of algorithm based on closed-loop control theory

In Figure 8, u represents the controller output, $N(x)$ represents the particle size distribution function. The algorithm flow can be described as follows: the measured the light intensity value

I is the input of the algorithm, and initialize the feedback light intensity to zero. Then calculate the difference between the input light intensity and the feedback light intensity, and the difference is sequentially passed through the PID controller and the basic integral inversion algorithm. After that output the calculated particle size distribution function of this time. From this distribution, the light intensity curve under the Fraunhofer diffraction condition can be calculated, and the obtained light intensity distribution is used as the feedback light intensity to participate in the next iteration. When the difference between the input and the feedback light intensity is less than a certain value, the iteration is stopped. The particle size distribution function of the output is the reconstruction result.

From the previous analysis, it can be seen that for the non-narrow-distributed particle, the double integral inversion algorithm has the higher reconstruction accuracy than the Chin-Shifrin algorithm. Therefore, the double integral inversion algorithm is used as the basic algorithm in this topic.

For the positional PID controller, after the output control quantity has reached the maximum value, the error will still accumulate due to the integral action, it will cause the system to enter the saturation zone, so it is difficult to quickly respond to the error of the reverse change. In addition, the positional PID controller needs to record the error value of each iteration, the calculation amount is large, and the memory is occupied. Therefore, the subject adopts the incremental PID as the introduced control algorithm, and the incremental PID has no accumulation of errors. The reliability of the iteration formula is as follows:

$$\begin{cases} \Delta u^{(k)} = K_p^{(k)} \times (e^{(k)} - e^{(k-1)}) + K_i^{(k)} \times e^{(k)} + K_d^{(k)} \times (e^{(k)} - 2e^{(k-1)} + e^{(k-2)}) \\ u^{(k)} = u^{(k-1)} + \Delta u^{(k)} \end{cases} \tag{3.1}$$

In order to verify the feasibility of the proposed algorithm, a set of controller parameters ($K_p = 3.5,\ K_i = 1.0,\ K_d = 0.1$) is selected by choosing from a huge number of calculations. And the Rosin-Rammler distribution, the lognormal distribution and the normal bimodal distribution are reconstructed respectively. The three groups were set to narrow particles, where the Rosin-Rammler distribution parameters are set to $\bar{D}$=27.3 μm，k=30; The lognormal distribution parameters are set to $\bar{D}$=46.3 μm，σ=1.02，The bimodal normal distribution parameters are set to a=b=0.5，$\bar{D}_1$=32.0 μm，$\bar{D}_1$=36.0 μm，$\sigma_1 = \sigma_2 = 0.4$. The reconstruction results for the three different distributions are shown in Figure 9 to Figure 11.

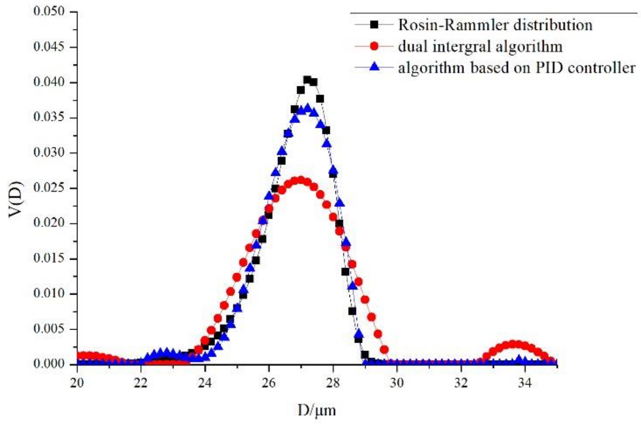

Figure 9 Rosin-Rammler distribution reconstruction results

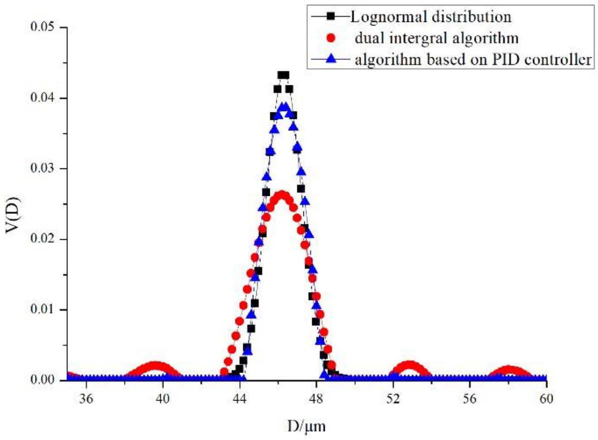

Figure 10 Lognormal distribution reconstruction result

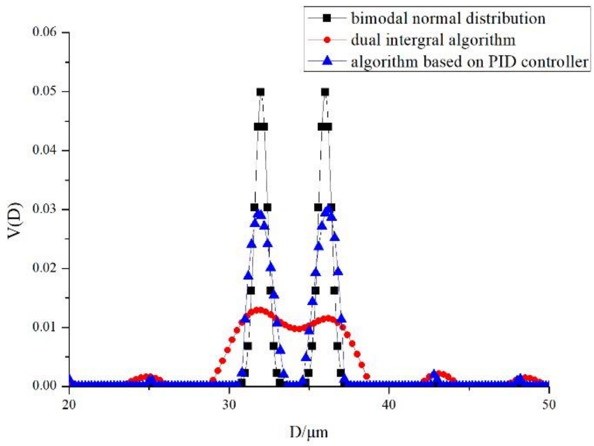

Figure 11 Bimodal normal distribution reconstruction result

The reconstruction results show that the proposed integral algorithm has a significant improvement over the traditional double integral inversion algorithm in the narrow particle size distribution reconstruction. For the Rosin-Rammler distribution, the lognormal distribution and the normal bimodal distribution, the reconstructed s values are reduced from 0.33, 0.36, and 0.77 to 0.09, 0.12, and 0.41 respectively.

However, the parameters choosing need massive calculation, and the obtained parameters cannot be applied to all particle distributions. Therefore, it is necessary to adopt a more advanced PID controller to achieve adaptive selection of parameters.

3.2. Inversion algorithm based on neural network model

3.2.1. Principle of the algorithm

Neural Network is based on a collection of connected units or nodes called artificial neurons, which loosely model the neurons in a biological brain. Each connection, like the synapses in a biological brain, can transmit a signal from one artificial neuron to another[50]. The structure of a typical three-layer neural network model is shown in Figure 12. The neural network has strong self-learning ability. Its multi-layered neuron structure can realize approximation of arbitrary functions. The closed-loop control theory based on neural network model is introduced into the reconstruction process, which can realize adaptive selection of parameters.

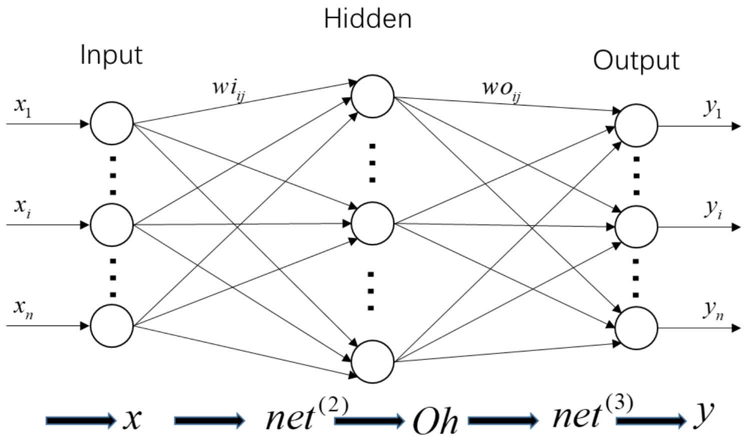

Figure 12 Neural network structure

Each circle in the figure represents a node in the neural network model, also called a neuron, x represents the input signal of the neural network model, and y represents the output signal of the neural network model, $net^{(2)}$、$net^{(3)}$ representing the input of the hidden layer and the output layer respectively. Oh represents the output of the hidden layer, wi_{ij} represents the weight of each node of the input layer to the hidden layer, wo_{ij} represents the weight of each node of the hidden layer to the output layer, and the input value of each layer node is obtained by summing the output values of the upper node and the corresponding weight products. The typical three-layer neural network model calculation process is:

$$\begin{cases} net_i^{(2)} = \sum_{j=o}^{m} wi_{ij} x_j \\ Oh = f(net_i^{(2)}) \\ net_i^{(3)} = \sum_{j=o}^{q} wo_{ij} Oh_j \\ y_i = g(net_i^{(3)}) \end{cases} \tag{3.2}$$

Backpropagation (BP) is a method for gradient calculation in artificial neural networks, which can correct the weight of each layer in the neural network[51]. Let the algorithm evaluation function be

$$E = \frac{1}{2}(r_k - y_k)^2 \tag{3.3}$$

where r represents the desired output. According to the gradient descent method, the weight coefficient is modified. In order to speed up the convergence, the inertia link is generally added in the correction, and the weight can be corrected by the Eq.(3.4):

$$\Delta w_k = -\eta \frac{\partial E_k}{\partial w} + \alpha \Delta w_{k-1} \tag{3.4}$$

where η is the learning rate， α is the inertia coefficient.

To realize the computational advantages of the neural network model and realize the effect of automatically selecting different controller parameters, it is necessary to design the neural network model reasonably. There is no uniform standard for the design of neural network models. In this research, the inputs of the neural network model (x_i) are the measured light intensity ($I_{mea}(\theta)$)、feedback light intensity ($I_{inv}(\theta)$) and deviation between the two (e). The number of layer neurons is three, corresponding to the three parameters *Kp, Ki, Kd* of the PID controller. In order to achieve reasonable self-learning, the selection of the number of neurons in the hidden layer is very important. Excessive neurons in the hidden layer will lead to over-fitting. Too few neurons will lead to inaccuracy learning, and the results fall into local optimum. Usually the number of neurons in the hidden layer should be 1.2-1.5 times the number of neurons in the input layer. In this subject, the number of neurons in the hidden layer is selected as 1.3 times of the number of neurons in the input layer.

The neural network PID structure is introduced into the reconstruction algorithm, and each iteration can be regarded as a training of the neural network. The structure of the proposed reconstruction algorithm is shown in Figure 13:

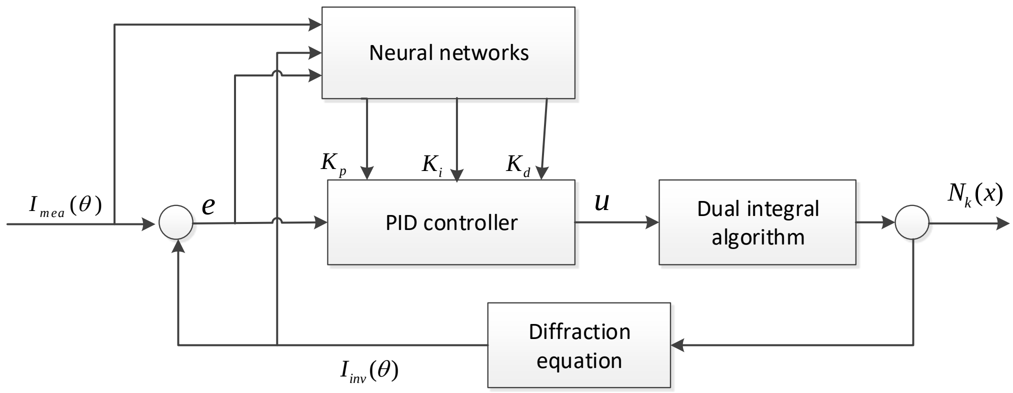

Figure 13 Structure of algorithm based on Neural networks

The algorithm consists of two processes, one is the iterative calculation of particle size distribution: the input signal and output signal of each layer of the neural network can be obtained by Eq.(3.2), and three parameters *Kp, Ki, Kd* are output to the PID controller. The light intensity error signal passes through the controller in turn, and the double integral inversion algorithm obtains the particle size distribution function of the current output, and calculates the input diffraction intensity to the output particle size distribution. The other one is the neural network completes the online adjustment process of the controller parameters through self-learning: the feedback light intensity obtained by the Fraunhofer diffraction formula of the output particle size distribution, combined with the neural network model, through the BP algorithm, the weight of each layer of the neural network model is updated, and automatically adjust the next iteration controller parameters. In this topic, the activation functions of the hidden layer and the output layer are selected as follows:

$$\begin{cases} f(x) = \tanh(x) = \dfrac{e^x - e^{-x}}{e^x + e^{-x}} \\ g(x) = \dfrac{1}{2}\left(1 + \tanh(x)\right) = \dfrac{e^x}{e^x + e^{-x}} \end{cases} \tag{3.5}$$

In the actual calculation, the error derivative in Eq.(3.4) can be expressed as

$$\begin{cases} \dfrac{\partial E}{\partial wo} = \dfrac{\partial E}{\partial I_{inv}(\theta)} \cdot \dfrac{\partial I_{inv}(\theta)}{\partial u(\theta)} \cdot \dfrac{\partial u(\theta)}{\partial K} \cdot g'(net^{(3)}) \cdot \dfrac{\partial net^{(3)}}{\partial wo} \\ \dfrac{\partial E}{\partial wi} = \dfrac{\partial E}{\partial I_{inv}(\theta)} \cdot \dfrac{\partial I_{inv}(\theta)}{\partial N(x)} \cdot \dfrac{\partial N(x)}{\partial u(\theta)} \cdot \dfrac{\partial u(\theta)}{\partial K} \cdot g'(net^{(3)}) \cdot \dfrac{\partial net^{(3)}}{\partial Oh} \cdot f'(net^{(2)}) \cdot \dfrac{\partial net^{(2)}}{\partial wi} \end{cases} \tag{3.6}$$

The weight of each layer of the neural network needs to be initialized. The selection of the initial weight directly affects the self-learning results. If the initial value of the weight is all zero, the weight of the structure will be stable to the same value due to the symmetry of the structure. Usually, the initial weight value of the neural network should be a randomly selected smaller value to invalidate the symmetry and implement the weight update for each iteration.

The final algorithm implementation process is as follows:

（1）Determine the neural network structure (the number of nodes in each layer), initialize the weights of each layer of the neural network, and select the learning rate η and the inertia coefficient α to be 0.25 and 0.05 respectively; set the iterative stop condition ε; initialize the input light intensity to the set value I_{mea}, and the feedback light intensity is $I_{inv}^{(0)}=0$. Calculate the input and output values of each layer of the neural network and finally obtain the proportional, integral and differential parameters of the PID controller as Kp、Ki、Kd;

（2）The difference $e^{(k)}$ between the input light intensity I_{mea} and the feedback light intensity $I_{inv}^{(k)}$ is input to the controller of the current parameter to obtain the output quantity *u(k)*. *u(k)* through the double integral inversion algorithm to obtain the current reconstructed particle size distribution function $N_k(x)$;

（3）Perform neural network learning. First adjust the weight of the hidden layer to the output layer wo， further adjust the weight wi of the input layer to the hidden layer, obtain the weight distribution of each layer of the new neural network, and calculate the controller parameters for the next iteration;

（4）Calculate the light intensity distribution $I_{inv}^{(k+1)}$ under the current particle size distribution $N_k(x)$, repeat steps (2) to (4) until the error between the input light intensity and the feedback light intensity is less than the set value ε, and stop iterating. The particle size distribution function is the final calculated inverse particle size distribution.

3.2.2. Numerical simulation

In order to verify the feasibility of the improved granularity inversion algorithm based on neural network PID, three common distributions are numerically simulated and reconstructed respectively. The parameters of the three distributions are set as described above.

1）Retrieval with Noise-free Data

The numerical simulation results when there is no noise interference are shown in Figure 14 to Figure 16.

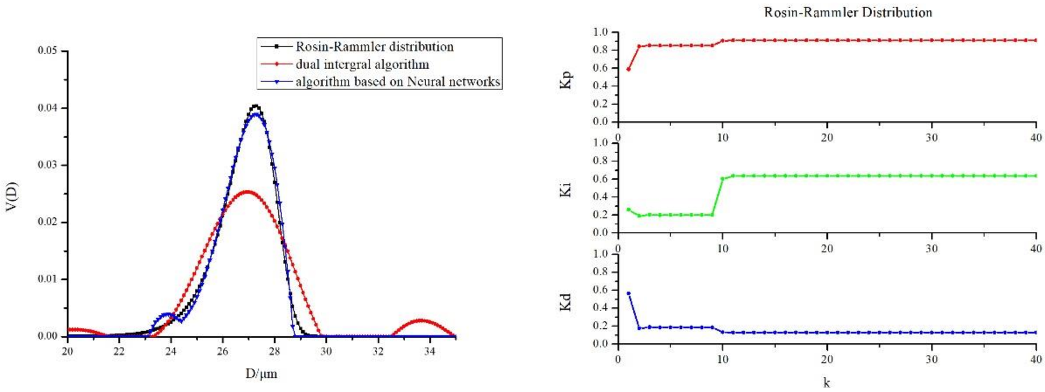

(a) Reconstruction result **(b) self-adapting parameters**

Figure 14 Rosin-Rammler distribution

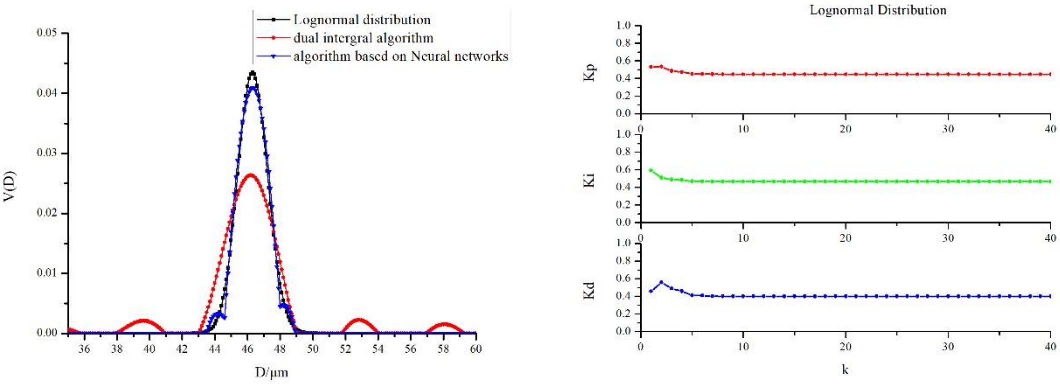

(a) Reconstruction result **(b) self-adapting parameters**

Figure 15 Lognormal distribution

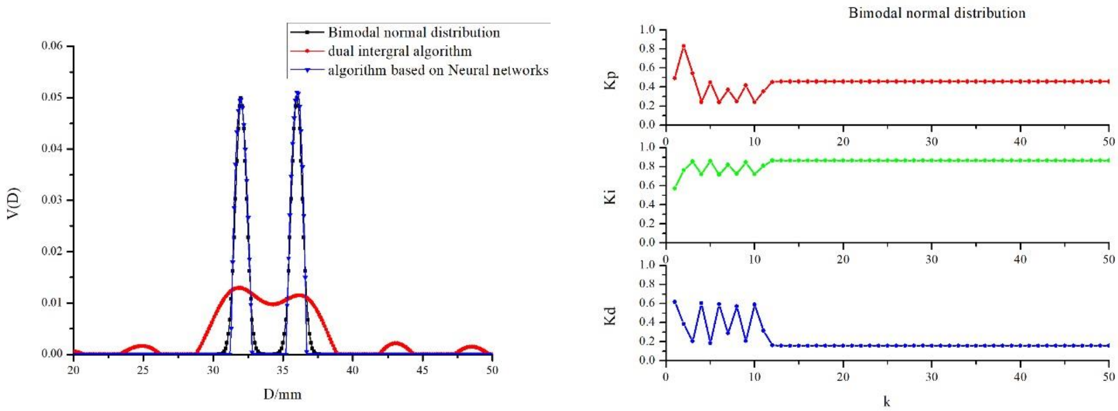

(a) Reconstruction result **(b) self-adapting parameters**

Figure 16 Bimodal normal distribution

The results show that the s value of the reconstruction algorithm based on neural network model is significantly smaller than that of the double integral inversion algorithm. For Rosin-Rammler distribution and lognormal distribution, the *s* value decreases by about 0.02. For the normal bimodal distribution, the improved algorithm based on the neural network model can not only distinguish the adjacent narrow-distributed double peaks, but also greatly improve the reconstruction accuracy. The number and intensity of fake peaks in the reconstruction results of the improved algorithm are smaller than that of the double-integral inversion algorithm, indicating that the application of neural network PID model can effectively suppress the generation of fake peaks and improve the quality of inversion. Meanwhile, the parameters of the PID controller are automatically adjusted with each iteration, and finally stabilized to a certain value, which proves that the neural network model can achieve adaptive selection of PID parameters without human intervention.

2）Retrieval with noise-contaminated data

To evaluate the reconstruction results of the reconstruction algorithm under different noise levels, the multiplicative noise with a signal-to-noise ratio of 20-60 dB is added to the light intensity signal. In order to avoid the influence of chance factors, the neural network structure parameters and weights are kept unchanged during reconstruction, and 50 repeated calculations are performed for each noise level. Figure 17 to Figure 19 show the reconstruction accuracy (s value) at different noise levels. The reconstruction accuracy of the reconstruction algorithm changes with the noise level. The mean value of the s value in the graph represents the average reconstruction accuracy under different noise levels, and the error bar reflects the stability of the reconstruction algorithm. It can be seen from the figure that for all these three distributions, the reconstruction by the algorithm based on the neural network model is more accurate at each noise level. But when the noise level is lower than 30 dB, the standard deviation of the proposed algorithm is significantly larger than that of the double integral inversion algorithm, indicating that the improved algorithm is more sensitive to noise at low noise levels. In the actual measurement, the signal-to-noise ratio of the measured signal is about 40 dB, and in this condition the reconstruction effect of the improved inversion algorithm is obviously better than the traditional method and the reconstruction result is stable.

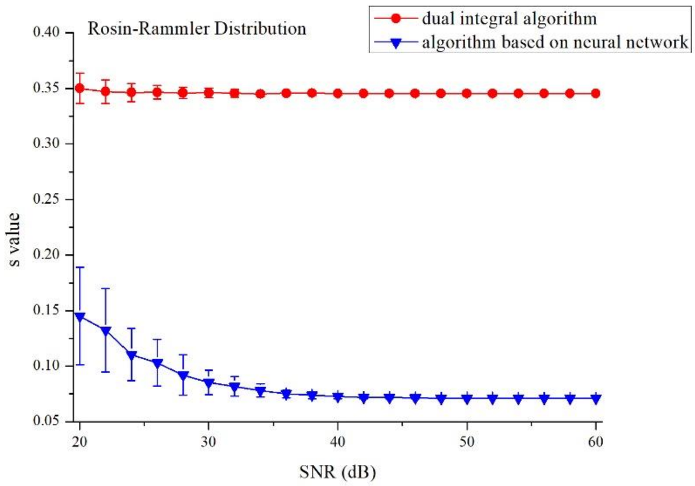

Figure 17 Reconstruction *s* value of Rosin-Rammler distribution under different noise levels

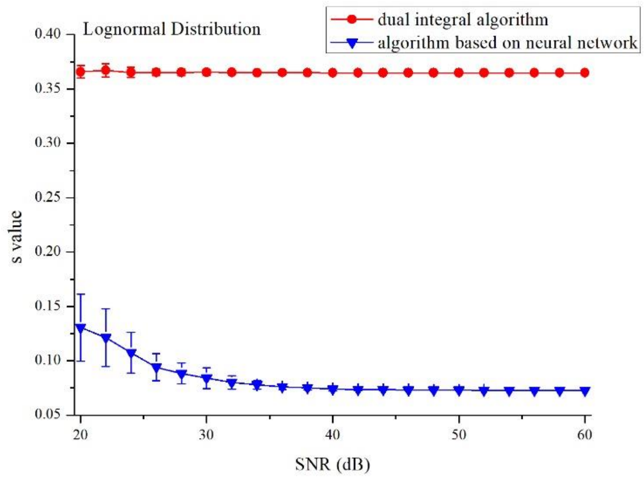

Figure 18 Logarithmic normal distribution reconstruction s values under different noise levels

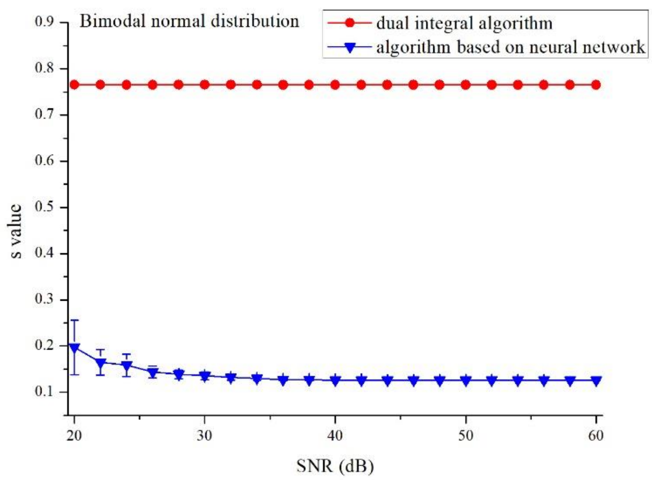

Figure 19 Normal s-peak distribution reconstruction s value under different noise levels

3.2.3. Influence of random initialization weight

The weight coefficient of the neural network model needs to be initialized to a random small amount. For different distributions, the reconstruction of the particle size range results in a change in the length of the input light intensity column vector, which in turn causes the weight coefficient dimension to change. Therefore, the process of randomly initializing the weight will introduce errors into the reconstruction result. Fifty reconstructions are performed under the noiseless situation, and the weight coefficients of the neural network model are randomly initialized each time. Figure 20 to Figure 22 show reconstruction results for different initial weights. The results show that the random initialization weight will cause large fluctuations in each reconstruction result, and even fake peaks.

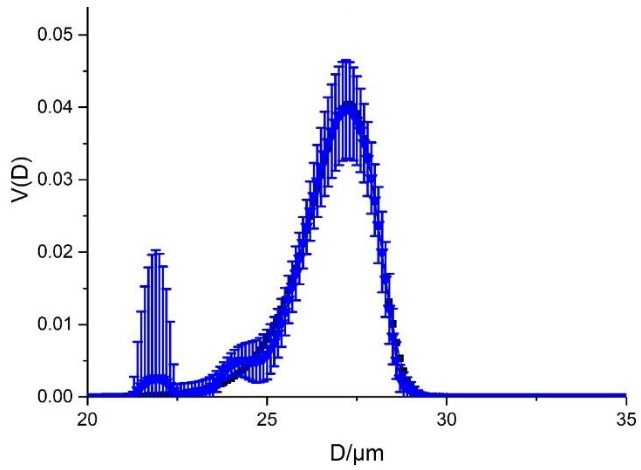

Figure 20 Reconstruction of Rosin-Rammler distribution under random weight selection

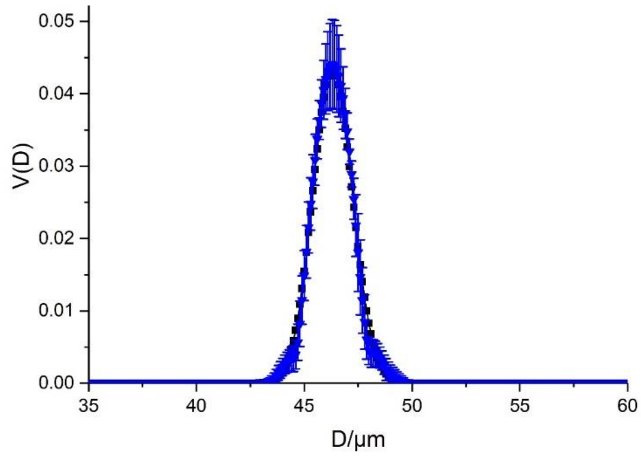

Figure 21 Reconstruction of Lognormal distribution under random weight selection

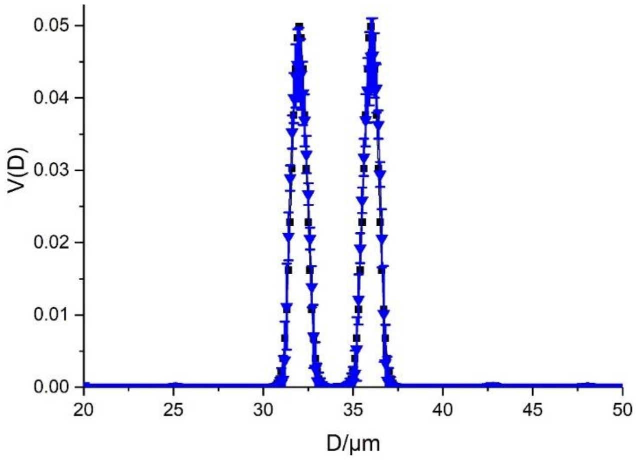

Figure 22 Reconstruction of Bimodal normal distribution under random weight selection

3.3. Inversion algorithm based on fuzzy control

The reconstruction result of the algorithm based on neural network model is closely related to the selection result of random weight. In order to solve the problem that the reconstruction result is sensitive to the initial weight selection during the actual measurement reconstruction, the fuzzy control theory instead of neural network model is introduced to the algorithm to realize the adaptive adjustment of the parameters.

3.3.1. Principle of the algorithm based on fuzzy control

The theory of fuzzy was first proposed by L.A.Zadeh in 1965 [52]. Fuzzy control is a kind of intelligent control. According to system theory, any intelligent behavior can be regarded as a mapping from an input to an output. In general, this mapping is difficult to express with an accurate mathematical model, so an adaptive intelligent control theory is proposed. The essence of fuzzy control is based on the control of knowledge or rules. According to the experience of field operators or experts in related fields, the control rules of mathematical models are abstracted into language control rules. When designing fuzzy controllers, it is not necessary to establish strict mathematic model for controlled objects, so the design is simple and has broad application prospects[53].

There are four main steps in the fuzzy controller to realize fuzzy control, namely: fuzzification of the input accurate quantity, establishment of fuzzy mapping rules, fuzzy inference, and conversion of fuzzy output into accurate quantity. The principle can be represented by Figure 23：

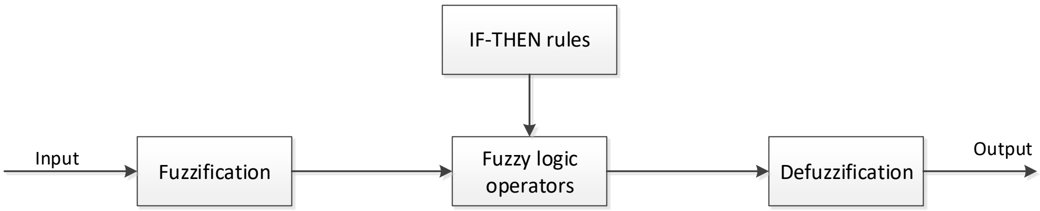

Figure 23 Basic schematic diagram of fuzzy process

The fuzzy controller can be used to adaptively select the PID parameters. It is essentially a fuzzy system in which the inputs are the error *e* between the input quantity and the feedback quantity and the error derivative *ec*. The PID controller parameters are the output variables. By establishing the fuzzy inference rules, the changes of the three parameters *Kp*, *Ki*, and *Kd* are adjusted to realize the correction and adaptive selection of the controller parameters. After introducing the fuzzy PID into the dual integral inversion algorithm, the algorithm structure is shown in Figure 24:

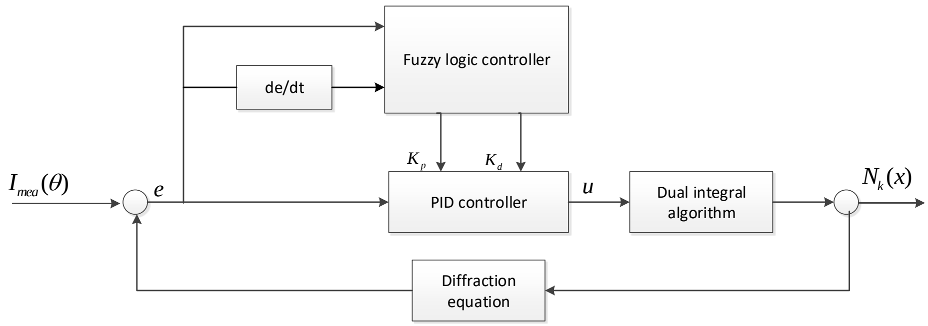

Figure 24 Algorithm structure based on fuzzy control theory

The first step in designing a fuzzy controller is to determine the input value domain and determine the fuzzy logic operators. For particle size distribution reconstruction, the input error should be the difference between the measured light intensity and the feedback light intensity. For comparison, the measured light intensity for reconstruction will be normalized. Then the difference between the two is a column vector whose value is less than 1, and the 2-norm of the vector is used as the input error *e*. According to experience, the value of *e* is in the range of [0, 1].

Traditional fuzzy controllers generally need to implement fuzzy control of three-parameter output. To achieve fuzzy control of three-parameter changes, seven fuzzy linguistic variable values must be defined in the input and output intervals, namely NB, NM, NS, ZE, PS, PM,PB, which represent negative large value, negative median, negative small value, zero, positive small value, positive median value, positive value respectively. By correspondence between the fuzzy interval of the two input quantities and the possible outputs of the three outputs, the prediction of the parameter output value is realized, and the automatic adjustment of the controller parameters is realized.

In the closed-loop iterative algorithm designed in this paper, the double integral inversion algorithm and the Faunhofer diffraction formula are mutually inverse processes, and the product of the transfer functions can be regarded as constant 1. Only consider the effect of the incremental PID on the output, and perform Z-transformation on the iterative formula of the incremental PID. The result is:

$$\frac{U[\mathrm{z}]}{E[\mathrm{z}]}=\frac{K_p\cdot(1-\mathrm{z}^{-1})+K_i+K_d\cdot(1-2\cdot\mathrm{z}^{-1}+\mathrm{z}^{-2})}{1-z^{-1}} \tag{3.7}$$

Apply the final value theorem:

$$\begin{aligned} f(\infty)&=\lim_{z\to1}(\frac{\mathrm{z}-1}{z})\cdot\frac{U[\mathrm{z}]}{E[\mathrm{z}]}\\ &=\lim_{z\to1}[K_p\cdot(1-\mathrm{z}^{-1})+K_i+K_d\cdot(1-2\cdot\mathrm{z}^{-1}+\mathrm{z}^{-2})]\end{aligned} \tag{3.8}$$

Finally get:

$$f(\infty)=K_i \tag{3.9}$$

It can be seen from Eq.(3.9) that the final steady state value of the incremental PID control is only related to the parameter *Ki*.Therefore, by fixing the value of the parameter *Ki* and adjusting the parameters *Kp*、*Kd* online, the stability of the reconstruction algorithm can be improved.

In this subject, the left boundary of the domain is selected as the Z-type membership function (zmf) with a slow change on the right side, and the right boundary of the domain is selected as the S-type membership function (smf) with a slow change on the left. Both of them are based on the spline function. The curve of the middle region of the domain is selected as a triangular membership function (trimf) with simple operation, high sensitivity and symmetry. The function expression is as follows:

$$\mu(x)=\begin{cases}0,\ x<a\\ \dfrac{x-a}{b-a},\ a\le x\le b\\ \dfrac{x-a}{c-b},\ b\le x\le c\\ 0,\ x>c\end{cases} \tag{3.10}$$

where the parameters *a*，*c* determine the zero position of the triangle function, *b* determines the peak position of the function.

Through the above analysis, fixed $Ki=2$, the fuzzy controller with two inputs and two outputs is selected to realize the adaptive adjustment of the two parameters of *Kp* and *Kd*. The range of the variables in the fuzzy controller is: $e \in [0,1]$、 $ec \in [-0.1, 0.1]$、 $K_p \in [-5.0, 5.0]$、 $K_d \in [-1.0, 1.0]$. Different from the fuzzy control of the three-parameter output, the fuzzy controller of the two-parameter output only needs to define three fuzzy linguistic variables in the fuzzy domain, namely negative (N), zero (Z) and positive (P). The membership functions of the error e, the error derivative ec, the parameters *Kp* and *Kd* are shown in Figure 25 to Figure 26 :

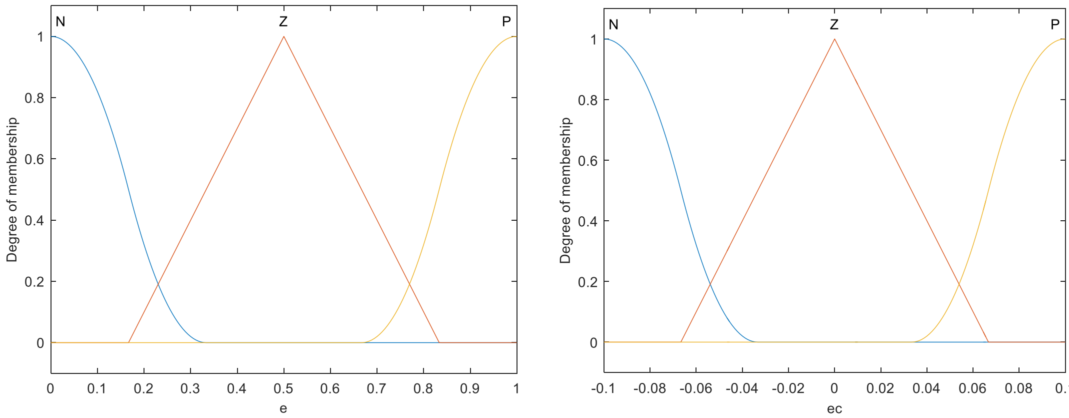

(a) membership function of error *e* **(b) membership function of error *ec***

Figure 25 Fuzzy control input membership functions

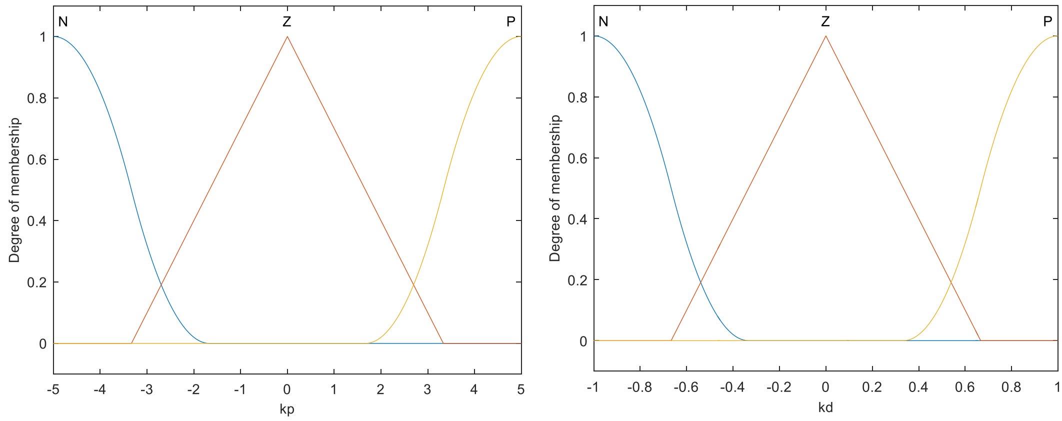

(a) membership function of error *Kp* **(b) membership function of error *Kd***

Figure 26 Fuzzy control output membership functions

In this paper, for the adaptive adjustment of the two controller parameters, the fuzzy control table is shown in Table 2 to Table 3 [54]:

Table 2 Fuzzy control table for parameter *Kp*

ec	e		
	N	Z	P
N	Z	Z	P
Z	Z	P	P
P	Z	P	P

Table 3 Fuzzy control table for parameter *Kd*

ec	e		
	N	Z	P
N	Z	P	Z
Z	Z	P	Z
P	Z	P	Z

In the table, each cell corresponds to an IF-THEN fuzzy rule, taking the first column of the first row of the fuzzy control table of the parameter *Kp* as an example, and the fuzzy rule expressed as a natural language is:

If (e is N) and (ec is N) then (ΔK_p=Z).

After the fuzzy logic processing, the final precise control quantity needs to be obtained by defuzzification. In this paper, the most common defuzzification operator, the center of gravity defuzzification operator, is used to determine the final output's determined value by calculating the center of the region surrounding the membership function curve. The calculation formula of the center of gravity defuzzification operator is:

$$y^* = \frac{\int_V \mu(y)\cdot y\mathrm{d}y}{\int_V \mu(y)\mathrm{d}y} \tag{3.11}$$

where V is the fuzzy domain, y is the fuzzy value, y^* is the corresponding clear amount. The relationship between the resulting output parameters and the input parameters is shown in Figure 27.

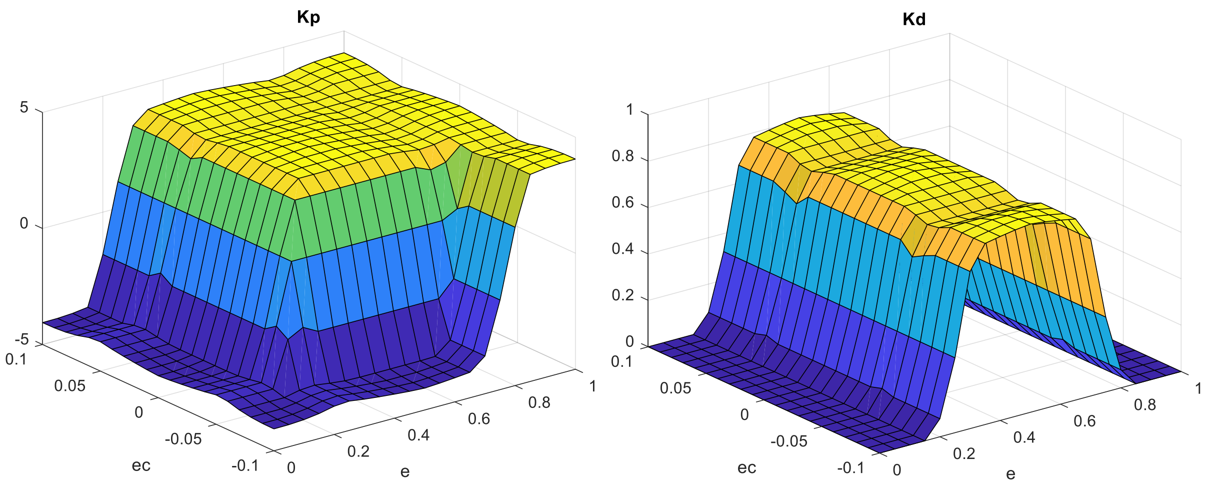

(a) the relationship between *Kp* and input values **(b) the relationship between *Kd* and input values**

Figure 27 Fuzzy controller output variable and input variable relationship

3.3.2. Simulation of the algorithm based on Fuzzy control

In order to verify the feasibility of the inversion algorithm based on fuzzy control theory, simulations without and with noise have been done. The parameters of the three distributions are set as described above.

1）Retrieval with Noise-free Data

Figure 28 to Figure 30 respectively show the reconstruction results of three different distributions using different reconstruction algorithms. The reconstruction accuracy of the three methods (indicated by the s value) is compared in Table 4.

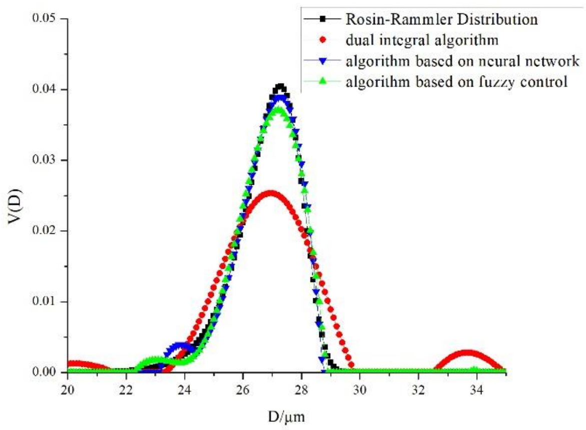

Figure 28　Rosin-Rammler distribution reconstruction results

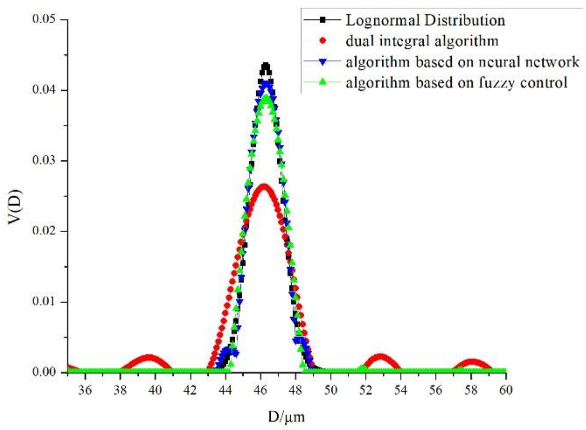

Figure 29　Lognormal distribution reconstruction result

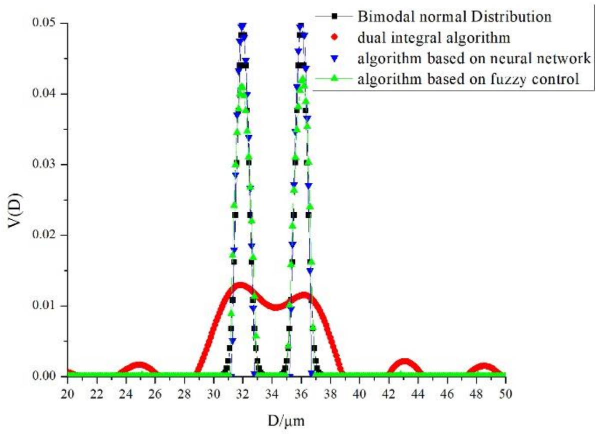

Figure 30 Bimodal normal distribution reconstruction result

Table 4 Reconstruction accuracy (s value) of different reconstruction algorithms

Reconstruction algorithm	Particle size distribution		
	Rosin-Rammler distribution	Lognormal distribution	Normal bimodal distribution
Double integral algorithm	0.33	0.36	0.77
Algorithm based on neural network model	0.07	0.08	0.15
Algorithm based on fuzzy control theory	0.09	0.12	0.18

The reconstruction results show that although the accuracy of reconstruction algorithm based on fuzzy control theory is slightly lower than that of the integral algorithm based on neural network model, its reconstruction result is still better than the traditional dual integral algorithm, and it can accurately distinguish adjacent double peaks.

2）Retrieval with noise-contaminated data

A multiplicative noise of 20-60 dB is added to the light intensity signal, and in order to avoid contingency factors, 50 repeated calculations are performed for each noise level. Figure 31 to Figure 33 show the reconstruction accuracy under different noise levels. It can be seen from the results that for all the three distributions, although the s value of the improved fuzzy control theory algorithm is slightly larger than the s value of the algorithm based on the neural network model, it is still obvious less than the dual integral inversion algorithm. For the unimodal distribution, the reconstructed s value of the proposed algorithm does not exceed 0.15, and at low noise level, the error bar of the proposed algorithm is slightly smaller than the neural network model algorithm, which means the proposed algorithm has stronger anti-noise ability. For bimodal normal distribution, the s value of the new improved algorithm does not exceed 0.3, and the error bar is larger when the signal-to-noise ratio is lower than 35 dB, indicating that accurate reconstruction of multi-peak distribution requires more accurate measurement data.

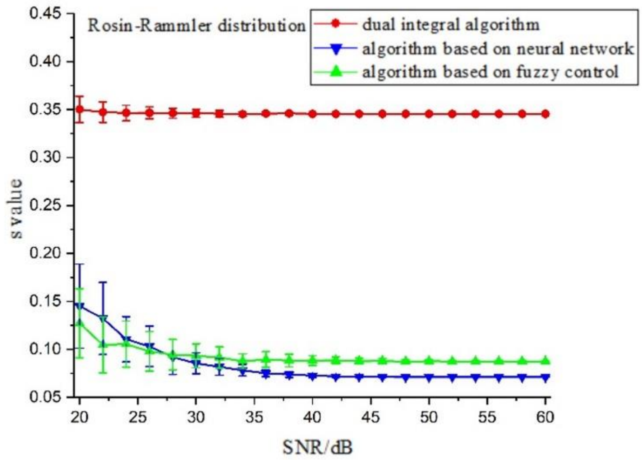

Figure 31 Reconstruction s value of Rosin-Rammler distribution under different noise levels

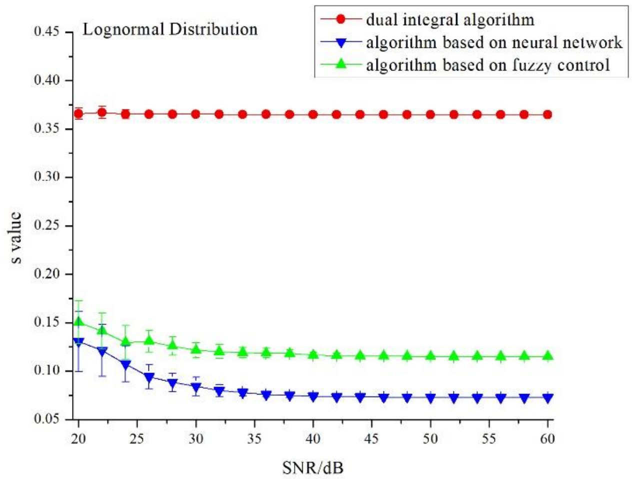

Figure 32 Reconstruction s value of lognormal distribution under different noise levels

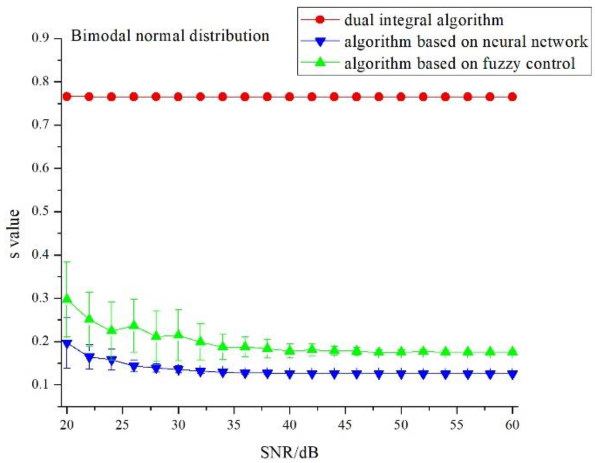

Figure 33 Reconstruction s value of bimodal normal distribution under different noise levels

3.4. Conclusions

In this chapter, the compatibility between the iterative process of the reconstruction algorithm and the feedback function in the closed-loop control principle is pointed out firstly. The method of introducing the closed-loop control principle into the particle size distribution reconstruction process is proposed. The simulations verify the feasibility of the method. Secondly, the principle of adaptive selection of PID controller parameters by neural network model is introduced in detail. The improved integral inversion algorithm based on neural network model is designed and implemented. The superiority of the improved algorithm in narrow particle size distribution reconstruction is verified by simulation. At the same time, the deficiencies of the neural network model applied to the inversion algorithm are analyzed. Finally, in order to further improve the performance of the granular inversion algorithm, an improved integral inversion algorithm based on fuzzy control is proposed. The design process of the fuzzy controller is introduced in detail. The simulation results show that the inversion algorithm based on fuzzy control theory has obvious superiority in narrow-particle particle size reconstruction compared with the traditional dual integral algorithm.

Chapter 4 System structure improvement and experiments

In order to obtain more accurate results of narrow-particle particle size distribution reconstruction, it is necessary to obtain accurate measurement data. Therefore, how to eliminate or reduce the interference introduced in the measurement process is an issue that needs to be studied in depth. The modulation and demodulation technology can effectively filter out the influence of the noise that the signal may introduce during the transmission on the measurement, and improve the accuracy of the measurement signal. This chapter applies the modulation and demodulation principle to improve the anti-noise ability of the measurement signal.

4.1. Structure improvement based on modulation and demodulation principle

Modulation and demodulation technique is widely used in weak signal measurement. The modulation process refers to the synthesis of signals onto a carrier. The demodulation process refers to extracting the effective information of the signal from the synthesized signal. The modulation and demodulation technology can effectively reduce the influence of external interference signals that may be introduced during the propagation process on the measurement results. This subject adopts the principle of multiplication and demodulation in phase sensitive demodulation. The amplitude of the laser signal is sinusoidally modulated by the carrier signal and then input into the measurement system. The measured signals are respectively multiplied by the sine and cosine signals of the same frequency as the carrier signal. After the filtering process, the demodulated light intensity signal can be obtained.

Assuming that the input light intensity signal is *I(t)*, the carrier signal *c(t)* is a sine wave with the frequency of *fc* and the amplitude of *A*, the modulated light intensity signal can be expressed as

$$y(t) = I(t) \cdot \mathrm{c}(t) = I(t) \cdot A\sin(2\pi f_c t) \tag{4.1}$$

The external interference signal that may be introduced during the transmission of the signal is represented by *e(t)*, and the signal received by the photodetector can be expressed as

$$y'(t) = y(t) + e(t) = I(t) \cdot A\sin(2\pi f_c t) + e(t) \tag{4.2}$$

The received signals are multiplied by the cosine and sinusoidal signals of the same frequency as the carrier signal, respectively. The process is:

$$\begin{cases} q(t) = y'(t) \cdot \cos(2\pi f_c t + \phi) = [I(t) \cdot A\sin(2\pi f_c t) + e(t)] \cdot \cos(2\pi f_c t + \phi) \\ p(t) = y'(t) \cdot \sin(2\pi f_c t + \phi) = [I(t) \cdot A\sin(2\pi f_c t) + e(t)] \cdot \sin(2\pi f_c t + \phi) \end{cases} \tag{4.3}$$

Applying the orthogonality of the Fourier transform, the final expression of the signal is obtained:

$$\begin{cases} q(t) = \frac{1}{2} I(t) \cdot A\sin(-\phi) + \frac{1}{2} I(t) \cdot A\sin(4\pi f_c t + \phi) + e(t) \cdot \cos(2\pi f_c t + \phi) \\ p(t) = \frac{1}{2} I(t) \cdot A\cos(-\phi) - \frac{1}{2} I(t) \cdot A\cos(4\pi f_c t + \phi) + e(t) \cdot \sin(2\pi f_c t + \phi) \end{cases} \quad (4.4)$$

It can be seen that the two signals obtained are composed of three components: a low frequency component containing the original measurement signal information, a co-frequency component of the modulation frequency, and a double frequency component. Therefore, the processed signals *q(t) and p(t)* pass through a low-pass filter with a cut off frequency lower than *fc* and the high-frequency components are filtered out. Finally, the resulting signal contains valid information of the measured signal:

$$\begin{cases} q'(t) = \frac{1}{2} I(t) \cdot A\sin(-\varphi) \\ p'(t) = \frac{1}{2} I(t) \cdot A\cos(-\varphi) \end{cases} \quad (4.5)$$

The measured signal amplitude can be effectively restored by $I(t) \propto \sqrt{q^2(t) + p^2(t)}$.

In an actual measurement system, modulation of the intensity of the light is achieved by an electro-optic modulator. Under the action of a strong external electric field, some crystals will produce birefringence or change in original birefringence properties. This phenomenon is called the electro-optic effect of the crystal. The crystal with this effect is called electro-optic crystal [55]. The principle of the electro-optic modulator is shown in Figure 34:

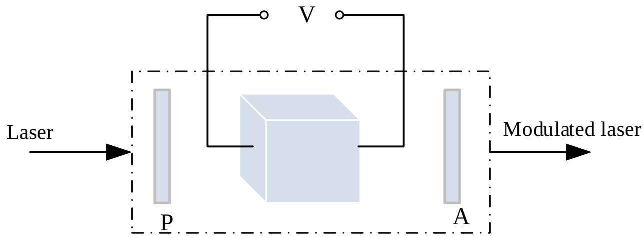

Figure 34 Electro-optic modulator principle

In the figure, V is an externally strengthened electric field, and P and A are two orthogonal polarizers. When an electro-optic crystal is applied with a varying electric field, itself equivalent to a wave plate. The phase delay due to the electro-optic effect changes the polarization state of the crystal, so that the intensity of the light output after passing through the polarizer changes with the voltage, achieving the light intensity modulation. Generally, in order to maintain a linear change between the output light intensity and the external voltage, it is necessary to apply a DC bias at both ends of the crystal so that the two axially polarized lights have an initial phase difference π . This DC bias voltage is called a half wave voltage.

The structure is shown in Figure 35, and the signal received by the detector can be used for reconstruction of the particle size distribution after demodulation.

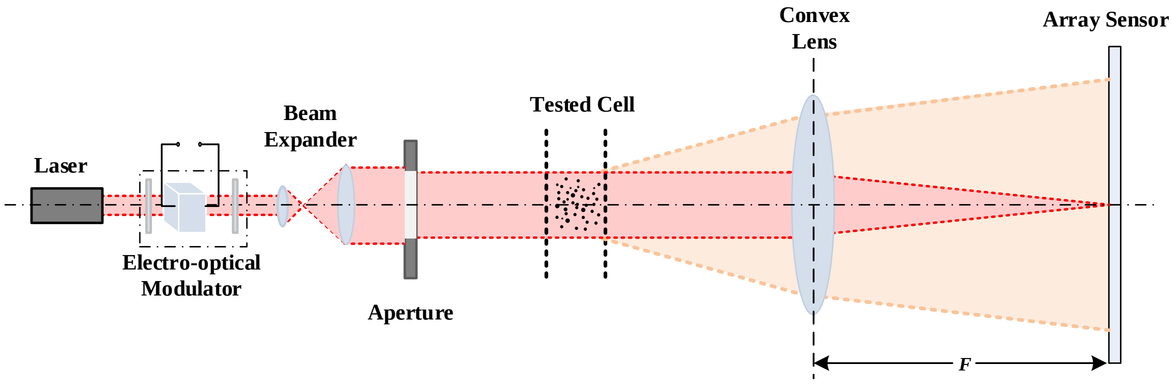

Figure 35 Measurement structure with modulation and demodulation technique

4.2. Latex standard particle suspension experiments

4.2.1. Experimental device

The experimental setup is shown in Figure 36, in order to avoid the error introduced by the detector response inconsistency, the combination of digital micromirror array (DMD), converging lens and single point detector replaced the ring detector array in the traditional measurement system. The monochromatic laser passes through the collimating mirror and the electro-optic modulator. The intensity is modulated into a sine wave. After passes through the beam expander, aperture, measurement area and convex lens, the Light produces diffraction fringes on the DMD which is placed on the focal plane of the receiving lens. And the DMD is sequentially flipped by the upper computer to set the split ring, so that the light energy on the 1/4 ring area is concentrated by the lens and then received by the detector. The received signal is demodulated by a lock-in amplifier to finally obtain a light intensity signal for reconstruction. The following is a brief introduction to each part of the experimental setup:

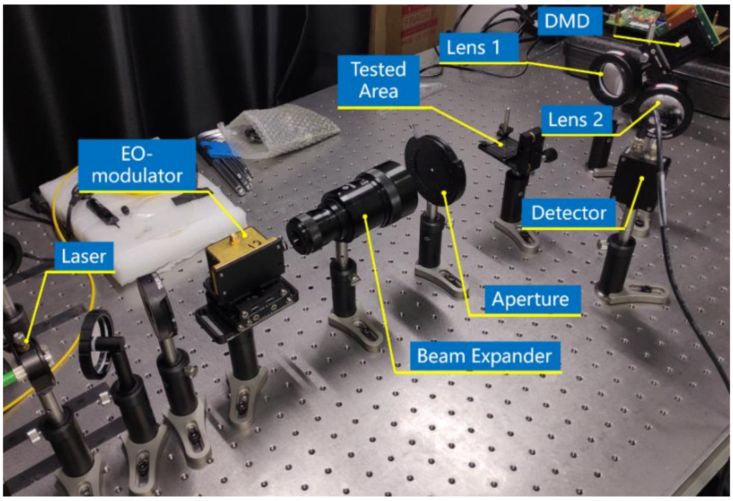

Figure 36 Particle size measuring device based on modulation and demodulation principle

1）Laser source：

The semiconductor laser has the advantages of small size and low cost. Therefore, this experiment uses a fiber-optic output semiconductor laser source with a wavelength of 650 nm. The divergence angle is 0.6 mrad and the maximum output power is 30 mW. The intensity of the diffracted light can be guaranteed.

2）Modulation section

The spatial light modulator used should be suitable for the actual measurement band. The actual measurement uses the EO-AM series of electro-optical amplitude modulators produced by Thorlabs to achieve a light modulation for spatial light. The actual image is shown in Figure 37:

Figure 37　Electro-optic modulator

The applicable wavelength range of the electro-optic modulator is 600 nm-900 nm. In the experiment, the applied half-wave voltage can be approximated by the Eq.(4.6):

$$V_{\pi} = 0.361\lambda - 23.844 \tag{4.6}$$

3）Photodetection section

The photodetection part consists of a DMD, a converging lens and a single point detector.

（1）DMD

The experiment uses an ultra-high speed DMD spatial light modulator produced by Vialux, Germany. The object is shown in Figure 38.

Figure 38 DMD

The photosensitive area is an array of micro-mirrors with a block size of 13.68 μm×13.68 μm. Each micro-mirror has two stable states: 1 indicates a deflection of +12° with a diagonal axis, and 0 indicates a deflection of -12°. In the experiment, when the upper computer controls the micromirror to flip, the optical signal is received by the detector when the state is set to 1.

During the experiment, it is necessary to preset the micromirror annular array for each flip of the DMD. To maximize the use of the space, the optical path should be adjusted so that the laser passes through the lens and converges to the corner of the DMD. Set the focus to the center of the circle, set 35 times to turn the ring, each time to 1/4 ring, as shown in Figure 39. The left side is an odd ring, and the right side is an even ring. In the figure, white represents a 1 area, and black represents a 0 area. In order to prevent the Airy disk at the center of the diffracted spot, the innermost radius of the DMD flip is slightly larger than the Airy disk radius, which is equivalent to the small hole left in the center of the conventional ring detector array. The wavelength of the light source is 650 nm, the inner diameter of the innermost ring of the DMD split ring deflection is *Rin*=396.7 μm, and the outermost diameter of the outer ring is *Rout*=8892.0 μm.

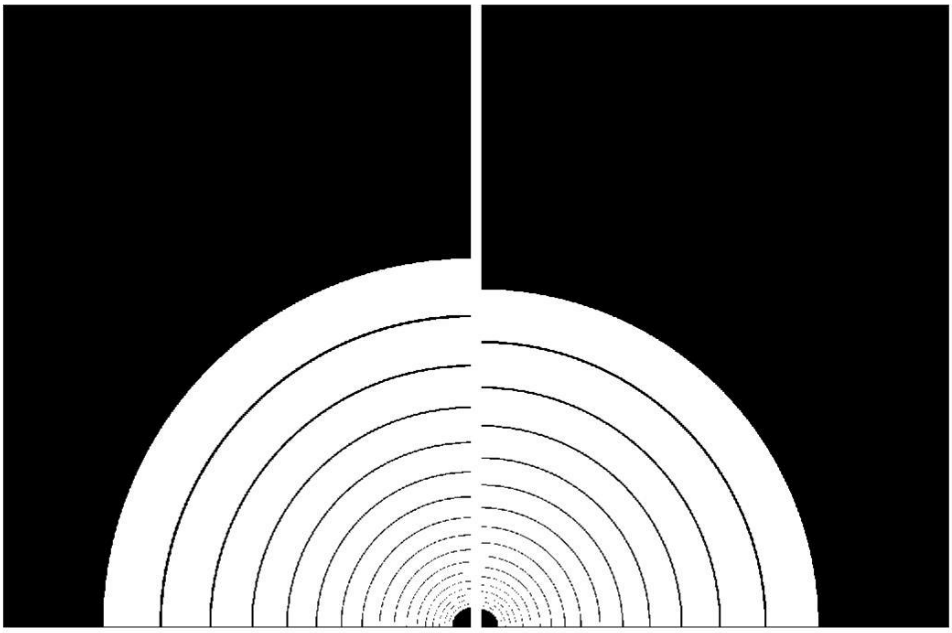

Figure 39 DMD flip rings (35 groups)

（2）Receiving lens

The focal length of the receiving lens determines the lower limit of the detectable particle. Under the condition that the particle measuring range is satisfied, the lens with smaller focal length, the larger the detectable diffraction angle. In this experiment, the focal length of the receiving lens is chosen to be 15 cm. Therefore, the minimum detectable and maximum diffraction angles are 0.15° and 3.39° respectively, and the detectable lower limit of the particles is 4.74 μm.

（3）Single point detector

The single-point detector receives the real image after the diffraction fringe on the DMD passes through the condenser lens. Therefore, it is necessary to select the detector with the largest possible photosensitive surface. In this experiment, Thorlabs PDA100A-EC photodetector is selected, and the photosensitive surface is $10\times10\ \mathrm{mm}^2$. The detectable wavelength range is from 340 nm to 1100 nm.

4）Fraunhofer transform optical structure

A wider application of forward Fourier transform optical structure is adopted in this experiment, and the optical path part structure is:

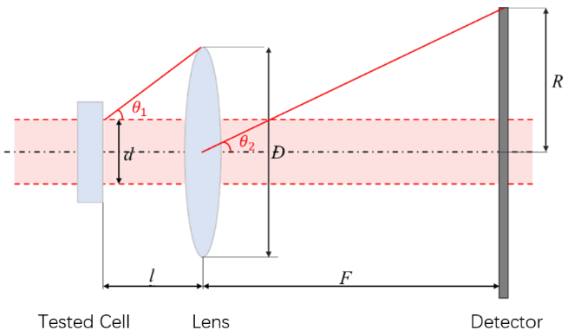

Figure 40　Forward Fourier transform optical structure

In Figure 40, d is the parallel laser beam width, D is the Fourier lens diameter, R is the maximum detection radius, l is the horizontal distance between the sample cell and the Fourier lens, F is the Fourier lens focal length.

As can be seen from Figure 40, the maximum diffraction angle at which the lens can converge is θ_1:

$$\theta_1 = \frac{D-d}{2l} \tag{4.7}$$

The maximum diffraction angle detectable by the detection area is θ_2:

$$\theta_2 = \frac{R}{F} \tag{4.8}$$

To ensure that the detection area is maximized, θ_1 and θ_2 should be satisfied $\theta_1 \geq \theta_2$, Therefore, it can be concluded that the relationship between the parameters is:

$$l \leq \frac{F(D-d)}{2R} \tag{4.9}$$

In the experiment, the focal length of the lens is 15 cm, the diameter is 46.04 mm, and the outermost ring radius of the DMD is 8892.0 μm. The experimental sample cell is a cuvette with an inner side length of 9.96 mm. During the experiment, the laser spot diameter should be controlled to be smaller than the inner side of the cuvette. The distance between the cuvette and the Fourier can be calculated from Eq.(4.9) should not exceed 304.32 mm.

During the experiment, the laser source, the beam expander, the aperture and the receiving lens should be adjusted to be strictly coaxial, the DMD is placed at the focal plane of the receiving lens, and the position of the DMD is adjusted so that the parallel light is concentrated by the lens on a micromirror unit of the DMD.

5）Test sample

In this experiment, polystyrene standard particles are used as the measured particle group. For the single peak distribution, four standard particle suspensions were used as experimental samples, which named class A, B, C, and D with center particle diameters of 21.3 μm、25.0 μm、30.0 μm、35.0 μm respectively. For bimodal distribution, particle suspensions with different particle sizes of 21.3 μm (standard particle A) and 35.0 μm (standard particle D) were used. The liquid was used as an experimental sample to be tested, and the ratio of the two particles was 1/3, 1/2, 1/1, 2/1, 2/3 (in terms of the number of drops). According to the standard particle identification manual, the theoretical particle size distribution of the four unimodal standard particles is shown in Figure 41 and Table 5 shows the corresponding particle size distribution parameters.

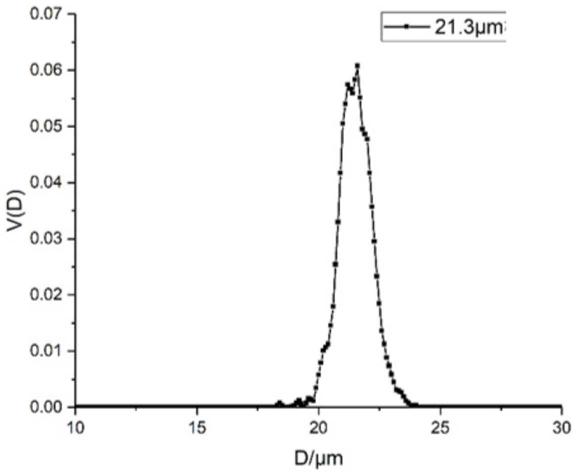

(a) particle size distribution curve of class A

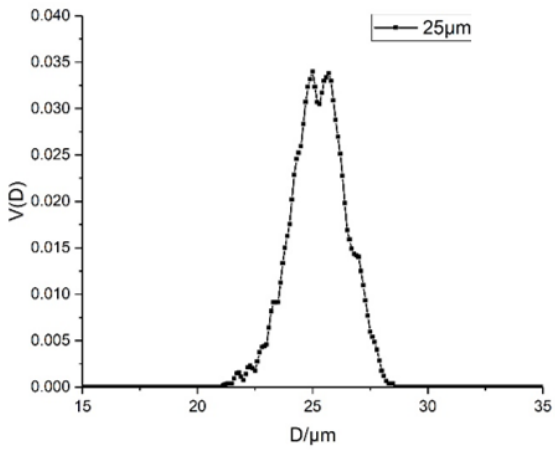

(b) particle size distribution curve of class B

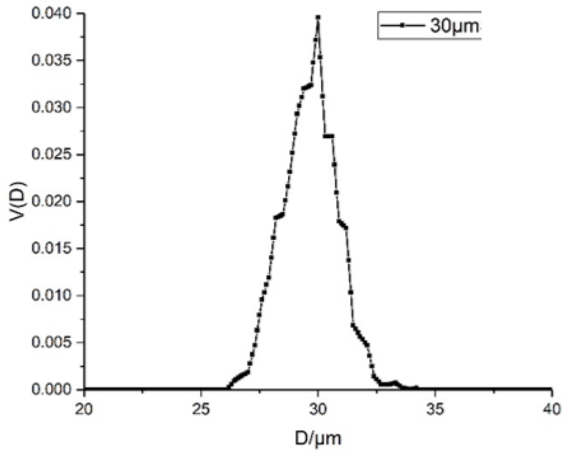

(c) particle size distribution curve of class C

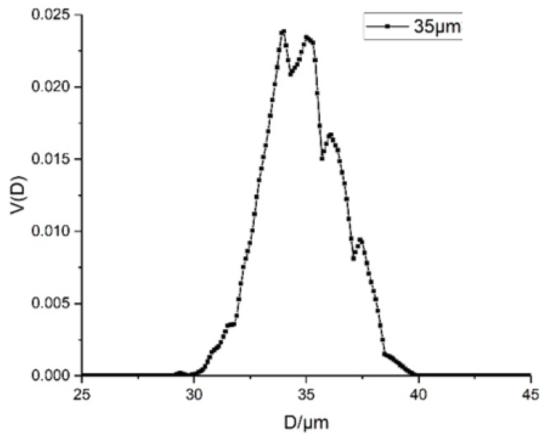

(d) particle size distribution curve of class D

Figure 41 Four standard particle distributions

Table 5 Four standard particle corresponding distribution parameters

Distribution parameter	Standard particle type			
	A	B	C	D
Center particle size (μm)	21.3	25.0	30.0	35.0
Distribution width (μm)	4.0	6.6	6.0	8.4

In order to ensure the experimental results, the following issues need to be considered:

1）The effect of interface effects on measurements

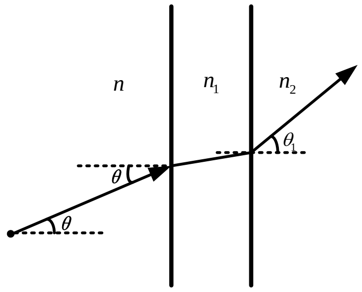

Figure 42　Interface effect

As shown in Figure 42, since the medium outside the cuvette is air and the medium in the cuvette is water, different refractive indices of different media will introduce systematic errors. Assuming that the refractive index of the medium inside is n_1, the refractive index of the cuvette is n_2 and the refractive index of the medium outside is n_3, the relationship between the actual diffraction angle θ and the diffraction angle received at the detection position θ' is satisfied:

$$\theta = \arcsin(\frac{n_3}{n_1}\sin\theta') \approx \frac{n_3}{n_1}\theta' \tag{4.10}$$

In the experiment, n_1=1.33， n_3=1, so that the diffraction angle can be corrected by $\theta = \theta'/1.33$.

2）Preparation of experimental samples

The standard particles used in the experiment were dispensed in the form of an aqueous suspension, which was sonicated for 5 minutes before use, so that the standard particle suspension was uniformly mixed. Then, the test standard particles were dropped into a cuvette containing distilled water. Due to the dynamic change of the suspension, the sedimentation velocity of the suspension needs to be considered in the measurement. Considering that the particles measured in the experiment are small particles with a diameter of micrometers, the largest diameter particles are particles has the fastest settlement speed, which with a center particle diameter of 35.0 μm and its complete settling time is about 3 min. In order to avoid the influence of settlement, the measurement time should be less than 1 min.

In this subject, the carrier signal frequency used for modulation is 500 kHz, and the DMD flip frequency is 1 kHz. The time required to measure a set of data is less than 0.05 s, and the measurement time is much smaller than the particle settling time. Therefore, the particle sedimentation effect can be ignored.

4.2.2. Analysis and discussion of experimental results

1）Measurement signal noise immunity verification

In order to verify that the new particle size measurement system has certain anti-noise ability, the experiments under the two conditions of dark room and incandescent lamp as interference light source have been done. Each group repeated measurements 50 times. The measured diffraction intensity distribution is shown in Figure 43 to Figure 46 and the signal-to-noise ratios of the data measured by different measurement methods for different distributions of particle groups are listed in Table 6 to Table 9, for convenience comparison, the measured light intensity is normalized.

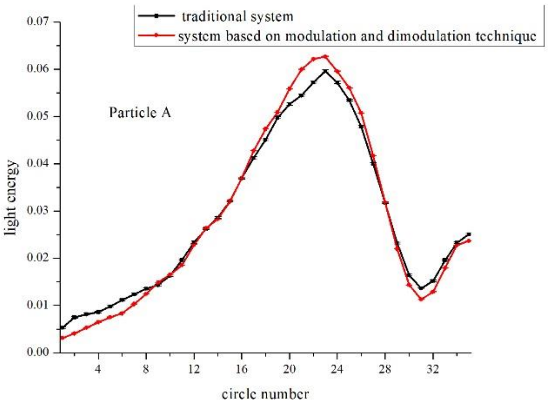

(a) intensity distribution of Class A

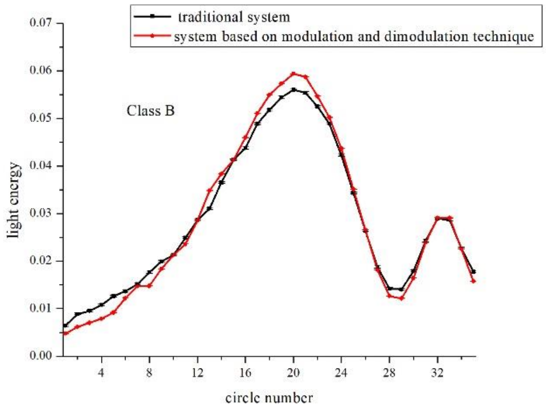

(b) intensity distribution of Class B

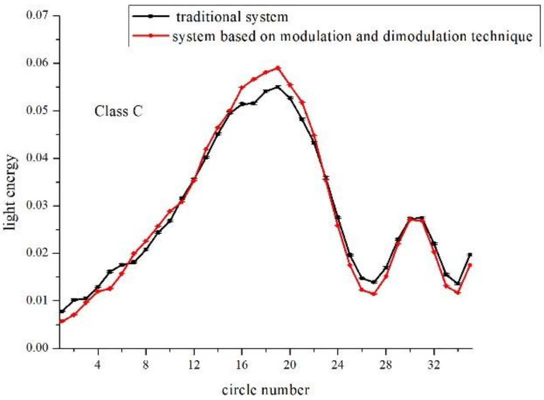

(c) intensity distribution of Class C

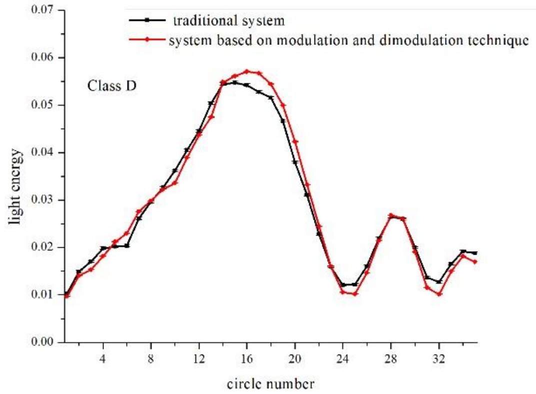

(d) intensity distribution of Class D

Figure 43 Light intensity distribution of unimodal particles under dark room condition

Table 6 Signal-to-noise ratio (dB) of unimodal particles under darkroom condition

Measurement methods	Unimodal distribution standard particle class			
	A	B	C	D
Traditional measurement method	41	41	42	41
Modulation and demodulation method	58	58	58	57

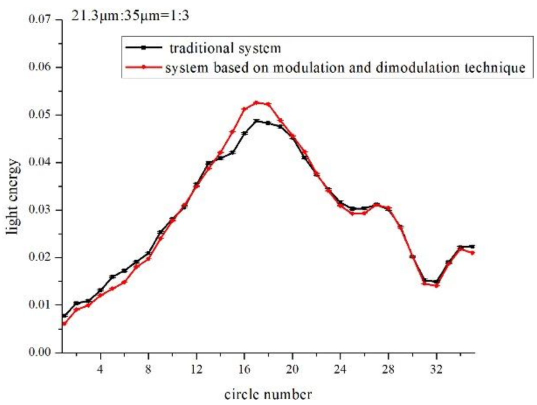

(a) intensity distribution(Class A:D=1:3)

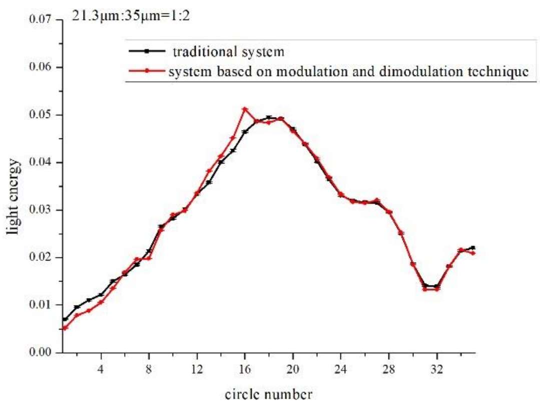

(b) intensity distribution(Class A:D=1:2)

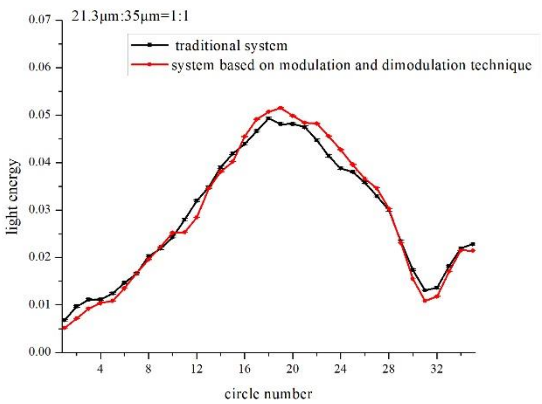

(c) intensity distribution(Class A:D=1:1)

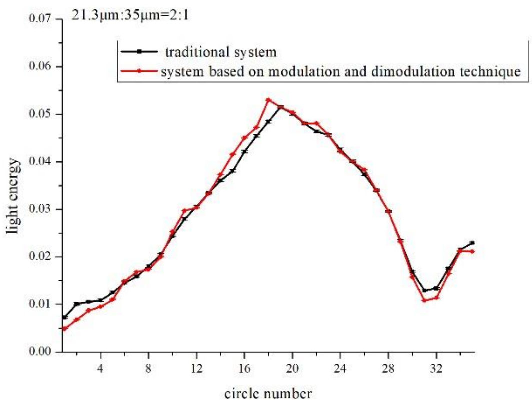

(d) intensity distribution(Class A:D=2:1)

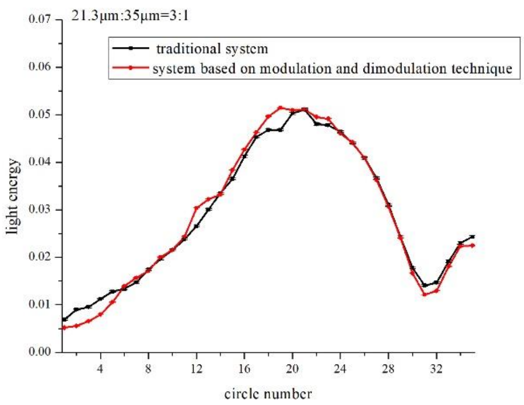

(e) intensity distribution(Class A:D=3:1)

Figure 44 Light intensity distribution of bimodal particles under dark room condition

Table 7 Signal-to-noise ratio (dB) of bimodal particles under darkroom condition

Measurement methods	Preparation ratio of standard particle suspension (A:D)				
	1:3	1:2	1:1	2:1	3:1
Traditional measurement method	42	42	42	40	41
Modulation and demodulation method	57	58	57	56	57

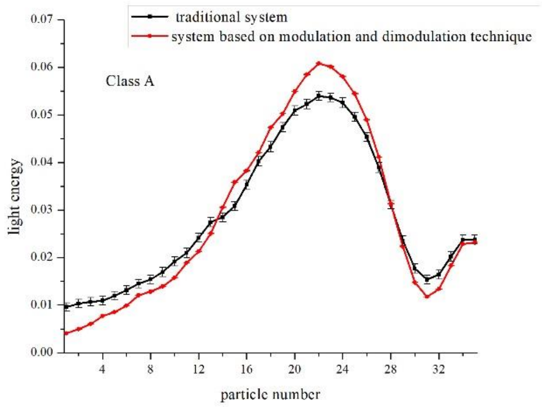

(a) intensity distribution of Class A

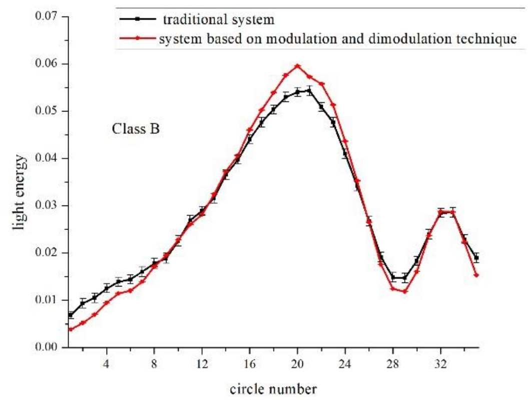

(b) intensity distribution of Class B

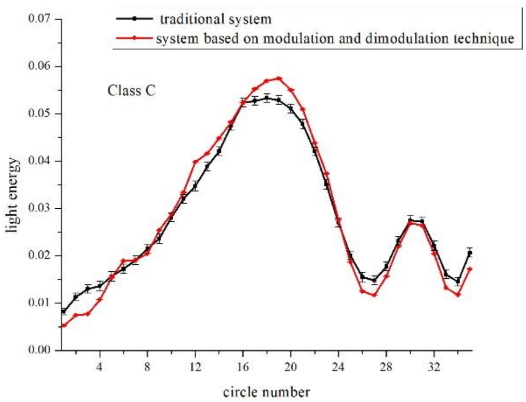

(c) intensity distribution of Class C

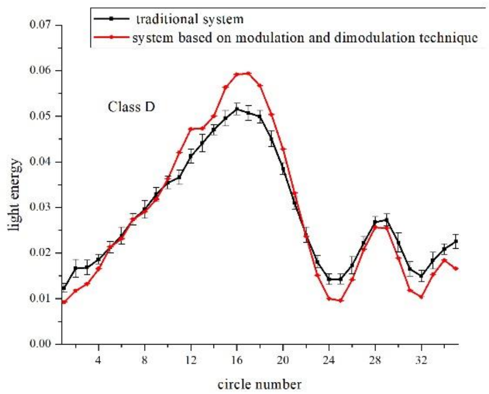

(d) intensity distribution of Class D

Figure 45 Light intensity distribution of unimodal particles under interference condition

Table 8 Signal-to-noise ratio (dB) of unimodal particles under interference condition

Measurement methods	Unimodal distribution standard particle class			
	A	B	C	D
Traditional measurement method	28	28	29	25
Modulation and demodulation method	58	57	58	56

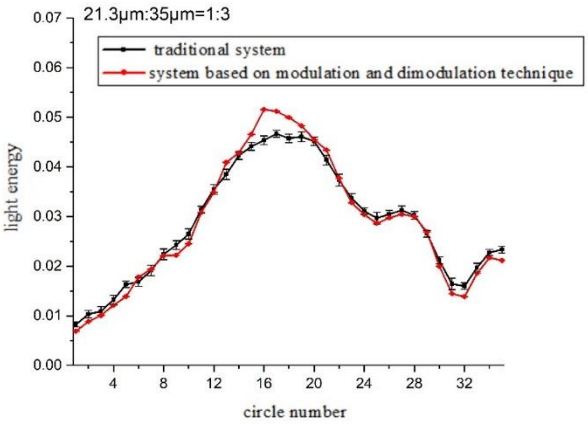

(a) intensity distribution(Class A:D=1:3)

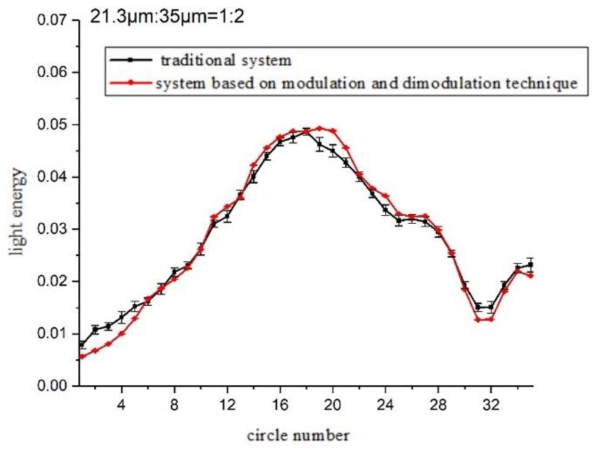

(b) intensity distribution(Class A:D=1:2)

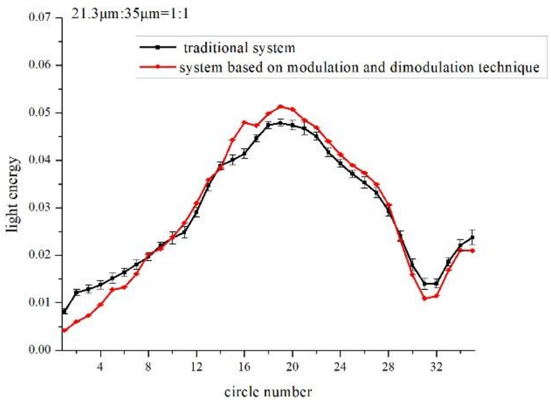

(c) intensity distribution(Class A:D=1:1)

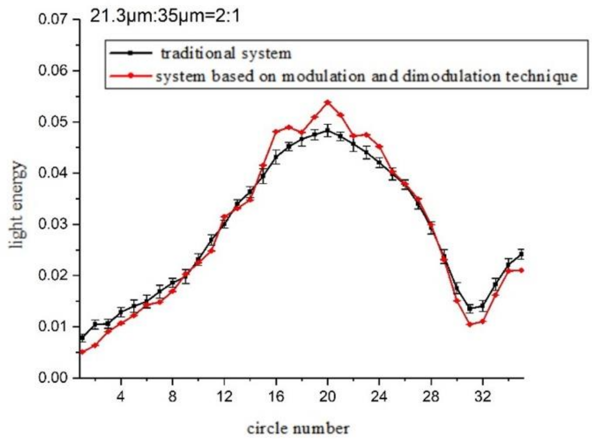

(d) intensity distribution(Class A:D=2:1)

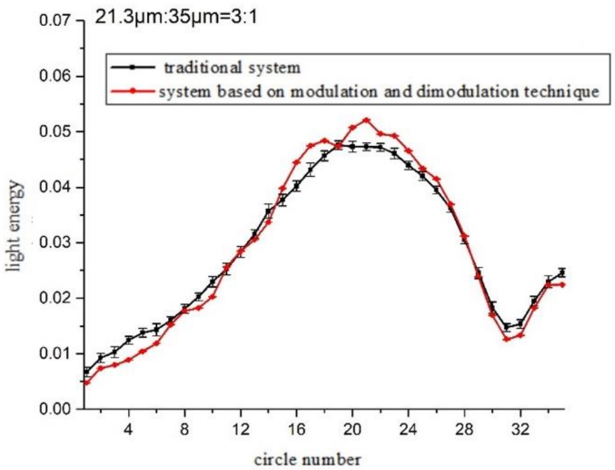

(e) intensity distribution(Class A:D=3:1)

Figure 46 Light intensity distribution of bimodal particles under interference condition

Table 9 Signal-to-noise ratio (dB) of bimodal particles under interference condition

Measurement methods	Preparation ratio of AD standard particle suspension				
	1:3	1:2	1:1	2:1	3:1
Traditional measurement method	30	29	28	27	29
Modulation and demodulation method	57	56	56	56	57

The measurement results show that for the mixed suspensions of four single-peak standard particles and two kinds of particles with different ratios, after applying the modulation and demodulation principle, the error bars of the measurement signals are significantly smaller than those of traditional system, both under the darkroom condition and incandescent lamp interference condition. The measurement results show that the improved method has smaller fluctuations in measurement data and relatively stable measurement values. In darkroom condition, the signal-to-noise ratio of the measurement signal is increased from about 40 dB to about 56 dB. With the interference of incandescent lamps, the signal-to-noise ratio of the measurement signal is insufficient increased from 30 dB to more than 55 dB, which indicates that the repeatability of the measured signal is better after applying the modulation and demodulation technique.

Therefore, the system applying he modulation and demodulation technique has superior anti-noise ability compared with the traditional measurement system. It can effectively suppress the background light intensity interference, and the signal repeatability is obviously improved.

2）Reconstruction algorithm accuracy verification

Considering the practical application prospects, in this paper, the reconstruction results of the integral algorithm based on the fuzzy control principle are mainly verified. Using the data measured by the above-mentioned modulation and demodulation method under the interference of incandescent lamps, the particle size distributions of the four unimodal distribution standard particles and the bimodal distribution particle groups generated by different ratios are reconstructed respectively. The reconstruction results are shown in Figure 47 to Figure 48. As shown, the reconstruction distribution mean and error bars of 50 measurements are plotted. Table 10 and Table 11 show the reconstruction accuracy of the improved integral inversion algorithm using the dual integral inversion algorithm and the algorithm based on fuzzy theory respectively (represented by s value).

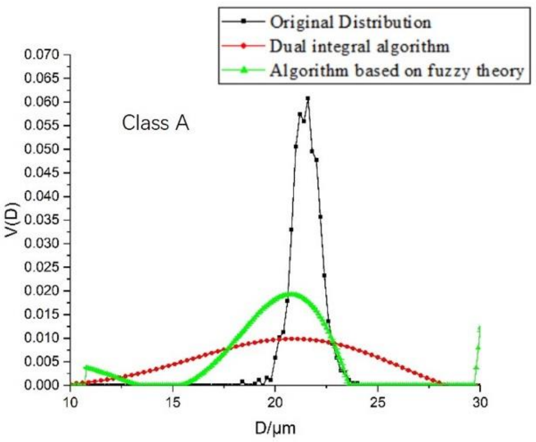

(a) reconstruction results of Class A

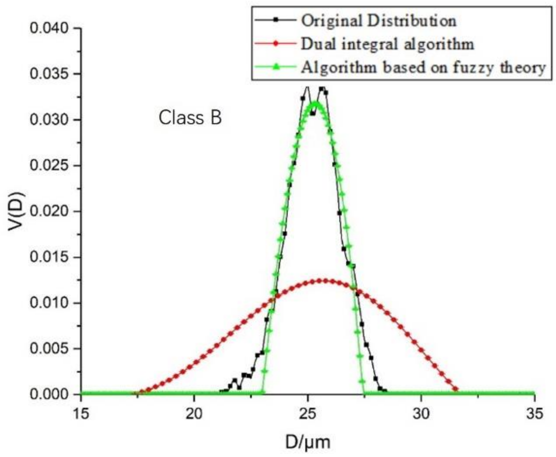

(b) reconstruction results of Class B

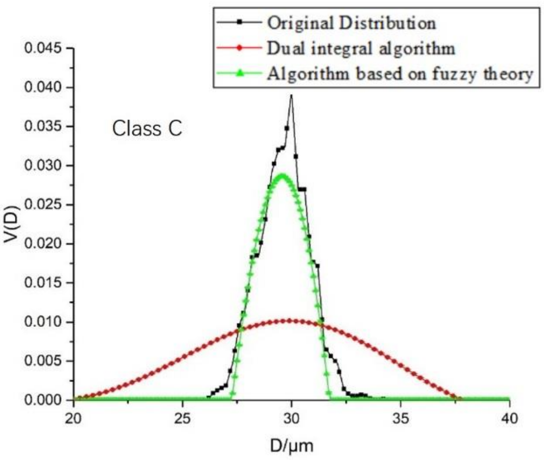

(c) reconstruction results of Class C

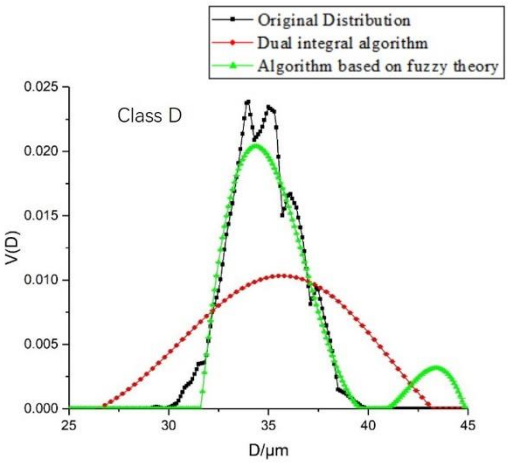

(d) reconstruction results of Class D

Figure 47 Unimodal distribution particle size distribution reconstruction result

Table 10 Unimodal distribution particle reconstruction accuracy (s value)

Inversion algorithm	Unimodal distribution standard particle class			
	A	B	C	D
Dual integral algorithm	0.85	0.64	0.71	0.57
Algorithm based on fuzzy theory	0.72	0.15	0.19	0.17

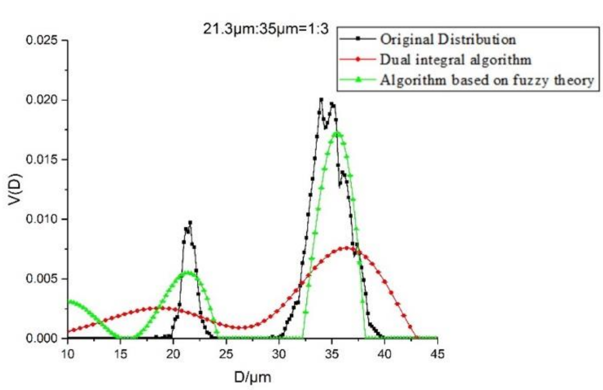

(a) reconstruction results (ClassA:D=1:3)

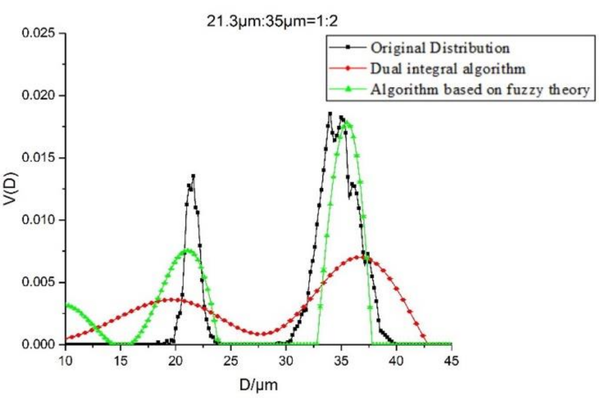

(b) reconstruction results (ClassA:D=1:2)

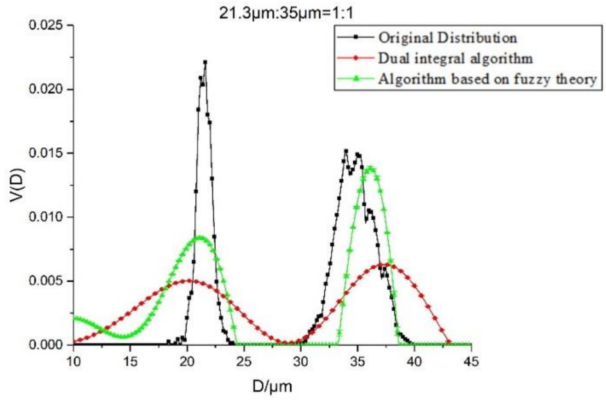

(c) reconstruction results (ClassA:D=1:1)

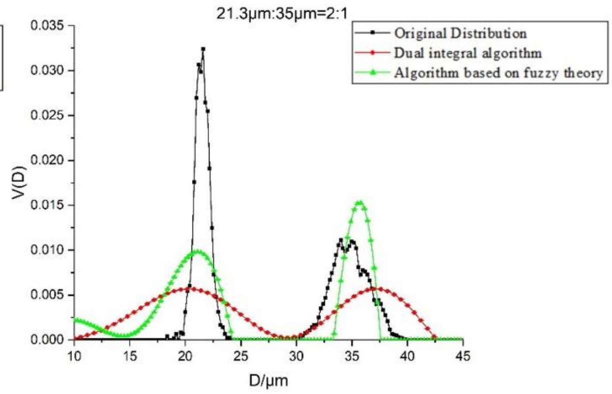

(d) reconstruction results (ClassA:D=2:1)

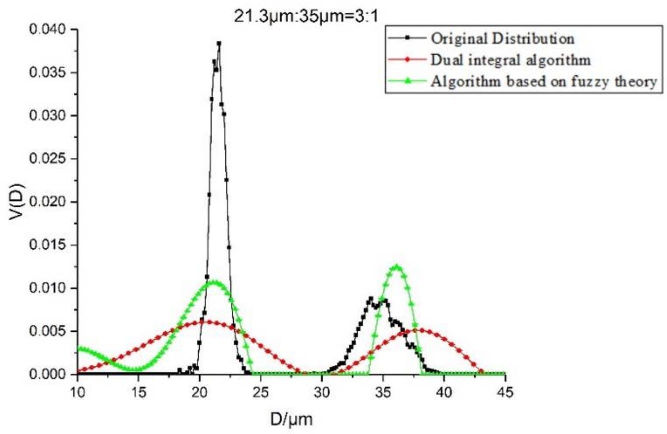

(e) reconstruction results (ClassA:D=3:1)

Figure 48 Bimodal distribution particle size distribution reconstruction result

Table 11 Bimodal distribution particle reconstruction accuracy (s value)

Inversion algorithm	Preparation ratio of standard particle suspension (A:D)				
	1:3	1:2	1:1	2:1	3:1
Dual integral algorithm	0.66	0.69	0.77	0.81	0.85
Algorithm based on fuzzy theory	0.39	0.50	0.64	0.70	0.73

It can be seen from the reconstruction results that for the Class A standard particles with a center particle size of 21.3 μm, the s value of the proposed algorithm is slightly smaller than that of the dual integral inversion algorithm, but the reconstruction results are not significantly improved. For the Class B and C standard particles with a center particle size of 25.0 μm and 30.0 μm respectively, the proposed algorithm can accurately reconstruct the particle size distribution. Compared with the traditional dual integral inversion algorithm, the s values are reduced from 0.64 and 0.71 to 0.15 and 0.19 respectively. For Class D standard particles with a center particle size of 35.0 μm, the proposed algorithm can accurately reconstruct the main peak distribution, and the s value is reduced from 0.57 to 0.17, but a fake peak appears. For the bimodal distribution particles, the s values are slightly reduced. The double peak can be distinguished and the problem of large particle size center shift is slightly improved. But the reconstruction results for small particle cannot match the original distribution well and there are fake peaks.

Since the ratio cannot be strictly guaranteed in the experiment and the agglomeration may occur after the two particles are mixed, the theoretical value of the bimodal particles can only be seen as a reference value, and the reconstruction result cannot be accurately evaluated. In order to evaluate the reconstruction effect of the algorithm on the bimodal particles, the ratio of the two kinds of particles in the distribution function reconstructed by the two algorithms is calculated separately (the area enclosed by the horizontal axis and the reconstructions). The correlation between the quantitative ratio calculated by the reconstruction results of the two reconstruction algorithms and the ratio change is shown in Figure 49. Both the dual integral algorithm and the improved algorithm can accurately reflect the changes of different particle ratios.

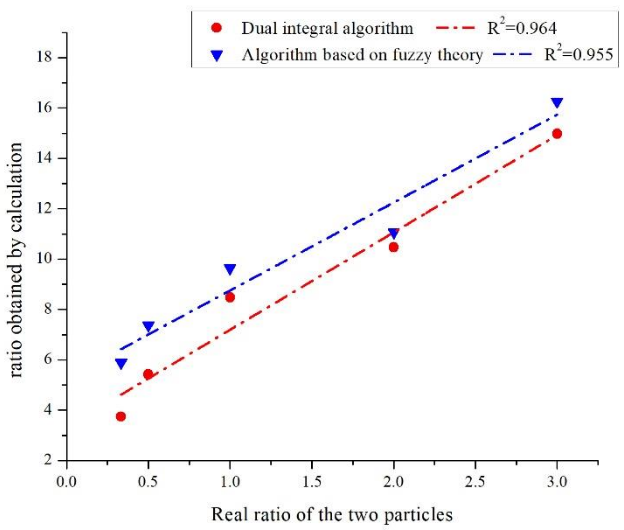

Figure 49 The ratio relationship

In summary, although the improved reconstruction algorithm may produce fake peaks, the overall reconstruction accuracy is improved.

3）Discussion on calibration of experimental data

It can be seen from the previous analysis that when using the integral reconstruction algorithm based on fuzzy control theory to reconstruct the particle group with multi-peak distribution, the requirement accuracy of the measurement data is higher. Therefore, for the case of mixing two standard particles, the experimental data can be calibrated to improves the accuracy of the measured data.

Use the measurement data of four unimodal standard particles to calibrate the bimodal particle measurement data. Taking into account the DMD array of 1024×768 micro-mirrors with a size of 13.68 μm×13.68 μm, when the upper computer controls its flipping, since the border between each micromirror does not flip with the micromirror, the reflected light of the bezel will introduce a stable light intensity error, and the reflection process of the micromirror will bring a certain loss of light energy, which can be approximated as a proportional error.

Based on the above analysis, the fitting curve is set to $y = kx + b$, in which *y* represents the corrected diffracted light signal and *x* represents the measured diffracted optical signal. The partial fit results are shown in Figure 50:

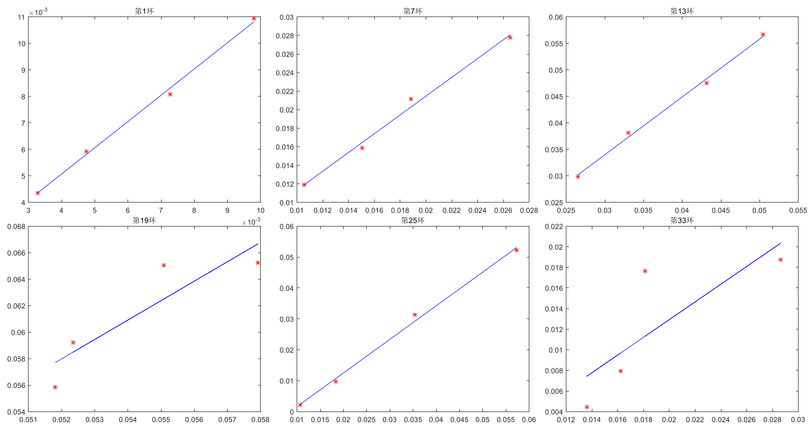

Figure 50 Fitting correction curves (partial)

The bimodal particle group distribution is corrected by the fitted calibration curve. To verify the validity of the calibration, the corrected measurement signal and the original measurement signal are compared, and the relative error of the theoretical light energy is used to evaluate the data accuracy. The error is defined as

$$e = \sqrt{\frac{\sum_{i=1}^{n}(I_i - I_{ref,i})^2}{\sum_{i=1}^{n} I_{ref,i}^2}} \tag{4.11}$$

where I_{ref} is the theoretical light energy distribution, *n* is the total number of the circle. The smaller the relative error, the more accurate the data is. The results of the five sets of experimental data are shown in Figure 51. Table 12 shows the accuracy of the data before and after the correction (indicated by the relative error e):

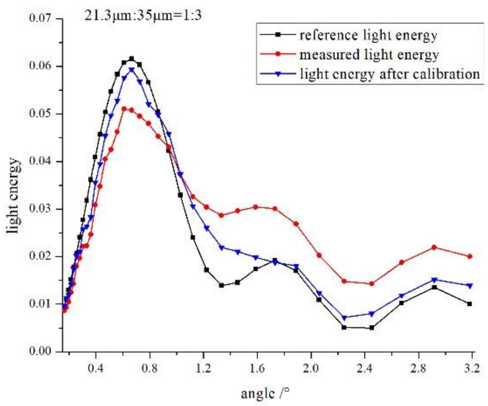

(a) intensity calibration result (Class A:D=1:3)

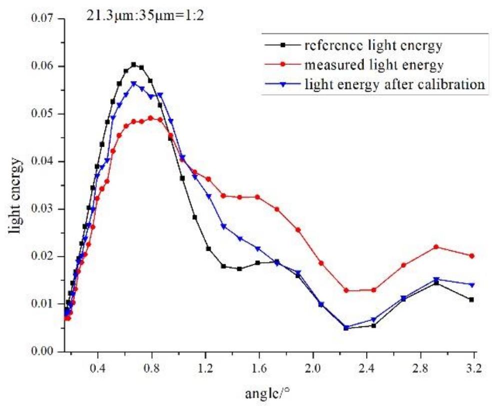

(b) intensity calibration result (Class A:D=1:2)

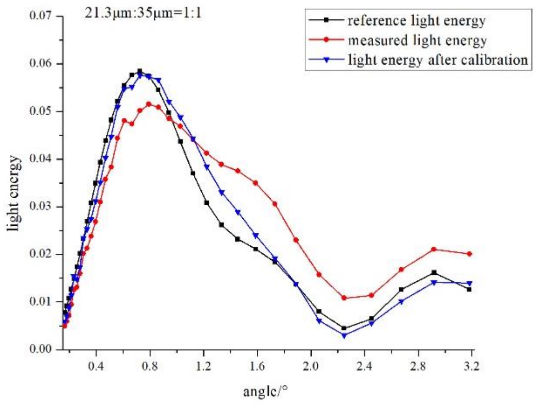

(c) intensity calibration result (Class A:D=1:1)

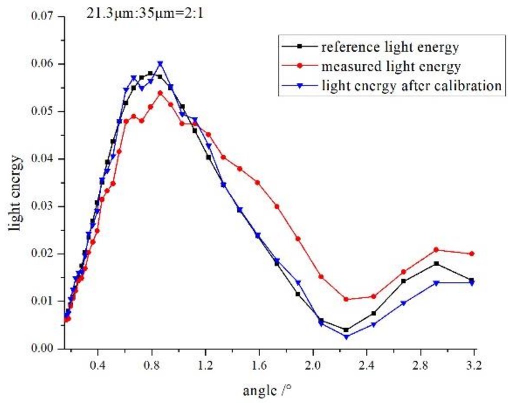

(d) intensity calibration result (Class A:D=2:1)

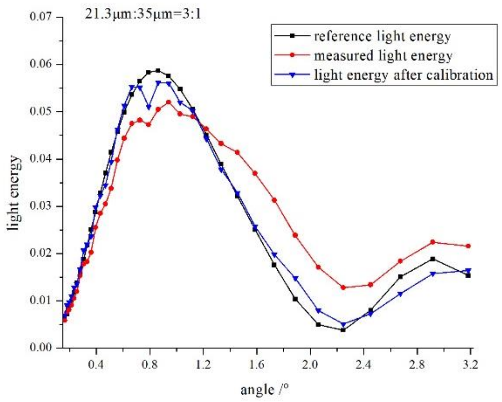

(e) intensity calibration result (Class A:D=3:1)

Figure 51　calibration results

Table 12　Data accuracy before and after calibration (relative error e)

Data category	Preparation ratio of AD standard particle suspension				
	1:3	1:2	1:1	2:1	3:1
Measurement data	0.27	0.27	0.23	0.18	0.20
Data after calibration	0.12	0.13	0.10	0.06	0.06

It can be seen from the correction results that calibrating the measured values of bimodal particles with unimodal particle measurements can effectively improve the accuracy of the measured signal, and the relative error drops into 15%.

The reconstruction results by algorithm based on fuzzy theory are shown in Figure 52:

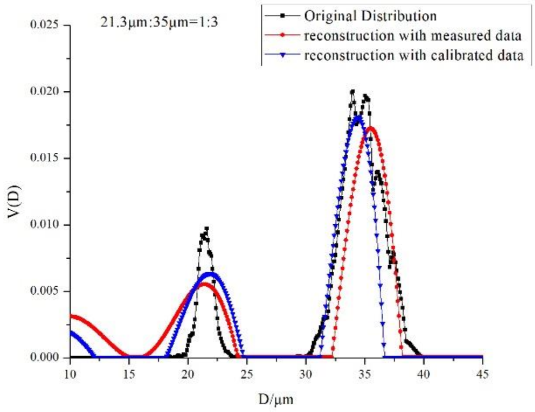

(a) reconstruction results (Class A:D=1:3)

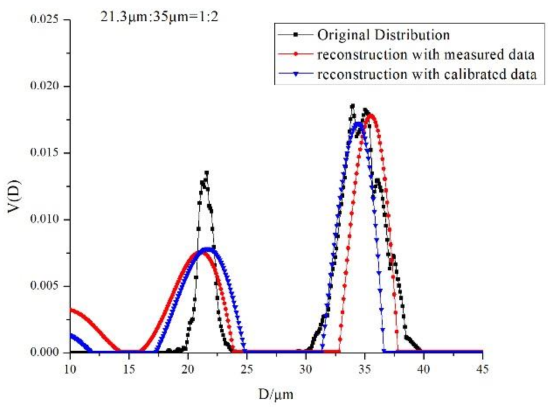

(b) reconstruction results (Class A:D=1:2)

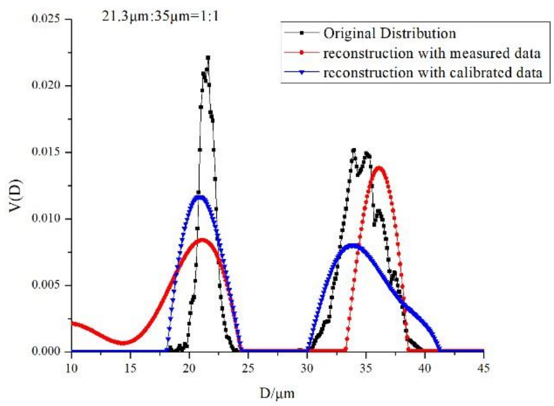

(c) reconstruction results (Class A:D=1:1)

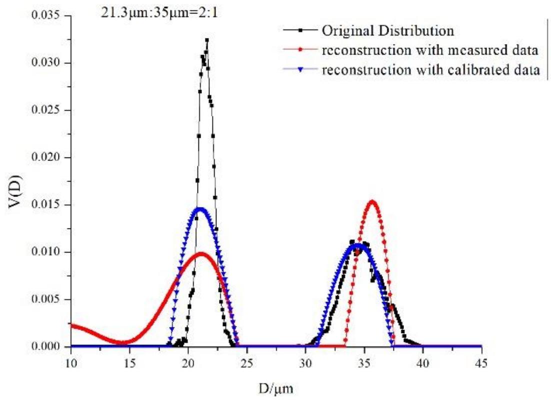

(d) reconstruction results (Class A:D=2:1)

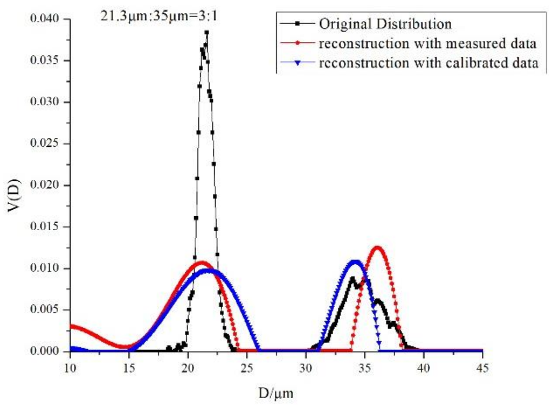

(e) reconstruction results (Class A:D=3:1)

Figure 52 Reconstructions before and after calibration

From the reconstruction results, the corrected data can solve the problem of the center particle size shifting of 35.0 μm particle, and effectively suppress the fake peaks at small particle size. The experimental device designed in this subject can only measure the range of the scattering angle less than 3° in the forward direction, so the reconstruction accuracy at the small particle size is difficult to improve. For the 35.0 μm particle fraction with larger center particle size, the particle size distribution reconstructed with the corrected data is closer to the theoretical distribution than the pre-correction and the reconstruction accuracy is higher. In general, the calibration method can improve the accuracy of the measurement data and also have a positive impact on the reconstruction results.

4.3. Conclusions

This chapter firstly based on the purpose of improving the noise immunity of the measurement system, designed the diffraction signal acquisition method based on the modulation and demodulation principle, and briefly introduced the various parts of the measurement system. Then, using different distributions of polystyrene standard particle suspension as the object to be tested, the experimental results show that the improved method has excellent anti-noise ability compared with the traditional system. Under the condition of incandescent lamp interference, the signal-to-noise ratio of the measurement signal is increased by about 30 dB. At the same time, the reconstruction result using experiment data further proves the reliability of the proposed algorithm based on fuzzy theory. The algorithm effectively improves the accuracy of particle size reconstruction for narrow distribution particles. Finally, a calibration method for measurement data is proposed to effectively correct the systematic error caused by the micromirror array structure of DMD.

Chapter 5 Optical principles of self-mixing interferometry

5.1. Introduction of self-mixing interferometry

Laser interferometry is a well-established technique, because of its advantages of non-contact, high accuracy and sensitivity, it is widely used in the industrial and laboratory environments. However, in the actual application process, the traditional laser interferometry technology has many defects, such as complex system, large size, high cost. These problems also restrict the wide application of the measurement technology. Therefore, designing a simple, stable, compact and high-precision interference system has become the development trend of laser interference technology. Over the last few years Self-mixing Interferometry has taken hold as convenient alternative to other well-established optical measurement techniques. It abandons the shortcomings of previous interferometric techniques and has received increasing attention in the field of high-precision measurement.

The basic principle of self-mixing interferometry is: light is emitted from a laser, is transmitted to an external target from which it is partially reflected, and transmitted back to the laser where a portion of it re-enters the laser cavity; there the reinjected light interacts (mixes) with the resonant modes of the laser. Due to the self-coherent nature of laser feedback interferometers, they are inherently highly sensitive, suppressing most radiation entering the laser cavity that is not their own[56].

Compared with other conventional interference systems, the self-mixing interference (SMI) system has the following advantages[57].

(1) Requires a small number of optical components, requires no external light source, and is simple and compact;

(2) Information is carried by the laser beam and it can be picked up everywhere (also at the remote target location);

(3) Successful operation on rough diffusive surfaces can be achieved;

(4) The SMI system is highly sensitive. Under certain conditions, the sub-nanometer detection sensitivity is better than 280d B;

(5) The SMI system does not depend on the type of laser.

5.2. Self-mixing interference model

There are two equivalent models for the analysis of self-mixing interference: the three-mirror model and the Lang-Kobayashi model.

The Figure 53 shows a three-mirror model. It can be seen from the figure that the laser “internal” cavity is composed of two mirrors named M1 and M2, with length L_D and refractive index n_c. The “external” cavity is composed of mirror M2 and target M3, with length L_E. When the beam output by the laser is irradiated to the target M3, reflection or scattering is formed, and part of the reflected light is reflected back into the laser cavity, and interferes with the cavity light on the M2 of the laser cavity. The length of the outer cavity determines the phase shift. When the artificial outer cavity is artificially adjusted to be the same or integral multiple of the effective optical length of the laser cavity, the laser output power is the largest. This is the physical process of analyzing the self-mixing interference by the three-mirror model.

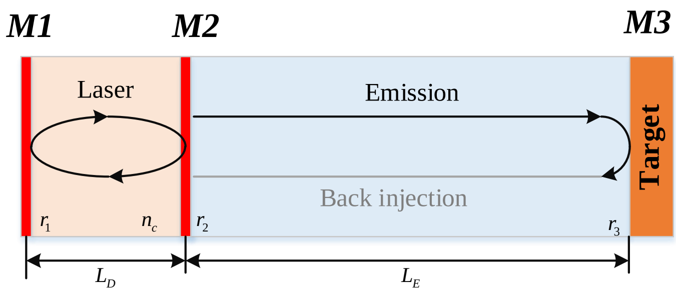

Figure 53 Three-Mirror model of Self-mixing interference

The essence of the Lang-Kobayash model is using the steady-state solution of the rate equation to obtain the optical frequency and intensity of the light emitted by the laser. Under the action of the light field, the atomic excitation transitions, which causes the atomic population density at each working level to change with time, and the total number of photons or photon density in the excitation field also changes with time. In this processing, the Lang-Kobayash model are derived.

In a self-mixing interference system, the external reflector has a small range of displacement changes based on the initial cavity length, and the intensity variation can be detected by a photodetector (PD) encapsulated inside the laser. The general expression for the power emitted by the laser is:

$$P(\phi_F(\tau)) = P_0[1 + mG(\phi_F(\tau))] \tag{5.1}$$

where P_0 is the power emitted by the unperturbed laser, *m* is the modulation index (typical value is $m \approx 10^{-3}$) and $G(\phi_F(\tau))$ is a periodic function of the interferometric phase $\phi_F(\tau)$, of period 2π.

Because the self-mixing interference expression derived from the three-mirror model is the same as the result derived from the Lang-Kobayash model. Therefore, for the convenience of research, the results of the two models are unified into the following general mathematical model for analysis:

$$\phi_F(\tau) = \phi_0(\tau) - C \cdot \sin[\phi_F(\tau) + \arctan\alpha] \tag{5.2}$$

$$G(\phi_F(\tau)) = \cos(\phi_F(\tau)) \tag{5.3}$$

$$P(\phi_F(\tau)) = P_0[1 + mG(\phi_F(\tau))] \tag{5.4}$$

where $\phi_0(\tau)$ is the optical phase of the external cavity when there is no optical feedback, and $\phi_0(\tau) = \omega_0\tau = 2\pi v_0\tau$, $v_0(\omega_0)$ corresponding to the (angle) frequency of the semiconductor laser without external cavity optical feedback;

$\phi_F(\tau)$ is the optical phase of the external cavity when the optical feedback exists and $\phi_F(\tau) = \omega_F\tau = 2\pi v_F\tau$, $v_F(\omega_F)$ the (angle) frequency of the corresponding semiconductor laser has no external cavity optical feedback;

τ is the flight time in the external cavity. $\tau = 2L/c$, where L is the laser-target distance, c represents the speed of light in the vacuum;

α is the linewidth enhancement factor, $\alpha = (\partial n_R/\partial N)/(\partial n_I/\partial N)$, where N、n_R and n_I respectively represent the current-carrying density of the laser medium in the semiconductor laser, and the real and imaginary parts of the complex refractive index;

C is the feedback level factor, $C = \varepsilon \cdot L \cdot \sqrt{1+\alpha^2} \cdot \sqrt{R_{ext}} \cdot (1-R_2)/(l \cdot n \cdot \sqrt{R_2})$, where R_2 is the laser output facet power reflectivity, R_{ext} is the reflectivity of the target, l is the laser cavity length, and n is the cavity refractive index, ε accounts for a mismatch between the reflected and the lasing modes (typical value is $\varepsilon \approx 0.1-0.8$).

Eq.(5.2) is called the phase equation of the self-mixing interference system, Eq.(5.3) is the interference function, and Eq.(5.4) is the power equation of the self-mixing interference system.

In self-mixing interference experiments, the information of $P(\phi_F(\tau))$ $(i = 1, 2, \cdots N)$ can be obtained by measuring the self-mixing signal, so when C and α are known ,the displacement of the external object can be obtained. This is the theoretical basis for the displacement measurement by self-mixing interferometry(SMI).

5.3. The influence of various parameters in the model on the SMI signal

The factors affecting the SMI signal mainly include the following two aspects. One is the parameter of the LD itself, such as the linewidth enhancement factor α, the feedback parameter *C*. The other is the displacement of the external cavity object, that is, the outer cavity length L. L is determined by the initial distance L_0 and the vibration amplitude of the external cavity target ΔL. In the following, through the numerical simulation, the influence of the feedback parameter *C* and the external target vibration amplitude ΔL on the SMI signal is analyzed.

5.3.1. Influence of the feedback parameter C

The C parameter is of great importance, because it discriminates between different feedback regimes:

The first regime is characterized by weak optical feedback (C $\leqslant$ 1) with a single emission frequency and a narrowing or broadening of the emission line depending on the phase of the feedback.

The second regime is characterized by moderate optical feedback (C > 1), which results in multiple emission frequencies and apparent splitting of the emission line due to rapid mode hopping. The laser under optical feedback remains dependent on the phase of the feedback.

The third regime is characterized by strong optical feedback (C $\gg$ 1), which results in a return to single emission frequency under feedback. The laser under optical feedback remains dependent on the phase of the feedback.

Using the above simulation model, the values are taken under three feedback regimes to analyze the characteristics of the SMI signal (G). The results are shown in the Figure 54.

The simulation conditions are shown as follows:

External cavity phase: $\phi_F(\mathrm{n}) = \phi_0 + a \times \sin(2\pi f \times n)$, $\phi_0 = 30$, $a = 19$, $\alpha = 5$, $f = 20\mathrm{Hz}$, $n = 200$

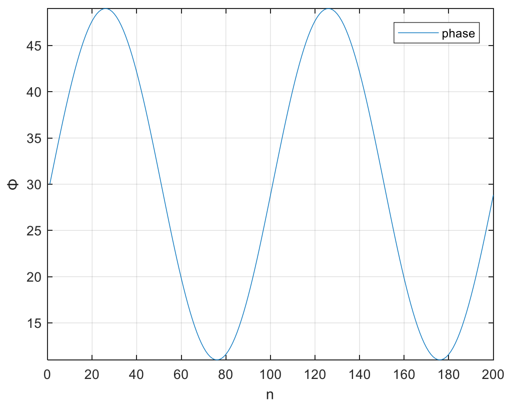

(a) external cavity phase

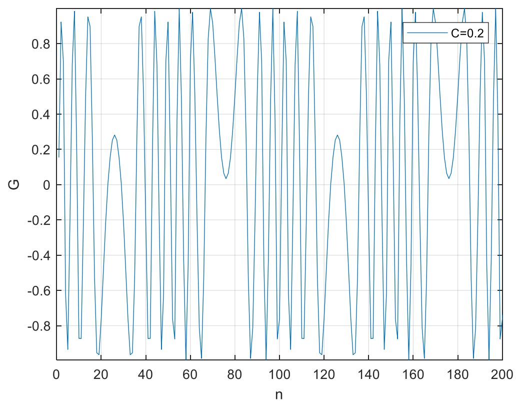

(b) SMI signal with C=0.2

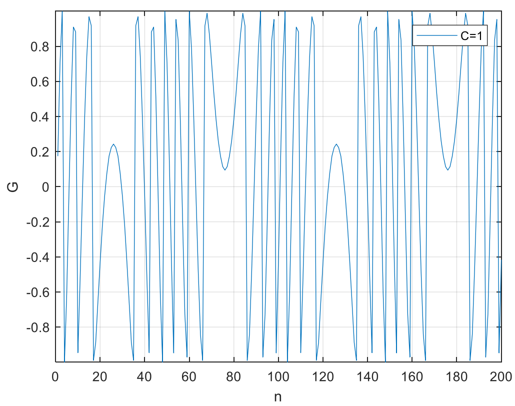

(c) SMI signal with C=1

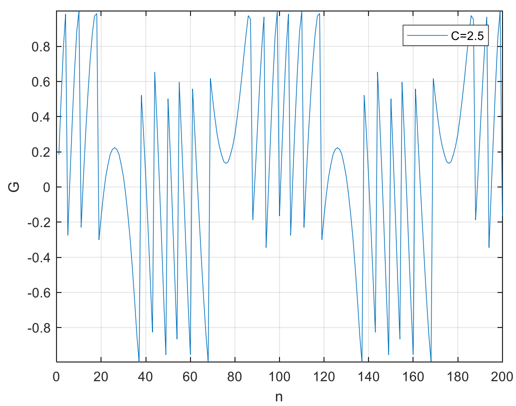

(d) SMI signal with C=2.5

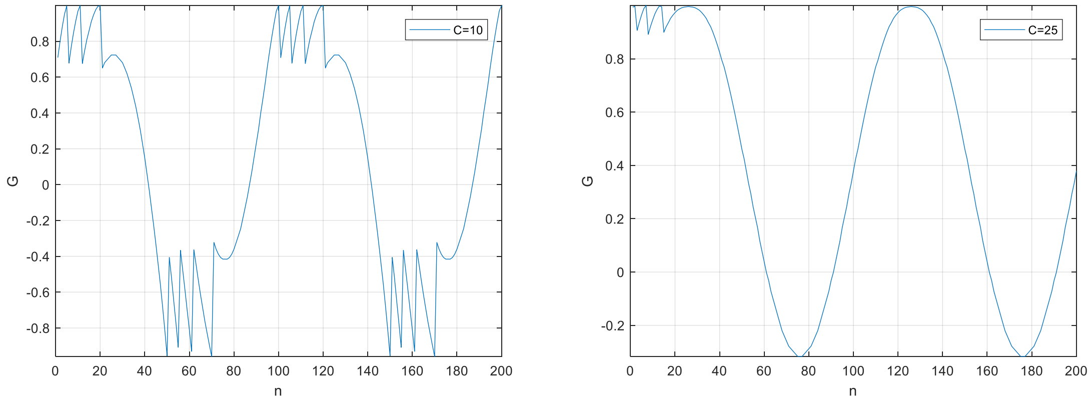

(e) SMI signal with C=10 **(f) SMI signal with C=25**

Figure 54 The self-mixing signal (G) with different feedback parameters

It can be seen from the results that:

(1) When C is 0.2, it belongs to the weak feedback mechanism, and the SMI signal waveform is similar to the traditional interference signal, and is a sinusoidal waveform;

(2) When C is under moderate feedback mechanism, the SMI signal appears as a sawtooth waveform. The larger the C value is, the greater the degree of deformation of the sawtooth, and the waveform also exhibits different degrees of tilt and hysteresis;

(3) Under the strong feedback mechanism, some interference fringes disappeared, and the system became more complicated. When C=25, the interference fringes almost disappeared, and the signal was sinusoidal. The system appeared coherent annihilation. It is considered that the feedback region has no self-mixing effect and is not suitable for sensor applications.

5.3.2. The influence of the external target vibration amplitude

When the feedback intensity C is between 0.7 and 7.8, the SMI system and the conventional interference have the same fringe resolution, that is, each time the amplitude of the measured object changes $\lambda/2$ an interference fringe is generated correspondingly. So the number of interference fringes of the corresponding SMI signal in a vibration period characterizes the magnitude of the vibration amplitude of the target object. From the relationship between ΔL and a ($a = 4\pi\Delta L/\lambda$), the value of the initial cavity ΔL determines the magnitude of the phase a of the outer cavity. In the simulation, a can be used instead of ΔL. Observe the characteristics of the SMI signal by taking different value of a. The simulation results are shown in Figure 55.

The simulation conditions are shown as follows

External cavity phase: $\phi_F(\mathrm{n}) = \phi_0 + a \times \sin(2\pi f \times n)$, $\phi_0 = 30$, $C = 2$, $\alpha = 5$, $f = 20\mathrm{Hz}$, $n = 200$

It can be seen from the results that when the amplitude a of the target object takes different values in one vibration period, the number of the fringes is also different. When the vibration amplitude a is gradually increased, the number of fringes is also correspondingly increased. In practical applications, the amplitude of the vibration of the target object can be measured by counting the number of interference fringes.

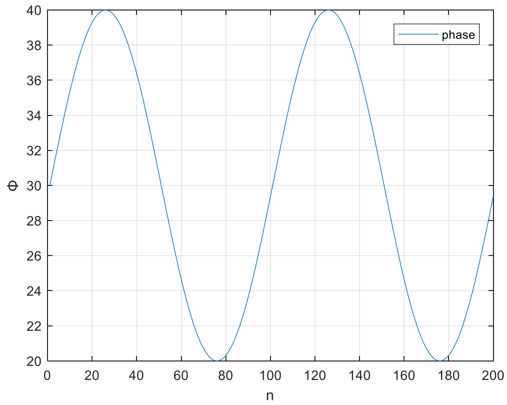

(a) external cavity phase

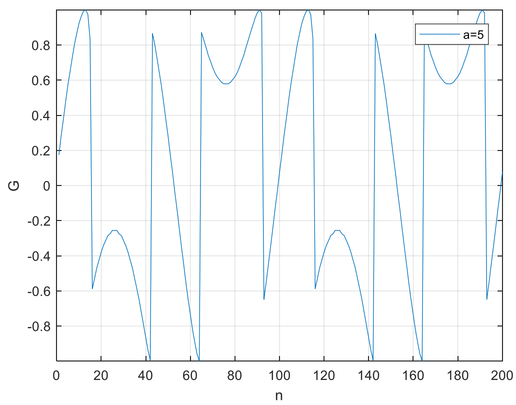

(b) SMI signal with *a*=5

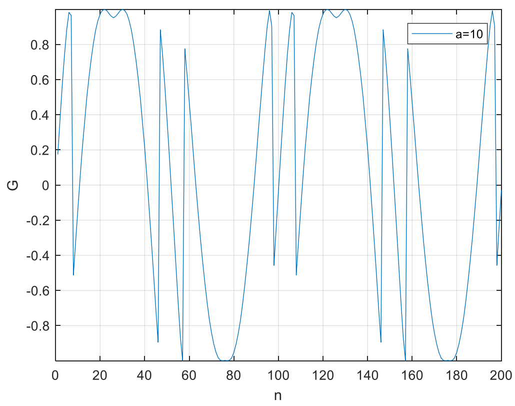

(c) SMI signal with *a*=10

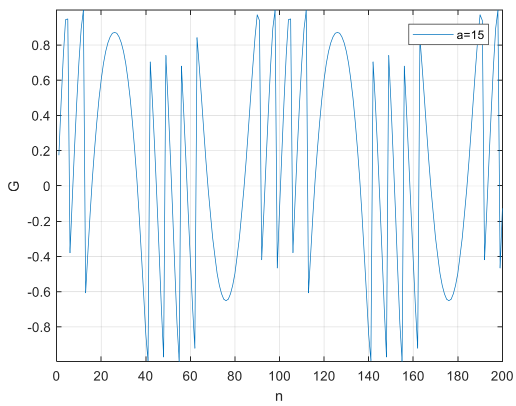

(d) SMI signal with *a*=15

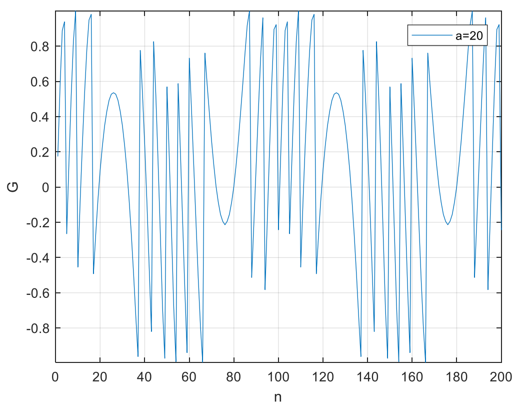

(e) SMI signal with *a*=20

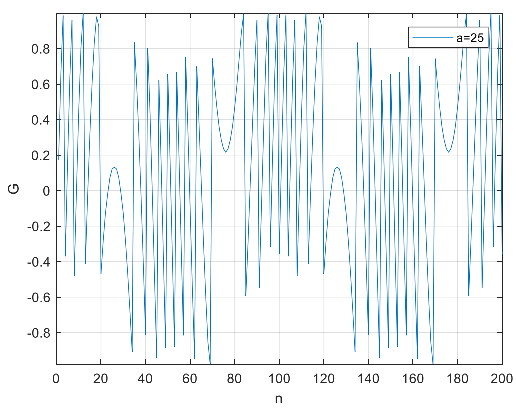

(f) SMI signal with *a*=25

Figure 55 The self-mixing signal (G) with different vibration amplitude *a*

From the above simulation analysis, the influence of the parameters on the SMI signal waveform is obtained. The feedback parameter C determines the degree of tilt of the signal waveform and the amplitude of the vibration of the external cavity object determines the number of signal fringes in a period.

Chapter 6 Displacement measurement by fringes counting

Fringes counting method is a common method of interferometry. For the moderate optical feedback regime, the self-mixing interference signal is a tilt sawtooth waveform, and the tilt direction corresponds to the displacement direction, so it is possible to measure the displacement with direction. The fringes counting method has the characteristics of simple measuring system and large measuring range.

6.1. Basic principle of fringe counting

From Eq.(5.2)、Eq.(5.3), it can be obtain that

$$G = \cos(\omega_0\tau - C\sin(\omega_0\tau - \cdots\cdots + \arctan(\alpha)) + \arctan(\alpha)) + \arctan(\alpha)) \tag{6.1}$$

Obviously

$$G(\omega_0\tau + 2\pi) = G(\omega_0\tau) \tag{6.2}$$

Therefore, the relative change of $G(\omega\tau)$ is a periodic function of $\omega_0\tau$, the period is 2π. From $\tau = 2L/c$ and $\omega_0 = 2\pi c/\lambda$, we can know that a fringe means that the external length changes by half of the wavelength of the laser. The displacement of the outer cavity is:

$$L = L_0 \pm k\cdot\frac{\lambda_0}{2} \tag{6.3}$$

Where L_0 is the initial external cavity length, k is the number of interference fringes contained in the two adjacent turning points, and the sign of the coefficient depends on the tilt direction of the interference signal, which indicates the direction of the target movement.

The flow chart of the fringes counting method is shown in Figure 56.

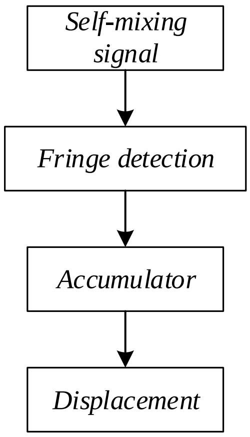

Figure 56 The flow chart of the fringes counting method

6.2. Algorithm simulation result

Since the self-mixing interference signal is a sawtooth wave, the SMI signal is differentiated to obtain a pulse signal corresponding to the zero-crossing point of the SMI signal.

Based on Eq. (6.3), one pulse means half wavelength displacement. The sign of the zero-crossing pulse signal reflects the direction of motion of the object.

Assume that the vibration of the external object is:

$$L = L_0 + \Delta L \sin(2\pi ft) \tag{6.4}$$

Where L_0 is the initial length of the external cavity, ΔL is the amplitude of the vibration of the target, f is the vibration frequency.

From $\omega_0 \tau = \omega_0 \times 2L / c = 4\pi L / \lambda_0$, it can be obtain that

$$\omega_0 \tau = A_0 + A \sin 2\pi ft \tag{6.5}$$

Where $A_0 = 4\pi L_0 / \lambda_0$ is the initial phase of the external cavity, $A = 4\pi \Delta L / \lambda_0$ is the amplitude of the phase fluctuation of the external cavity. For convenience, use A_0 、 A replace L_0 、 ΔL in the simulation.

The parameter takes the value: $\alpha = 4, C = 0.9, A_0 = 30, A = 19, f = 195Hz$, the phase signal and the self-mixing signal are shown in Figure 57.

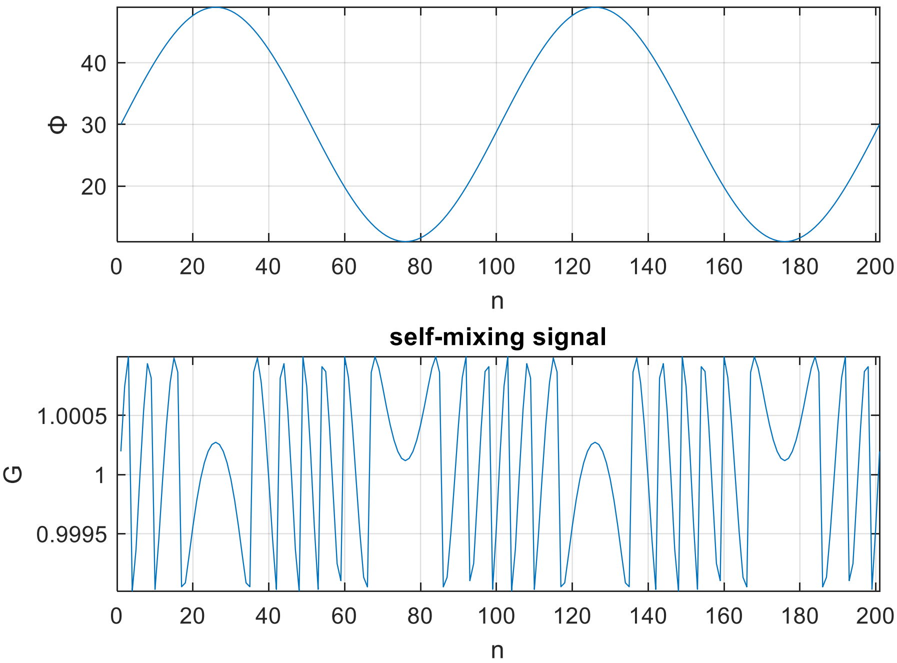

Figure 57 phase signal (upper trace) and self-mixing signal (lower trace)

For the convenience of processing, the differentially obtained signal is further flattened. The differential signal and the processed differential signal are shown below, where the position of the pulse corresponds to the zero-crossing position of the self-mixing interference signal.

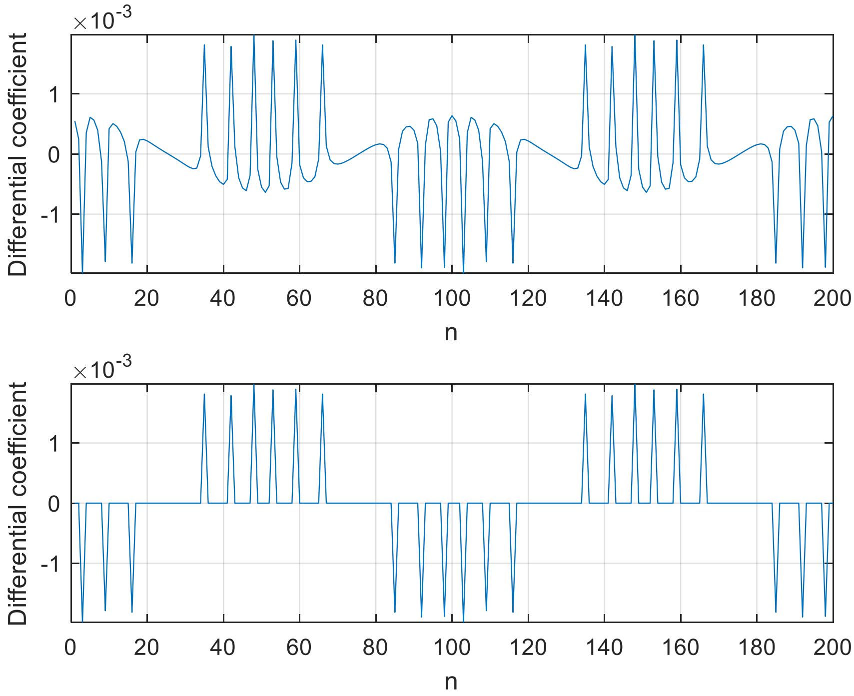

Figure 58 the differential signal (upper trace) and the flattened differential signal (lower trace)

Finally, the displacement of the target is reconstructed as shown in Figure 59. From the lower trace in Figure 59, the normalized phase signal is compared with the normalized displacement signal, it can be seen that the two signals have the same frequency and amplitude, which means that the fringe counting method can accurately reproduce the displacement of the outer cavity, but its resolution is limited by the half-wave length of the light wave.

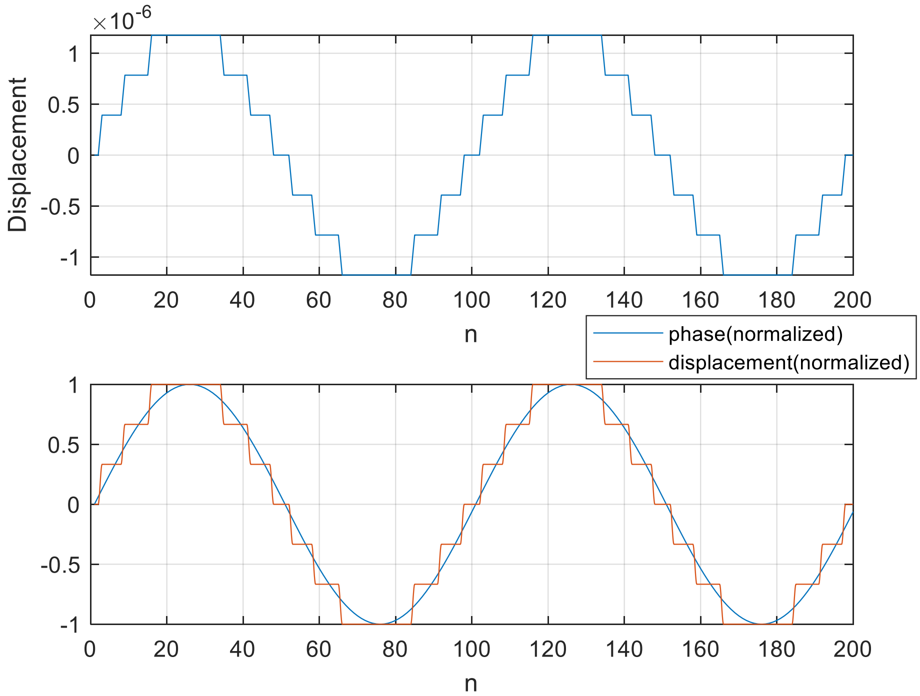

Figure 59 displacement (upper trace) and the normalized displacement (lower trace)

6.3. Experimental device and results

In order to verify the feasibility of the method, a measurement system is built. And the hardware system is shown as follows:

Figure 60 hardware system

A speaker is used as the target object, the displacement is generated by the vibration of the speaker. The signal generator is used to provide a sinusoidal signal for driving the vibration of the speaker, and the Analog discovery 2 is used for signal acquisition. Set the peak-to-peak value of the sinusoidal signal to 0.2V and the frequency to 100Hz. The displacement measurement result is shown in Figure 61. It can be seen that the reconstruction result can reflect the actual vibration of the speaker.

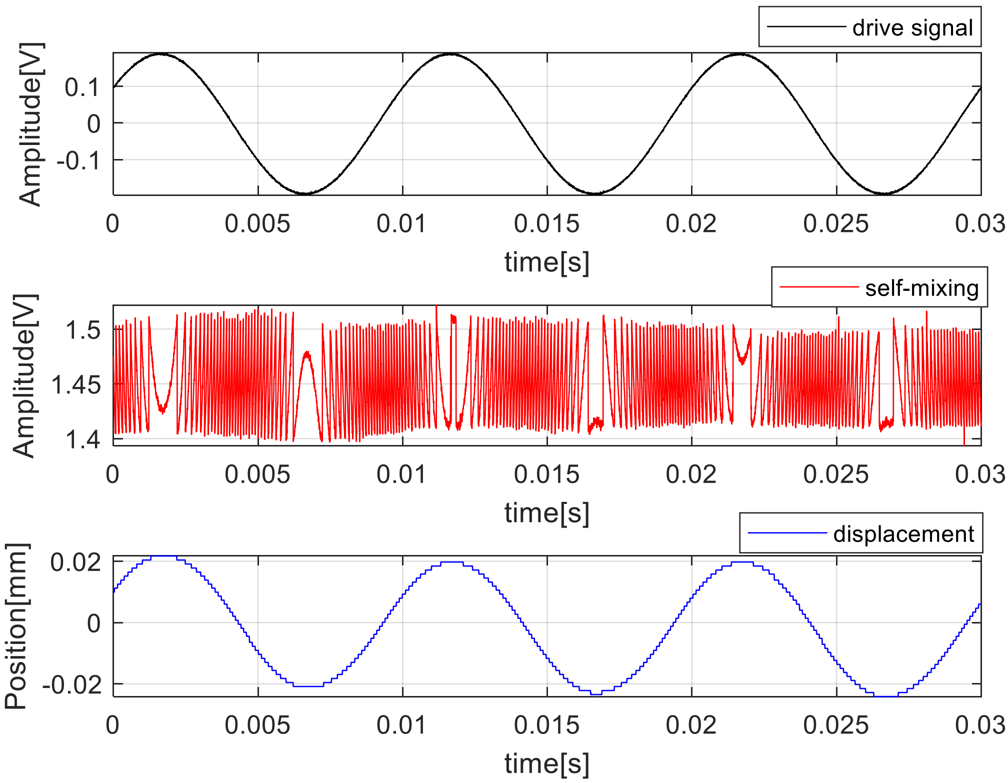

Figure 61 the displacement measurement results of a speaker

6.4. Conclusions

According to the characteristics of the SMI signal, the fringes counting method to measure the displacement of the target object is introduced in this chapter. The theoretical basis of the method is introduced systematically. Then a measurement system is built, and the feasibility of the method is proved by both simulation and experiment. The method is characterized by large range and high precision, which can measure any regular displacement, and the system is easy-built and low-cost. But the method is sensitive to noise and the measurement accuracy is limited by the laser half wavelength.

Chapter 7 Speed meter

7.1. Principle of functioning

Doppler tachometers are commonly used for motion measurements and it is based on the interference observed when two coherent beams coincide. The resulting intensity measured by the photodetector varies with the sinusoidal function of the phase difference between the two beams. In fact, the self-mixing interferometer can be regarded as an optical Doppler system, which produces interferometric signals at a frequency equal to the optical frequency difference between output light and back-injected light; in other terms it represents a homodyne demodulator. The relationship between speed and signal frequency is:

$$f_D = 2 \cdot v / \lambda \tag{7.1}$$

where v is the moving speed of the target, λ is the laser wavelength and f_D is the interferometric signal frequency. Therefore, by evaluating the frequency of the interference fringes, the moving speed of the target can be determined. However, only the absolute velocity information can be obtained by the Doppler effect, and information about the direction of motion cannot be obtained.

Under moderate feedback conditions, the shape of the self-mixing interference signal is close to the sawtooth wave. When the target moves toward the laser, the stripe is deformed in one way; when the direction of motion is reversed, the stripe deformation mode is also reversed. For the convenience of discussion, the two modes of sawtooth waves in Figure 62 respectively represent self-mixing interference signals generated when the target approaches and moves away from the light source:

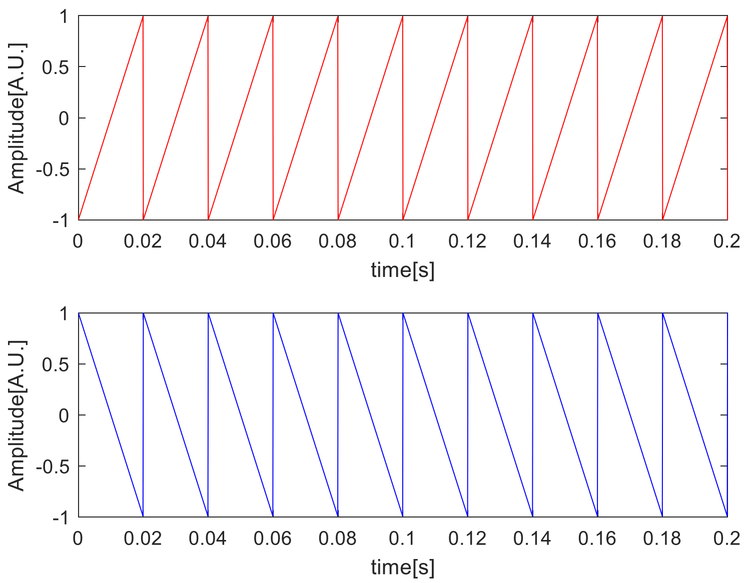

Figure 62 sawtooth signal and its inversion

The signals in the graph are odd functions. It is well known that the Fourier transform of real and odd signals is purely imaginary (sinusoidal series). Since the real part is zero, all harmonics have a phase of ±π/2. Therefore, for the two signals in Figure 62, they have the same amplitude spectrum, but different phase characteristics, and the phases of all the harmonics are opposite. In order to distinguish the direction of movement, the phase of the first harmonic can be measured, and when the direction is reversed, the phase changes by π.

In the actual case, the interference signal is observed without triggering, with the result that the acquired signal is not an odd number but with a random time delay. This leads to a transition at each phase:

$$\varphi_i = \pm\frac{\pi}{2} - 2\pi i f \Delta T \tag{7.2}$$

where φ_i is the phase of the i-th harmonic, and f is the fundamental frequency of the signal (ie, the first harmonic frequency), ΔT is the delay of the actual signal and the theoretical odd-function signal.

Then the first two harmonics exhibits a phase shift equal to

$$\begin{aligned} \Delta\varphi_1 &= -2\pi f \Delta T \\ \Delta\varphi_2 &= -4\pi f \Delta T \end{aligned} \tag{7.3}$$

Therefore, the time delay can be expressed as[58]

$$\Delta T = -(\Delta\varphi_2 - \Delta\varphi_1)/2\pi f = -\Delta\varphi_{2-1}/2\pi f \tag{7.4}$$

where $\Delta\varphi_{2-1}$ is the phase difference between the first two harmonics.

We can estimate the direction of signal distortion by measuring the phase of the first harmonic φ_{10}, in the sampling condition of Figure 62, when the first two harmonics have the same phase. Then the first harmonic phase after the time shift is

$$\varphi_{10} = \varphi_1 - \Delta\varphi_1 = \varphi_1 + 2\pi f \Delta T = \varphi_1 - (\varphi_2 - \varphi_1) = 2\varphi_1 - \varphi_2 \tag{7.5}$$

where φ_1 and φ_2 can be measured in any time instant, while φ_{10} should have the value of $-\frac{\pi}{2}$ for the upper signal in Figure 62, and $+\frac{\pi}{2}$ for the lower signal.

Therefore, by measuring the phase of the first harmonic and the second harmonic, the direction information of the motion can be obtained. The entire block diagram of the method is described in Figure 63.

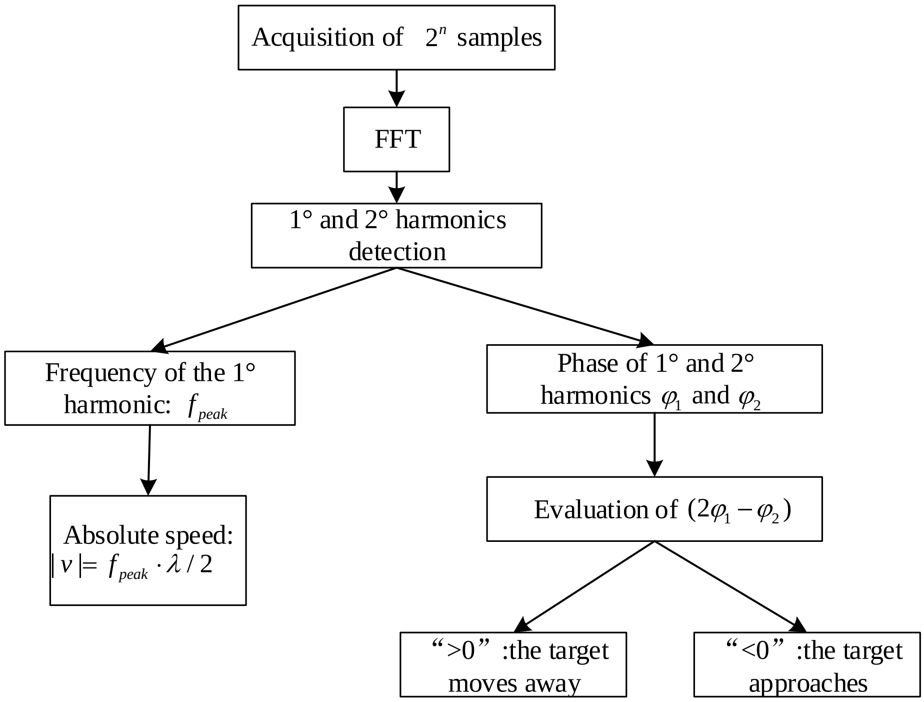

Figure 63 Block diagram of the method

The algorithm is based on the spectral analysis of the interference signal and is more robust than the method based on time domain analysis.

7.2. Preliminary simulation

In the actual measurement, the selection of the measurement points 2^n is realized by the movement of the window, with the window length $L = 2^n$. Since the fringes density of the self-mixing interference signal changes with the movement of the target object, the number of fringes in the FFT window changes with time. In the simulation, by changing the value of the window length L, the influence of the number of fringes in the FFT window on the reconstruction result is studied. Taking L=16, 64, 256 respectively, and the reconstruction results are shown as follows:

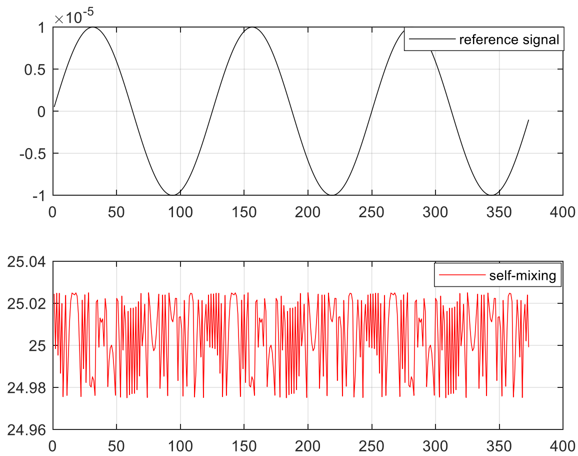

Figure 64 the reference signal (upper trace) and the self-mixing signal (lower trace)

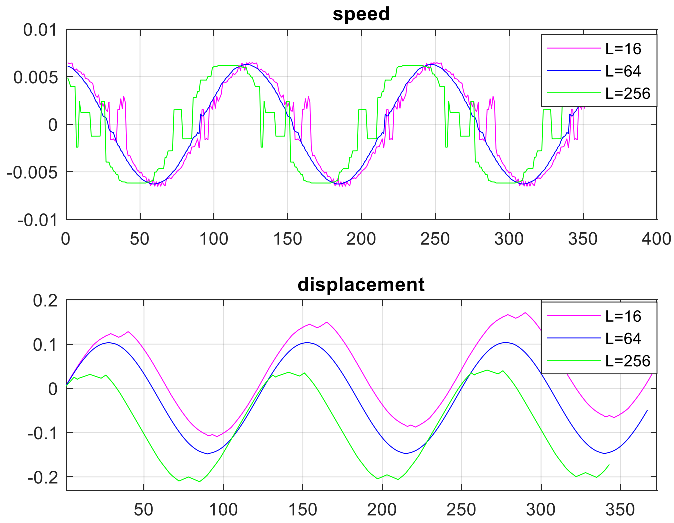

Figure 65 the target speed (upper trace) and the target displacement (lower trace)

It can be seen that the length of the window is too long and too short (that is, the number of stripes in the window is too much or too small), will both cause the disturbance on the reconstruction target speed and affect the reconstruction accuracy. When the number of stripes is in the range of 5-10, the reconstruction result is better.

In the actual measurement, the number of stripes in the window can be adjusted by changing the length of the window or changing the sampling frequency. In the experiment, the number of the fringes in the window is adjusted by changing the sampling frequency. The current window fringe number is estimated by the following formula:

$$N = \frac{f_{peak}}{f_s} \times L = \frac{f_{peak}}{f_s} \times 2^n \tag{7.6}$$

where f_{peak} is the signal fundamental frequency, f_s is the sampling frequency, $L = 2^n$ is the window length. If N exceeds the interval (5, 10), the optimal reconstruction condition can be achieved by changing the current sampling frequency.

7.3. Experimental results

Using the same experimental equipment as Chapter 6, the target motion speeds and displacements reconstructed results at different driving frequencies of 50 Hz, 100 Hz, and 200 Hz are shown in Figure 66 to Figure 68:

The sample frequencies are adjusted automatically in the experiment for different driving frequency, the final sample frequencies after adjusted are :

When the driving frequency is *f*=50Hz, the sample frequency is *fs*=125kHz;

When the driving frequency is *f*=100Hz, the sample frequency is *fs*=250kHz;

When the driving frequency is *f*=200Hz, the sample frequency is *fs*=500kHz;

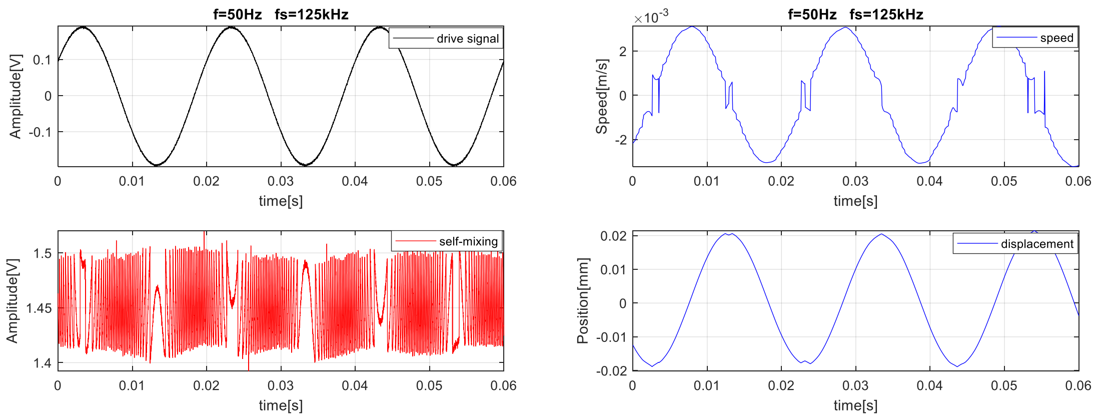

Figure 66 the speed and displacement reconstruct by the technique on *f*=50Hz

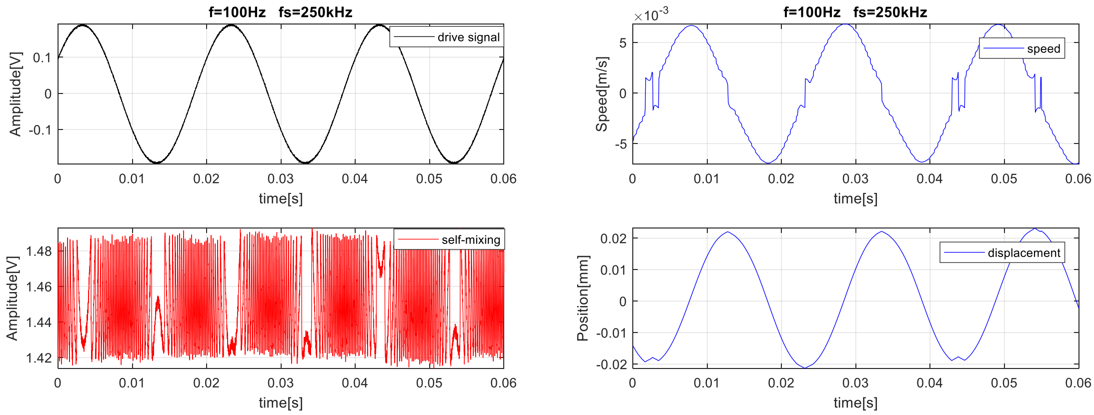

Figure 67 the speed and displacement reconstruct by the technique on *f*=100Hz

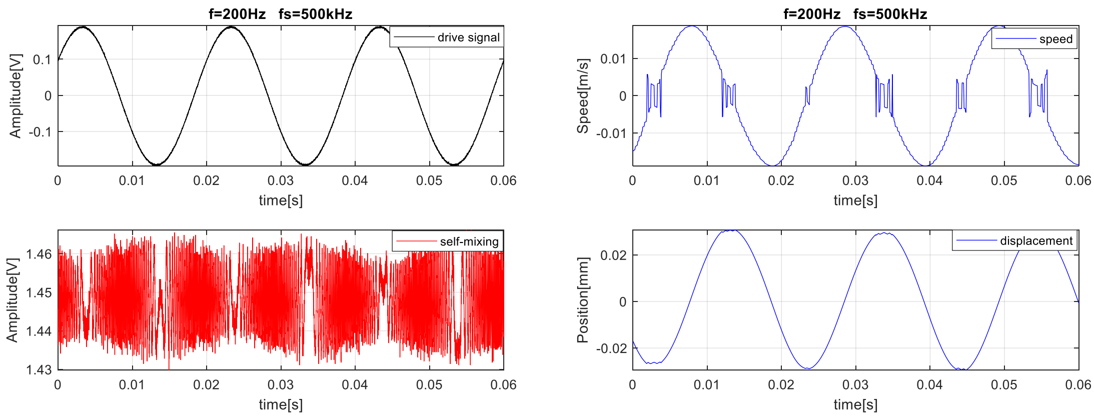

Figure 68 the speed and displacement reconstruct by the technique on *f*=200Hz

The results show that by adaptively adjusting the sampling frequency, although the velocity is disturbed when there is a change of the displacement direction, the method can basically reconstruct the velocity and displacement information of the target object accurately.

7.4. Conclusions

In this chapter, a method of measuring speed and displacement based on frequency domain analysis of self-mixing signals is discussed. Firstly, the principle of the algorithm is introduced.

The absolute velocity of the motion of the object is obtained by Doppler frequency shift. The sign of the motion is determined by phase analysis. Multiplying the absolute velocity and the sign of the motion, the complete motion velocity information is obtained. And the displacement of the target object can be obtained from the speed signal. Secondly the simulation verifies the feasibility of the algorithm and the influence of the number of the fringes of FFT process is analysis. Finally, in the actual measurement, design a method to realize the optimal number of fringes by changing sampling frequency automatically. Experiments show that the method can effectively reconstruct the velocity and displacement information of the object, and the robustness is strong.

Conclusions

The main research of this paper is based on laser measurement techniques. According to the application principle, the whole work can be divided into two parts: the measurement based on Fraunhofer diffraction theory and the measurement based on self-mixing interferometry.

Based on the Fraunhofer diffraction theory, this paper studies the system and method for measuring the particle size of narrow distribution.

In the aspect of measurement system, an improved measurement system based on modulation and demodulation technique is proposed, which is composed by a laser light source, an electro-optic modulator, a DMD and a single-point detector. After the laser light source is modulated by the electro-optic modulator, the light intensity is modulated into a sinusoidal shape, and the modulated optical signal pass through the measurement system, and the measurement signal is demodulated and used for particle size distribution reconstruction. Compared with the traditional measurement system, the improved measurement system can effectively suppress the interference of other optical signals during signal propagation and improve the anti-noise ability of the system.

In the aspect of reconstruction algorithm, in order to solve the problem that the existing integral inversion algorithm has lower accuracy for narrow-particle particle reconstruction, the closed-loop control theory is introduced into the reconstruction algorithm. Firstly, the feasibility of introducing closed-loop iteration to improve the narrow-distribution reconstruction result is proved by simulation. Furthermore, the selection of the controller parameters needs massive calculation, so the advanced PID theory is studied to realize adaptive selection of controller parameters and improve the adaptability of the algorithm. Two advanced PID controllers are studied: neural network PID and fuzzy PID. The proposed algorithm based on neural network model has fast iteration and can achieve a typical accurate reconstruction of the narrow distribution, but the reconstruction result is greatly affected by the initial weight. The reconstruction result is unstable when the initial weight is randomly selected. Therefore, the practical application of the method is limited. The proposed algorithm based on fuzzy control theory is also have better expression of the narrow distribution reconstruction than traditional dual integral algorithm. In order to verify the effect of the improved device and algorithm in the actual measurement, a new particle size measurement system based on modulation and demodulation was built. The particle size measurement experiment of polystyrene standard particles was carried out to verify that the system has good anti-noise ability. The measurement signal is used in the particle size distribution reconstruction, which verifies that the improved algorithm has better accuracy for both unimodal and bimodal distribution particles.

Based on self-mixing interference theory, the measurements for speed and displacement are studied. Firstly, numerical simulation of the self-mixing interference theory model is carried out to study the influence of parameters C and a on the self-mixing signal. Secondly, a displacement method base on fringes counting is introduced and a basic measurement system is built. Both the simulation and experimental results show that the method can measure the displacement of the target accurately. The displacement measurement error is less than half of the wavelength. Finally, applying the Doppler effect, a method which can measure the velocity and displacement of the target is studied. In experimental, an adaptive sample frequency choosing method is applying to achieve better results. Both the simulation and the experimental results show that the method can accurately reconstruct the velocity and the displacement of the target with strong robustness.

Future works will concern the study on how to realize the accurate measurement more speedily, both for the particle size distribution reconstruction and the speed or displacement measurement by self-mixing interferometry.

References

[1] 蔡小舒. 颗粒粒度测量技术及应用[M]. 北京:化学工业出版社, 2010:65-112.

[2] 王奥, 王彬彬, 徐滨, 等. RDX 粒度对改性单基药燃烧性能及力学性能的影响[J]. 火炸药学报, 2018,41(2):197-201.

[3] 黄珍霞, 梁峰, 张海军, 等. 含 Co 或 Ni 的双金属及三金属纳米颗粒的制备方法及其催化制氢性能[J]. 化学通报, 2017,80(7):621-630.

[4] 李定国, 熊杰, 卢文华, 等. 锰锌铁氧体纳米颗粒及其磁性液体的制备与磁性研究[J]. 人工晶体学报, 2012,41(2):359-364.

[5] Franck U, Odeh S, Wiedensohler A, et al. The effect of particle size on cardiovascular disorders-The smaller the worse[J]. Science of the Total Environment, 2011,409(20):4217-4221.

[6] 纪运景. 光学衍射法粒子群粒度分布中值粒径概率密度分布函数的数学模型[D]. 南京:南京理工大学, 2002.

[7] 张霜玉, 吕馥言, 夏正猛, 等. 激光粒度法与筛分法测量洗煤泥粒度分布对比[J]. 中国粉体技术, 2014,20(2):43-46.

[8] 刘焕胜, 周金环, 何亚群. 无振动离心筛分法的试验研究[J]. 中国矿业大学学报, 1995,24(3):85-90.

[9] Allen T. Particle Size Measurement[J]. Materials & Processing Report, 1977,2(11):3-4.

[10] 梁树端. 固液分离与颗粒粒度测试技术[J]. 流体机械, 1983(11):21-25.

[11] Van D P E, Coumans F A, Grootemaat A E, et al. Particle size distribution of exosomes and microvesicles determined by transmission electron microscopy, flow cytometry, nanoparticle tracking analysis, and resistive pulse sensing.[J]. Journal of Thrombosis & Haemostasis, 2014,12(7):1182-1192.

[12] 韦冬冬. 基于显微图像的 PTA 粒径分布估计方法研究[D]. 杭州:浙江大学, 2010.

[13] 熊向军. 颗粒粒度粒形测量的新技术介绍——时间转换理论以及动态图像分析[C]. 中国纳米技术应用研讨会论文集, 2004.

[14] Giechaskiel B, Maricq M, Ntziachristos L, et al. Review of motor vehicle particulate emissions sampling and measurement: From smoke and filter mass to particle number[J]. Journal of Aerosol Science, 2014,67(1):48-86.

[15] 袁易全. 近代超声原理及应用[M]. 南京:南京大学出版社, 1996.

[16] 苏明旭, 蔡小舒. 超细颗粒悬浊液中声衰减和声速的数值分析研究[J]. 声学学报,

2002,27(3):218-222.

[17] Mougin P, Wilkinson D, Roberts K J, et al. Sensitivity of particle sizing by ultrasonic attenuation spectroscopy to material properties[J]. Powder Technology, 2015,134(3):243-248.

[18] Xu R. Particle Characterization: Light Scattering Methods[J]. China Particuology, 2003,1(6):271.

[19] 朱震，王式民，叶茂，等. 前向光散射粒子消光测量的校正[J]. 激光杂志，1998，19(6):32-35.

[20] Louedec K, Dagoretcampagne S, Urban M. Ramsauer approach to Mie scattering of light on spherical particles[J]. Physics, 2009,80(1):75-84.

[21] Wang N N, Shen J Q. A study of the influence of misalignment on measuring results for laser particle analyzers[J]. Particle & Particle Systems Characterization, 2015,15(3):122-126.

[22] 胡柱国，盛德仁，蔡颐年. 两相流中液滴微粒尺寸分布的光散射法优化测量[J]. 西安交通大学学报, 1989,23(6):15-25.

[23] Bott S E, Hart W H. Extremely Wide Dynamic Range, High-Resolution Particle Sizing by Light Scattering[M]. American Chemical Society ,1991.

[24] 张福根. 激光粒度仪的光学结构[C]. 中国颗粒学会 2006 年年会暨海峡两岸颗粒技术研讨会论文集, 2006.

[25] 沈建琪. 光散射法测粒技术延伸测量下限的研究[D].上海:上海理工大学, 1999.

[26] 陈琪星，王燕民. 激光粒度测量中的一种无模式综合反演算法[J]. 中国粉体技术, 2008,14(3):10-14.

[27] Tihonov A N. On the solution of ill-posed problems and the method of regularization[C]. Doklady Akademii Nauk SSSR, 1963:501-504.

[28] Leberl F. Introduction to the mathematics of inversion in remote sensing and indirect measurement[J]. Tectonophysics, 2013,65(3):376-378.

[29] Chahine M T. Determination of the Temperature Profile in an Atmosphere from its Outgoing Radiance[J]. Optical Society of America, 1968,58(12):1634-1637.

[30] Guermond J L, Minev P, Shen J. An overview of projection methods for incompressible flows[J]. Computer Methods in Applied Mechanics and Engineering ,2006,195(44): 6011-6045.

[31] Jianping W, Shizhong X, Yimo Z, et al. Improved projection algorithm to invert forward scattered light for particle sizing[J]. Applied Optics, 2001,40(23):3937-3945.

[32] Ishimaru A, Marks R J, Tsang L, et al. Optical Sensing Of Particle Size Distribution By Neural Network Technique[C]. International Geoscience & Remote Sensing Symposium. IEEE, 1990.

[33] 王亚伟. 光散射理论及其应用技术[M]. 北京:科学出版社, 2013.

[34] Chin J H. Particle size distributions from angular variation of intensity of forward-scattered light at very small angles[J]. The Journal of Physical Chemistry, 1955,59(9):841-844.

[35] Shifrin KS, Zolotov IG. Determination of the aerosol particle-size distribution from simultaneous data on spectral attenuation and the small-angle phase function[J]. Applied Optics, 1997,24(36):6047-6056.

[36] Zhang C, Lijun X, Jie D. Integral inversion to Fraunhofer diffraction for particle sizing[J]. Applied Optics, 2009,48(25):4842-4850.

[37] 杨福桂, 王安廷, 明海, 等. 激光衍射粒径测量中的 Chin-Shifrin 反演算法[J]. 光学精密工程, 2011,19(2):323-331.

[38] Chen Q, Liu W, Wang W J, et al. Particle sizing by the Fraunhofer diffraction method based on an approximate non-negatively constrained Chin-Shifrin algorithm[J]. Powder Technology, 2017,317(1):95-103.

[39] 陈泉. 基于线阵 CCD 探测器的激光粒度测量技术研究[D]. 淄博:山东理工大学, 2017.

[40] Wang W, Liu W, Tan S, et al. Optimized criteria for angular parameter selection for the Chin-Shifrin integral transform inversion[J]. Optics Express, 2018,26(8):10858.

[41] 张艳春, 刘缠牢, 赵丁. 基于米氏散射理论的粒度测试算法研究[J]. 国外电子测量技术, 2009,28(11):24-25.

[42] Kerker M. The Scattering of Light and Other Electromagnetic Radiation[M]. Academic Press, 1969.

[43]Tsang L, Jin A K. Scattering of Electromagnetic Waves, Advanced Topics[M]. Wiley, 2001.

[44] Bertero M, Boccacci P, Mol C D, et al. Particle Size Distributions from Fraunhofer Diffraction[J]. Optica Acta International Journal of Optics, 1988,30(8):1043-1049.

[45] 沈建琪, 王乃宁. 关于小角前向散射激光测粒仪准则数 X 的讨论[J]. 中国激光, 1998,25(10):891-896.

[46] Jiayi Z, Zhang C, Heng X, et al. Digital micro-mirror device-based detector for particle-sizing instruments via Fraunhofer diffraction[J]. Applied Optics, 2015,54(18):5842.

[47] 魏家荣, 蔡瑞琳, 朱敏, 等. 用激光粒度仪检测还原染料颗粒细度的研究[J]. 科技

成果管理与研究, 2012,(5):53-56.

[48] Peleg M. Determination of the parameters of the Rosin-Rammler and beta distributions from their mode and variance using equation-solving software[J]. Powder Technology, 1996,87(2):181-184.

[49] Kanwal R P. Classical Fredholm Theory[M]. Springer New York, 2013: 41-60.

[50] Schmidhuber J. Deep learning in neural networks: An overview[J]. Neural networks, 2015,61:85-117.

[51] Heaton J. Ian Goodfellow, Yoshua Bengio, and Aaron Courville: Deep learning[J]. Genetic Programming and Evolvable Machines, 2018,19(1-2):305-307.

[52] Astrom K J. Information and Control[J]. Nature, 1957,180(4595):1097-1097.

[53] 刘金琨. 先进 PID 控制 MATLAB 仿真.第 3 版[M]. 北京:电子工业出版社, 2011.

[54] 戴忠达，张曾科，汤俭. 一种改进的模糊控制器及其应用[J]. 自动化学报，1990,16(3):258-261.

[55] 郁道银, 谈恒英. 工程光学.第 3 版[M]. 北京:机械工业出版社, 2011.

[56] Taimre T, Nikolić M, Bertling K, et al. Laser feedback interferometry: A tutorial on the self-mixing effect for coherent sensing[J]. Advances in Optics & Photonics, 2015,7(3):570.

[57] Giuliani G, Norgia M, Donati S, et al. Laser diode self-mixing technique for sensing applications[J].Journal of Optics A: Pure and Applied Optics, 2002(4):S283-S294.

[58] Magnani A, Pesatori A, Norgia M. Real-Time Self-Mixing Interferometer for Long Distances[J]. IEEE Transactions on Instrumentation & Measurement, 2014,63(7):1804-1809.